

Charge carrier dynamics in CuInS₂-based solar cells

Proefschrift

ter verkrijging van de graad van doctor
aan de Technische Universiteit Delft,
op gezag van de Rector Magnificus, prof. dr. ir. J.T. Fokkema,
voorzitter van het College van Promoties,
in het openbaar te verdedigen op

dinsdag 8 september 2009 om 15:00 uur

door

Joris Petrus Theodorus HOFHUIS

materiaalkundig ingenieur

geboren te Delft

Dit proefschrift is goedgekeurd door de promotor
Prof. dr. J. Schoonman

Samenstelling promotiecommissie

Rector Magnificus	voorzitter
Prof. dr. J. Schoonman	Technische Universiteit Delft, promotor
dr. A.P.L.M. Goossens	Technische Universiteit Delft, copromotor
Prof. dr. B. Dam	Technische Universiteit Delft
Prof. dr. ir. B.J. Thijsse	Technische Universiteit Delft
Prof. dr. M. Zeman	Technische Universiteit Delft
Prof. dr. U. Rau	Institut für Energieforschung, Duitsland
Prof. dr. H.W. Schock	Technische Universität Berlin, Duitsland

dr. A.P.L.M. Goossens heeft als begeleider in belangrijke mate aan de totstandkoming van het proefschrift bijgedragen.

Printed by Wöhrmann Print Service

Copyright (c) 2009 by Joris Hofhuis

All rights reserved. No part of the material protected by this copyright notice may be reproduced or utilized in any form or by any means. Electronic, or mechanical, including photocopying, recording or by any information storage and retrieval system, without permission of the author.

ISBN: 978-90-8570-405-8

Printed in the Netherlands

TABLE OF CONTENTS

1	Introduction	1
1.1	Renewable energy	2
1.2	Semiconductor solar cells	3
1.2.1	<i>Power from the sun</i>	3
1.2.2	<i>Principles of solar cell operation</i>	5
1.2.3	<i>Types of solar cells</i>	7
1.2.4	<i>Synthesis of semiconductor solar cells</i>	9
1.3	Efficiency losses in semiconductors	10
1.3.1	<i>Efficiency losses in semiconductor solar cells</i>	10
1.3.2	<i>The recombination of electrons and holes</i>	11
1.4	CuInS ₂	16
1.4.1	<i>Crystal structure and electronic properties of CuInS₂</i>	16
1.4.2	<i>Defect chemistry of Cu-rich CuInS₂</i>	19
1.4.3	<i>Defect-levels in Cu-rich CuInS₂</i>	19
1.5	Aim and outline of this thesis	21
2	Time-of-Flight studies on TiO₂ / CuInS₂ heterojunctions	26
2.1	Introduction	27
2.1.1	<i>Time-of-Flight background</i>	28
2.1.2	<i>Time-of-Flight on pn-heterojunctions</i>	29
2.2	Experimental aspects	30
2.3	Results	32
2.4	Discussion	36
2.4.1	<i>Electrostatic model</i>	38
2.4.2	<i>Charge transport model</i>	41
2.4.3	<i>Combining the models and fitting the ToF experiments</i>	43
2.5	Conclusions	46

3	Elucidation of the excited-state dynamics in CuInS₂ thin films	49
3.1	Introduction	50
3.2	Transient absorption	52
3.3	Experimental aspects	54
3.3.1	<i>Sample preparation</i>	54
3.3.2	<i>Photoluminescence spectroscopy</i>	54
3.3.3	<i>Transient Absorption</i>	55
3.4	Results	56
3.4.1	<i>PL results</i>	56
3.4.2	<i>TA results</i>	56
3.5	Discussion	62
3.5.1	<i>Discussion of the PL data</i>	62
3.5.2	<i>Discussion of the TA data</i>	64
3.5.3	<i>Modeling the recombination mechanism</i>	66
3.5.4	<i>Simulation results</i>	69
3.5.5	<i>Cu/In anti-site defects</i>	72
3.5.6	<i>Effect on solar cell properties</i>	73
3.6	Conclusions	74
4	How multiple decay paths affect the photoluminescence intensity in CuInS₂	78
4.1	Introduction	79
4.2	Experimental aspects	81
4.3	Results	82
4.4	Discussion	84
4.4.1	<i>The recombination model</i>	85
4.4.2	<i>Simulating power dependent PL experiments</i>	86
4.4.3	<i>Filling of the defect states</i>	92
4.4.4	<i>The influence of temperature upon defect-state saturation and g_{th}</i>	93
4.4.5	<i>Applying the model to CuInS₂</i>	95
4.5	Summary and conclusions	99

5 How flash-annealing affects defect association in spray deposited CuInS₂	101
5.1 Introduction	102
5.1.1 <i>Chalcopyrite material quality</i>	102
5.1.2 <i>Anti-site defects</i>	103
5.1.3 <i>Recombination mechanism</i>	104
5.2 Experimental aspects	105
5.2.1 <i>Sample preparation</i>	105
5.2.2 <i>Photoluminescence spectroscopy</i>	106
5.2.3 <i>Transient absorption</i>	106
5.3 Results	108
5.3.1 <i>Raman and PL spectroscopy</i>	108
5.3.2 <i>Transient absorption spectroscopy</i>	110
5.3.3 <i>Transient absorption spectroscopy at 1.38 eV</i>	111
5.3.4 <i>Transient absorption spectroscopy at 1.13-1.03 eV</i>	112
5.3.5 <i>Transient absorption spectroscopy at 0.95 and 0.85 eV</i>	113
5.4 Discussion	114
5.4.1 <i>Raman and PL measurements of the as-deposited samples</i>	114
5.4.2 <i>Construction of the band diagrams</i>	115
5.4.3 <i>Introduction transient absorption measurements</i>	116
5.4.4 <i>Probe energy of 1.38 eV</i>	117
5.4.5 <i>Probe energies of 1.13 eV - 1.03 eV</i>	118
5.4.6 <i>Probe energy of 0.95 eV and 0.85 eV</i>	120
5.4.7 <i>The effect of flash-annealing on the recombination mechanism of CuInS₂ thin films and the associated defect state association.</i>	121
5.4.8 <i>The role of sulfur</i>	123
5.4.9 <i>Solar cells</i>	124
5.5 Summary and conclusions	124
Summary and Outlook	128
Samenvatting	133
Publications	139
Curriculum Vitae	140
Dankwoord	141

Introduction

1.1 Renewable energy

In the previous 100 years, the demand for energy has increased substantially. Fossil fuels are applied globally to generate mechanical power, electrical power, and heat. The global economy depends on the price of oil, while the availability of oil gives reason to political and military instabilities. The growing consumption of fossil fuels has led to environmental pollution. The reserve of fossil fuels is decreasing and will no longer be available in due time.

Many reasons motivate the development of renewable energy. Global warming may stop, nature will recover, and hopefully people will stop fighting over natural resources of fossil fuel. Furthermore, despite the environmental problems and political needs, it should be realized that fossil fuels like oil and natural gas are no longer available in the not too distant future.

For the last decades, more and more successful sources of renewable energy have been explored. New systems in which renewable energy is the key factor are being developed. Sources of renewable energy, such as wind-energy, hydropower, solar energy, and bio-energy are combined with renewable storage of energy (rechargeable batteries or hydrogen storage). Together with the developments of electrical applications, such as the fuel cell and the electric motor, fossil fuels can be replaced. The global introduction of a renewable energy source is determined by its commercial potential. The cost of renewable energy has to compete with the cost of fossil fuels. To be completely renewable, the amount of energy that is generated by a renewable energy source has to be more than the energy that is needed for the production of the corresponding energy device.

Scientific research is needed for the development of new technologies. This thesis is part of a scientific research project that contributes to the development of an economically and energetically favorable solar cell. Recently, it has been shown that for large solar power plants the energy-payback-time is less than 3 years¹. The solar cells of the type that are investigated in this thesis (spray-pyrolysis deposited CuInS₂-based solar cells) have already shown their economical potential. The company Advanced Photovoltaic Applications is building a factory that produces an all-spray-deposited CuInS₂-based solar cell. These solar cells will operate mainly in large power plants and are not (yet) available for customer applications.

1.2 Semiconductor solar cells

1.2.1 Power from the sun

The sun generates an enormous amount of energy, of which a small fraction reaches the surface of the earth. However, this amount of 162.000 TeraWatt² power is sufficient to supply the entire world of energy. The solar power that hits the surface has the physical nature of UV light, visible light, and near-infrared radiation. The challenge of solar cell development is to convert solar light as much as possible into electricity. This conversion has to be energetically and economically favorable. The development of production methods that consume little energy and the reduction of material costs is needed to improve the energetic and economic efficiency of solar cells.

The discovery of the photovoltaic effect by A.C. Becquerel in 1839 has initiated the subject of photovoltaics³. Charles Fritts developed a 1% efficient solar cell in 1883. After years of research, Bell Laboratories invented the silicon solar cell, which still is the standard solar cell technology⁴. Nowadays, the efficiency of silicon solar cells has reached up to 24.7% at laboratory scale⁵ and 18% for commercial cells.

Three solar cell generations can be distinguished⁶. The first generation is initiated by the invention of the silicon solar cell and includes all bulk semiconductor solar cells. This generation of solar cells has a low efficiency and high production costs, as is evident from Figure 1.1. The solar cell market, however, is still dominated by this generation of solar cells². The second generation solar cells consist of cells in which new technologies and materials improved the economical viability by decreasing the production costs. At the time of writing, the 2nd generation of solar cells is being commercialized and solar power plants are now under construction². However, research is still needed to further improve these solar cells and to improve their efficiency. The 3rd generation of solar cells is expected to be the solar cell of the future. The development of functional materials, nano-technologies, and quantum dots, combined with theoretical approaches, will lead to a large increase in solar cell efficiency. Years of development are needed before these devices will be commercialized.

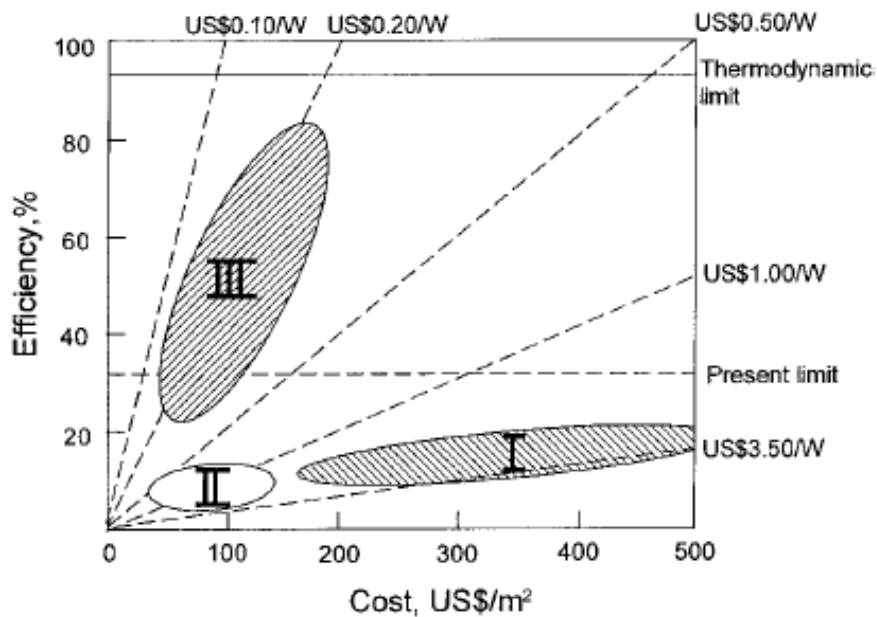
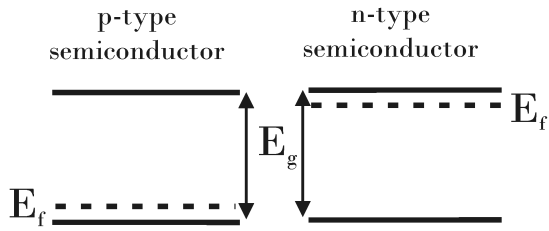


Figure 1.1: Efficiency and cost projections for first-, second-, and third-generation photovoltaic technology⁶.

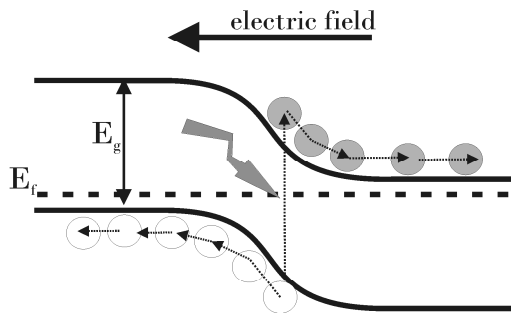
1.2.2 Principles of solar cell operation

The principle of a solar cell is demonstrated in Figure 1.2. The width of the energy gap E_g of a semiconductor is, in contrast to insulators, small enough to excite electrons from the valence band to the conduction band by the absorption of light. This property makes semiconductors excellent materials for photovoltaic applications. The use of dopants determines whether a semiconductor has n-type or p-type conductivity. Joining an n-type semiconductor to a p-type semiconductor forces the Fermi-levels to equilibrate, by a change of the relative position of the energy bands, as is illustrated in Figure 1.2b. The result is an electric field across the pn-junction region. After illumination with sunlight, excited electrons migrate under influence of the electric field, and cause an electrical current. The n-type semiconductor allows a selective electrical contact to the conduction band, while the p-type semiconductor allows a selective electrical contact to the valence band. As is shown in Figure 1.2c, the potential-difference between the electrical contacts provides the photo-voltage V . This way, sunlight is converted into electrical energy. The electrical energy can be used directly, or stored for consumption at another time. A solar cell does not produce any pollution or harmful emission upon operation, but the Si-based solar cells have a relatively large energy-return time.

(a) p-type and n-type
Si-based semiconductor



(b) pn-homojunction



(c) operational solar cell

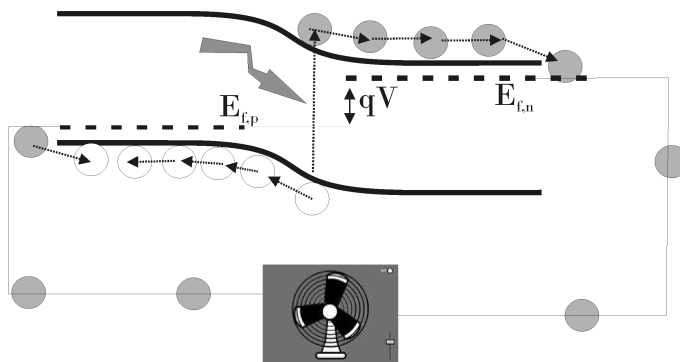


Figure 1.2: Principle of a homojunction Si-based solar cell. Graph (a) shows the band structure of a p-type and an n-type semiconductor. Graph (b) shows the pn-junction under illumination. Graph (c) shows the pn-junction under illumination in an external electrical circuit.

1.2.3 Types of solar cells

Homojunction solar cells

Different types of solar cells have been developed since the discovery of the PV effect. The most famous is the crystalline silicon solar cell. By doping silicon either n-type (Phosphorus doped) or p-type (Boron doped) silicon is formed. Upon joining the n-type and p-type silicon, a pn junction is established. Since one type of semiconductor material is used, solar cells based on this type of pn-junction are classified as homojunction solar cells.

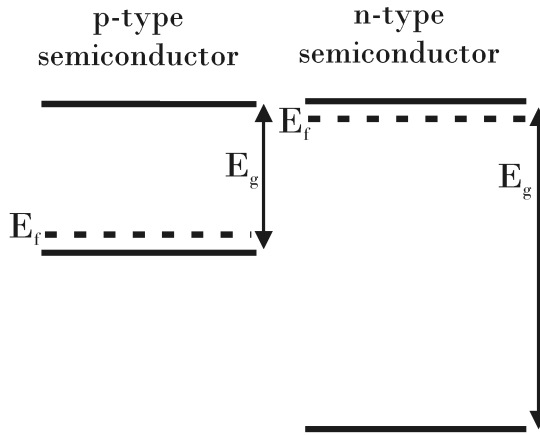
The largest disadvantage of the silicon solar cell is the high production costs of the silicon wafers, which are used in the production process of single crystalline and multi crystalline silicon solar cells. High temperature, high vacuum, and clean rooms are needed for the production of single-crystalline silicon solar cells. Currently, alternatives are being developed, such as amorphous silicon solar cells, which have reached an efficiency up to 9.5% at the time of writing⁵. Also, the development of the thin-film silicon solar cell is in progress. This way, the amount of material and thus the production costs can be reduced.

Heterojunction solar cells

Another type of solar cell consists of two different semiconductors, of which one is n-type and one is p-type. Joining the materials establishes a pn-junction, similar to the homojunction cell. Carefully selecting the material band structures leads to better solar cell efficiencies.

When the bandgaps of the two materials are not equal, the energy bands may not match perfectly, as is exemplified in Figure 1.3. Also in contrast to homojunction solar cells, the crystallographic properties of the n-type and p-type materials do not necessarily match. Among the hetero-junction solar cells, the window-layer design has attracted wide attention. In this design, the n-type semiconductor has a wide bandgap, which avoids the absorption of visible light by this part of the solar cell. In homojunction solar cells, the layers have to be as thin as possible to allow excited charge carriers to migrate to the junction before recombination occurs. In the window-layer design all visible-light absorption occurs in the p-type semiconductor. When a strong absorber is used in combination with illumination through a window layer, charge carrier generation within a small region close to the junction is secured⁷. This way, the migration-length of excited charge carriers to the junction is minimized, which lowers charge carrier recombination during the migration process. This increases the efficiency of the window-layer design solar cell. Widely known

(a) p-type and n-type semiconductor



(b) pn-heterojunction

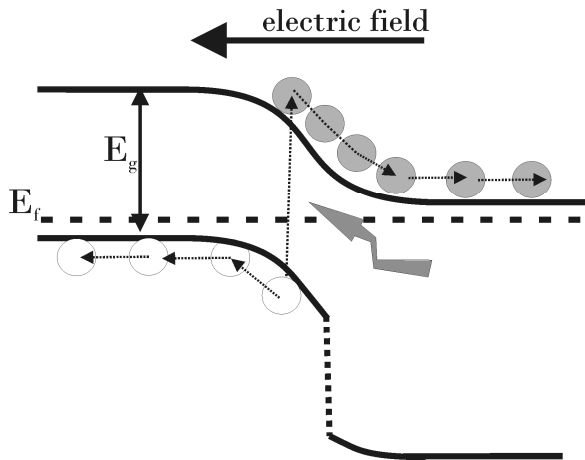


Figure 1.3: (a): p-type semiconductor and n-type wide-bandgap semiconductor. (b) pn-heterojunction.

heterojunction solar cells are based on combinations of GaAs, InP, CdTe, or Cu(In,Ga)(Se,S)₂ solar cells.

3D cell

The design of the Grätzel cell inspired researchers to further investigate new solar cell designs. The 3D concept is an example of an innovative solar cell design, in which the nano-porous TiO₂ structure is filled with a solid p-type semiconductor. This concept combines the benefit of the 3D structure with an all-solid-state solar cell, preventing the difficulties of using a liquid electrode. It is shown that a TiO₂ / CuInS₂ 3D solar cell has an efficiency of 5%⁸.

Although the 3D structure provides better solar cell efficiencies than thin film pn-junctions⁸, in this thesis only thin films are investigated. The 3D structure does not allow focusing on a single material since a nanoscaled mixture of different materials is present.

1.2.4 Synthesis of semiconductor solar cells

All semiconductor solar cells have in common that the substrate of the cell has to be transparent and conductive. Transparent Conductive Oxides (TCO's), such as SnO₂ (doped) or In₂O₃ (doped) have excellent properties to serve as a semiconductor substrate and electrical contact in one. TCO's can be easily deposited on glass, which forms a stable basis for solar cells.

Conventional deposition methods

Typical deposition methods for semiconductors include Chemical Vapor Deposition⁹, Sputter Deposition¹⁰, and Atomic Layer Deposition¹¹. These methods produce high-quality materials with optimal solar cell efficiencies. Usually, additional treatments are required after the deposition. All these deposition methods are classified as 'expensive', since high temperatures, a high vacuum, and often a clean environment are essential for producing high-quality materials. For solar cells for which a high efficiency is more important than low deposition costs, these deposition methods are the best choice.

Low-cost deposition methods

In order to reduce the production costs of solar cells, less expensive deposition methods have been developed. Chemical Spray Pyrolysis is a promising method. This method is developed during the last decades and shows promising results. Spray pyrolysis does not require extremely high temperatures,

a vacuum, or a clean room. The quality of the materials is lower than for conventional deposition methods, which lowers the efficiencies of the devices. The low production costs, however, increases the economical potential of the resulting solar cells. Other methods which are being investigated are electrodepositing and dip-coating. Low cost deposition methods become important when the costs of the solar cell are dominant to a high efficiency, i.e., in large area application.

1.3 Efficiency losses in semiconductors

1.3.1 Efficiency losses in semiconductor solar cells

The efficiency of a solar cell is determined by the percentage of solar energy that is converted into electrical energy. The amount of available solar energy is defined by the AM 1.5 solar spectrum. To achieve a high solar cell efficiency, the absorption of photons has to be large. A direct loss of solar energy is caused by photons that have an energy which is smaller than the bandgap. The ideal bandgap of a single-junction solar cell, with the most efficient absorption of the solar spectrum, is 1.4-1.6 eV¹².

The major energy-loss mechanisms of absorbed photons for a pn-junction solar cell are shown schematically in Figure 1.4¹³. Loss mechanism 1 is the relaxation of excited electrons and holes that have more energy than the bottom of the conduction band. This loss is responsible for a decrease in efficiency of 44%, when an optimal band-gap semiconductor is used. Loss mechanism 2 occurs when the excited charge carriers travel across the junction and loss mechanism 3 when the charge carriers are injected into the electronic contacts. The losses 1, 2 and 3 are part of the Queisser-Shockley limit, which predicts a maximum efficiency of 33% for single junction semiconductor solar cells¹⁴.

Loss mechanism 4 is the loss of excited electrons and holes that recombine before migration to the electronic contacts is completed. This type of loss is related to the material quality and physical properties and will be discussed in the next section.

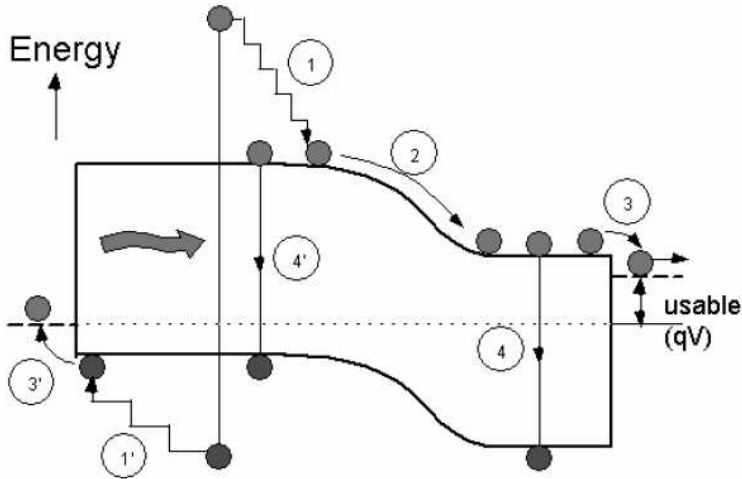


Figure 1.4: Major efficiency losses in single junction semiconductor solar cells.

1.3.2 *The recombination of electrons and holes*

The recombination of electrons and holes in pn-semiconductors is an important issue for semiconductor devices. In some devices, such as light-emitting diodes (LED's), a high recombination rate is preferred, while for solar cells a high recombination rate destroys the device operation. When recombination occurs, the (solar) energy is lost into the emission of photons or phonons. The current of a solar cell decreases directly with an increasing recombination rate. Recombination of electrons and holes can occur in the bulk-material or at interfaces.

Interface states

Missing atomic bonds at a surface or interface create defect states, i.e., surface states or interface states. Interface states are known as highly favorable recombination centers for electrons and holes, which reduce the solar cell efficiency strongly by encouraging electron-hole recombination at the junction. A buffer layer, which is a relatively thin layer between the p-and n-type semiconductor, slightly changes the electronic structure at the interface. This way, recombination of electrons and holes that occurs after the charge separation process has finished, is prevented¹⁵.

Bulk recombination mechanisms

The recombination in a bulk semiconductor is opposite to the excitation process. Recombination occurs when an excited electron is reduced in energy by filling a hole. Recombination can occur from the conduction band to the valence band, referred to as band-to-band or direct recombination, or through a defect state in the bandgap. The recombination mechanism in a semiconductor has been modeled by Shockley, Read and Hall^{16, 17} in 1952. Their so-called SRH-theory is widely used for modeling and explaining recombination mechanisms. This theory calculates the recombination rate from the statistical probability that an electron or a hole recombines. The model-parameters include the density of electrons in the conduction band, the density of holes in the valence band, the energy-level of the defect state, the density of defect states, the electron- or hole population of defect states, and the hole and electron capture cross sections.

Figure 1.5a shows schematically the recombination of electrons and holes for direct recombination and via a single defect state, according to the SRH model. External charge carrier generation changes the population density for both the valence- and the conduction band with respect to the equilibrium situation. Subsequent recombination induces a change in the defect-state population density. These changes in population density are described by differential equations that describe the corresponding recombination rate. For the valence- and conduction band, these differential equations read

$$\left(\frac{d\delta n}{dt} \right) = g - U_d - U_n \quad (1.1)$$

$$\left(\frac{d\delta p}{dt} \right) = g - U_d - U_p \quad (1.2).$$

in which δn is the deviation from the thermal equilibrium electron concentration in the conduction band, δp the deviation from the thermal equilibrium hole concentration in the valence band, g the charge carrier generation rate by external means, U_d the direct recombination rate, U_n the electron recombination rate to the defect state, and U_p the hole recombination rate to the defect state. For the defect state, the deviation from the thermal equilibrium electron population δN is

$$\frac{d\delta N}{dt} = U_n - U_p \quad (1.3)$$

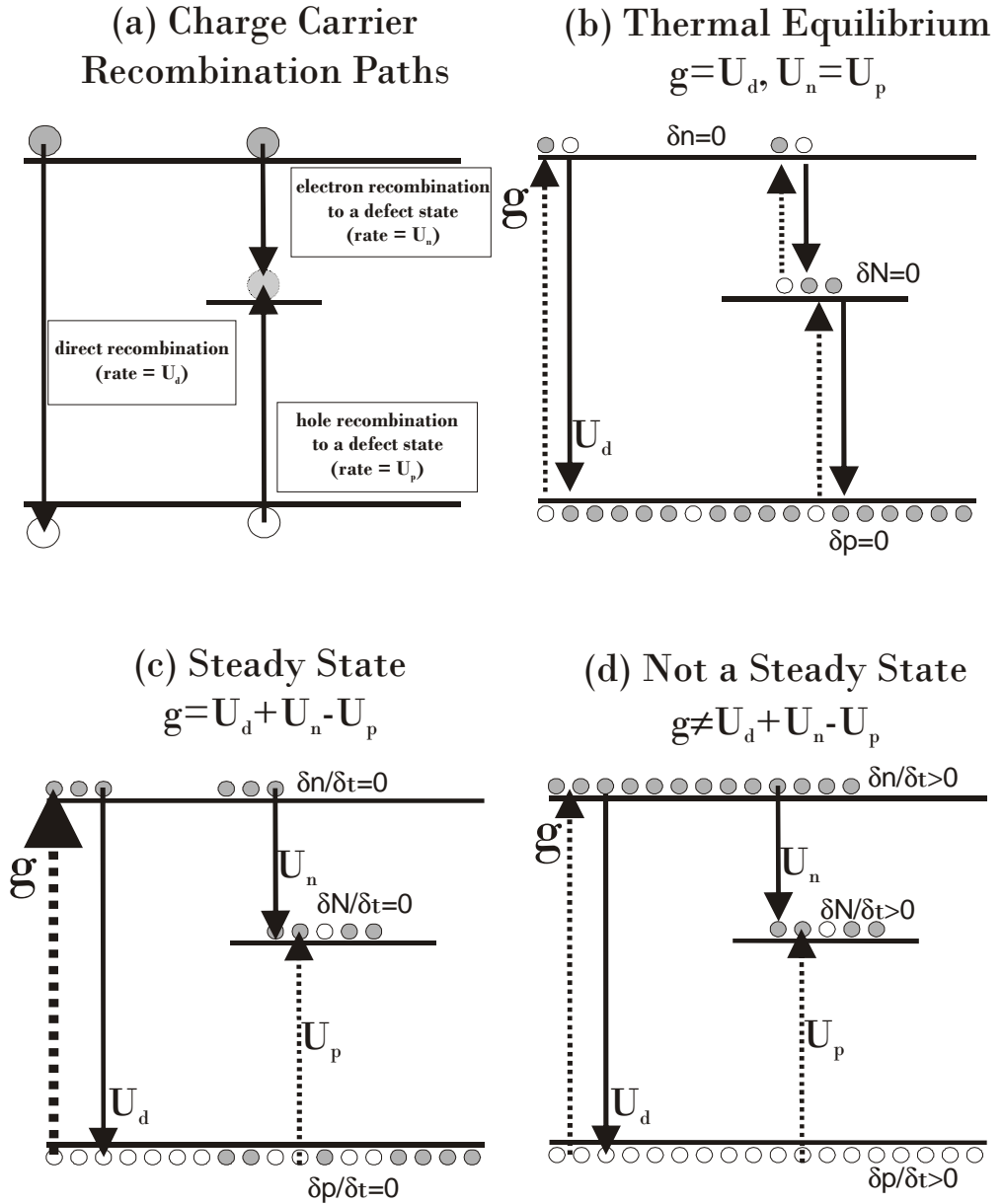


Figure 1.5: Charge carrier recombination models. (a) recombination paths, (b) system in thermal equilibrium, (c) system in steady-state, and (d) system not in a steady-state.

As is evident from Equation (1.3), the population density of electrons in the defect state increases when $U_p < U_n$ and decreases when $U_p > U_n$.

With the SRH model the recombination of optically excited charge carriers in semiconductors can be simulated. Three situations can be distinguished, which are shown in Figure 1.5b, c, and d.

I. The system is in thermal equilibrium.

Without any external charge carrier generation ($g=0$), the population densities do not change in time. The recombination rates are small, depending on the temperature.

II. The system is in a steady-state (but not in equilibrium).

When continuous charge carrier generation occurs ($g>0$), the system reaches a steady state after a stabilization time. The population densities do not change, but differ from the equilibrium value, as is indicated by the symbol δ . The recombination rates depend on the temperature and the generation rate, as well as the recombination parameters.

III. The system is not in a steady-state situation.

When, by external means, the system is not in a steady state situation, the population densities and the recombination rates will change with time, until a steady state or thermal equilibrium is reached

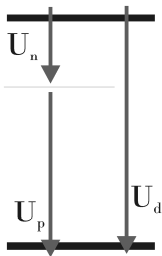
Situation II can be experimentally studied by means of photoluminescence spectroscopy. Situation III can be experimentally studied by using a pulsed excitation technique, as is described elsewhere in this thesis.

Multiple defect states

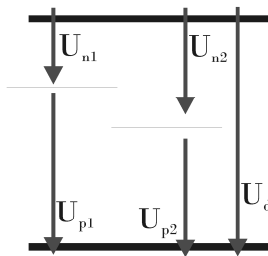
The SRH-theory is limited to a single defect in the bandgap of the semiconductor. Wertheim¹⁸ has extended the SRH-model to multiple defect states, as is shown in Figure 1.6b. Multiple defect states, which all act as an individual recombination center, are present in this model. Like the SRH-model, direct recombination is also present.

In this thesis, the model of Wertheim is extended to a mechanism in which also state-to-state recombination is involved, as is indicated by the bold arrow in Figure 1.6c. State-to-state recombination is allowed only when the corresponding crystallographic defects are located within tunneling distance to each other in the crystal. The differential equations that describe the state-to-state recombination model are coupled, which complicates the model. A general analytical solution does not exist, only numerical methods can handle these problems. Modern computational facilities enable the exploration of complicated recombination models.

Shockley-Read-Hall model



Wertheim Model



This Thesis

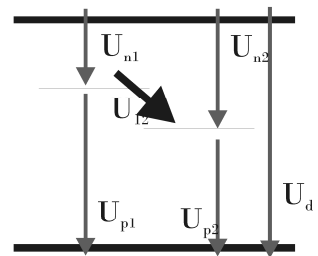


Figure 1.6: Electron-recombination mechanisms of (a) Shockley, Read and Hall, (b) Wertheim, and (c) this thesis. The recombination is shown from the electron point of view only.

1.4 CuInS₂

In the past decades, Cu-chalcopyrite materials have attracted wide attention for the application in solar cells^{5, 19}. The combination of a large bandgap (1.1 to 1.7 eV) and a high absorption coefficient (10⁵ cm⁻¹) are excellent for solar cell applications. The large bandgap has the ability for substantial absorption of the visible part of the solar spectrum. The high absorption coefficient is beneficial for use in thin-film solar cells, such as the window-layer design. The use of thin films reduces the production costs²⁰. Different Cu-chalcopyrite compounds have demonstrated photovoltaic activity, such as CuInSe₂²¹, Cu(In,Ga)Se₂²², CuInS₂²³, and CuGaSe₂²⁴.

This thesis focuses on the electro-optical properties of the chalcopyrite material CuInS₂. This material has several advantages with respect to other chalcopyrite-based materials. First of all, the bandgap of 1.55 eV^{25, 26} is ideal for optimal absorption of the solar spectrum. Second, unlike CuInSe₂, it does not contain the poisoning element Se. Third, CuInS₂ can be deposited by a cheap spray pyrolysis deposition^{8, 27-34}, which lowers the production costs.

For CuInS₂ materials the best solar cell efficiencies have been found for p-type CuInS₂ in combination with n-type window layers, such as TiO₂³⁵, ZnO³⁶, or In₂S₃^{27, 28}. To date, the maximum reported efficiency for a CuInS₂-based solar cell is 12.5% for a Mo/CuInS₂/CdS/ZnO cell³⁷. The theoretical efficiency of CuInS₂-based solar cells, however, is 28.5 %¹⁹.

1.4.1 Crystal structure and electronic properties of CuInS₂

CuInS₂ belongs to the I-III-VI₂ family of compounds. These ternary compounds are derived from the II₂-VI₂ sphalerites, where the two group-II atoms are replaced by one group-I atom and one group-III atom. The general notation for Cu-chalcopyrites yields Cu-B^{III}-C₂^{VI}. Upon crystallization, tetrahedra of Cu_nB(4-n)^{III} are formed around the C-atom. At low temperatures, the highest thermodynamically stable ordering is that of the chalcopyrite structure³⁸. The Cu-Au (copper-gold) ordering is closely related to the chalcopyrite structure. The formation-energy differs only 2 meV/atom³⁹ from that of the chalcopyrite structure. The crystal structure of the chalcopyrite ordering and the Cu-Au ordering are shown in Figure 1.7.

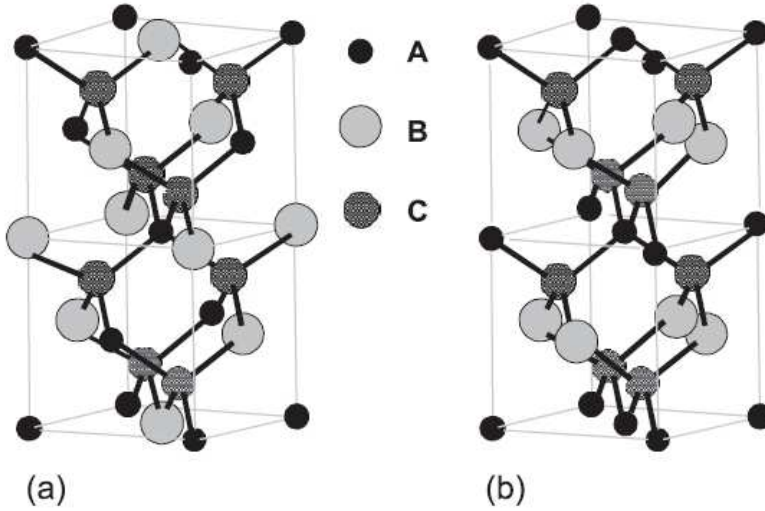


Figure 1.7: Atomic ordering for the ternary $\text{A}^{\text{I}}\text{B}^{\text{III}}\text{C}_2^{\text{VI}}$ compound in (a) the chalcopyrite structure and (b) the Cu-Au-like structure⁴⁰.

The crystal structure of CuInS_2 can be identified by Raman spectroscopy⁴¹⁻⁴³. This method is excellent to determine whether the material has the desired chalcopyrite structure or if the Cu-Au ordered structure is present. The chalcopyrite structure shows a Raman-peak at 295 cm^{-1} , while the Cu-Au ordered structure has a Raman-peak at 305 cm^{-1} . Figure 1.8 shows the Raman-spectrum for the chalcopyrite structure and for a mixture of the chalcopyrite structure and the Cu-Au ordered structure.

It is shown that the width of the chalcopyrite Raman-peak is related to the solar cell performance of CuInS_2 -based solar cells⁴⁴. Narrowing of the Full Width Half Maximum (FWHM) value of the chalcopyrite Raman-peak is found to be related to better solar cell efficiencies for CuInS_2 -based solar cell.

Ideally, the crystal structure of CuInS_2 follows that of Figure 1.7a, which holds for perfect crystalline chalcopyrite CuInS_2 . However, in reality this type of perfection is never reached. Material imperfections, such as vacancies, interstitial atoms, and substitutional atoms introduce local energy positions in the bandgap of the material. Also, a lattice distortion at interfaces can introduce imperfections. The application of cost-reducing deposition methods implies the use of low-purity chemicals (<99%), non-perfect atmospheric conditions and less control of the material growth. Therefore, material imperfections will increase when cost-reducing deposition methods are being applied. These imperfections include not only native defects, but also the crystal growth is not ideal.

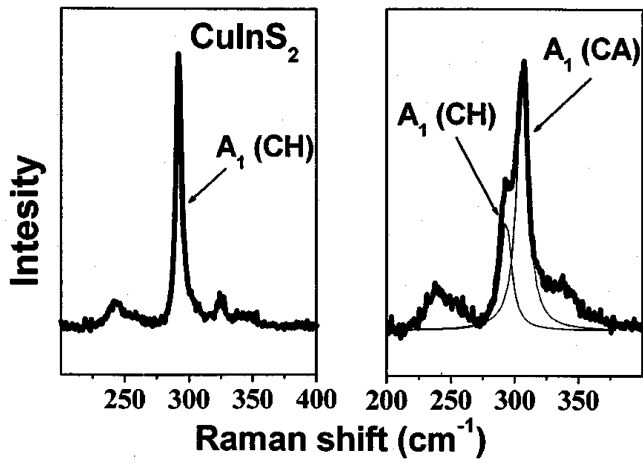
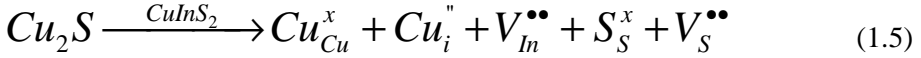
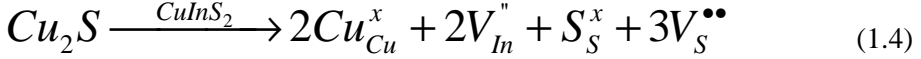


Figure 1.8: Raman spectrum of CuInS_2 , presenting only chalcopyrite (CH) ordering (left) and a mixture of CH and Cu-Au ordering (right)⁴¹.

1.4.2 Defect chemistry of Cu-rich CuInS₂

CuInS₂ can be either a p-type or an n-type semiconductor. Cu-rich CuInS₂ has p-type conductivity while the Cu-poor (In-rich) type has n-type conductivity^{45, 46}. For solar cells, p-type CuInS₂ is preferred, which means that the Cu-rich variant is used. In Cu-rich CuInS₂, the deviation from molecularity can be described by three defect reactions⁴⁷, which are



The most energetic favorable is Equation (1.6) because it involves the smallest number of defects with low electric charges. However, the probability of occurrence of the other equations is not completely excluded. According to Equations (1.4), (1.5), and (1.6) sulfur and indium vacancies are present to compensate for the excess of copper. These defects introduce energy-levels within the bandgap of Cu-rich CuInS₂.

1.4.3 Defect-levels in Cu-rich CuInS₂

Theoretical calculations of the position of the defect levels that arise from material imperfections are known for CuInSe₂^{39, 48, 49}, but not much for CuInS₂. The calculations of CuInSe₂ can be applied qualitatively to CuInS₂, since both compounds have a similar atomic structure. The exact position of the defect levels, however, has to be determined experimentally for CuInS₂. Defect states in the bandgap can be determined using photoluminescence (PL) spectroscopy. Shallow defects induce photoluminescence emission in the visible spectrum of the light, which are relatively easy to detect. The work of Binsma^{50, 51} pioneered the experimental determination of defects in CuInS₂ crystals in 1982. Ueng⁴⁶ extended this research and published a detailed description of the defect states in CuInS₂. Figure 1.9 summarizes the most important defects that can be present in p-type (Cu-rich) CuInS₂.

Deep defect states

Deep defect states have energy levels that are situated more in the center of the bandgap. Recombination of electrons and holes that occurs between the deep defect states, as well as state-to-state recombination, emits a photon with an energy that is below 1.2 eV. These photons are in the near infrared spectrum of the light, which is not easy to detect, especially when the emission is weak. The existence of deep defects in Cu-chalcopyrite crystals is recently discovered, but their exact position and physical origin is still a subject of debate. PL measurements have shown that deep defect states are present^{44, 52-55}. Also in this thesis, evidence for deep defect states is presented.

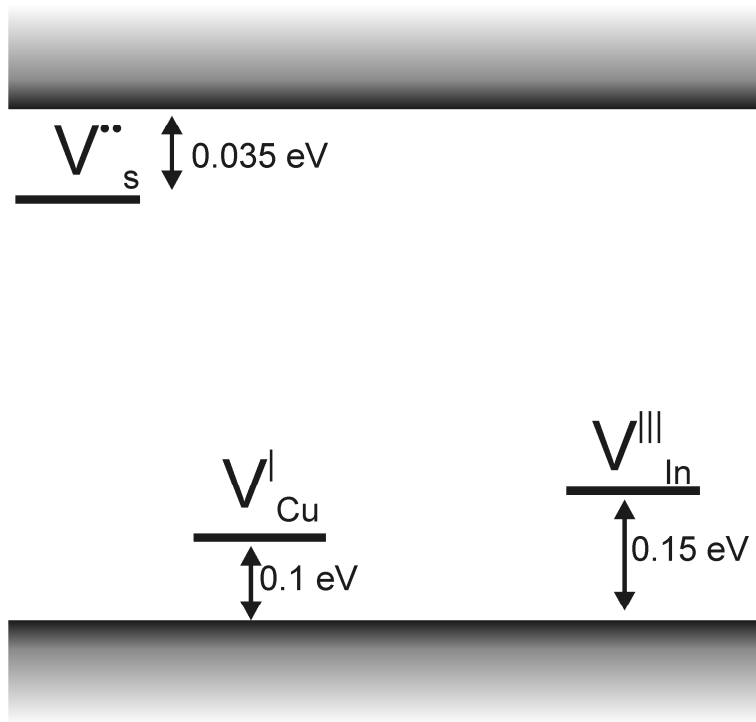


Figure 1.9: Shallow defects in CuInS₂

1.5 Aim and outline of this thesis

The application of cost-reducing deposition methods for chalcopyrite solar cells increases the density of material imperfections, which affects the electron recombination rate and decreases the solar cell efficiency. In order to increase the solar cell efficiency, it is important to obtain knowledge of the recombination mechanisms of the excited electrons.

In this thesis, steady-state and time-resolved optical methods are used to determine the behavior of excited electrons in CuInS₂. Based on the experimental results, the recombination mechanisms of the electrons are modeled, using semiconductor physics. The developed models, therefore, are applicable to a wide range of solar cells materials.

Also, the influence of a heterojunction on the dynamics of electrons is investigated for TiO₂/CuInS₂ heterojunction solar cells. For this purpose, Time-of-Flight measurements have been applied to actual solar cell structures. The role of surface states has been elaborated in detail.

Chapter 2 describes how Time-of-Flight measurements provide information about the surface states in CuInS₂/TiO₂ heterojunctions. An electrostatic model supports the experimental findings. Chapter 3 describes how transient absorption experiments provide information about the recombination mechanism and defect structure of CuInS₂ thin films. These experiments are carefully modeled and from the simulations important conclusions about the recombination mechanism of CuInS₂ can be drawn. Chapter 4 describes PL experiments on CuInS₂ thin films, which are performed as a function of excitation power. The recombination mechanism is modeled and applied to the PL experiments. In Chapter 5, transient absorption experiments, as well as Raman-spectroscopy and PL experiments are applied to spray-deposited CuInS₂, before and after heat-treatment. These experiments show how defect association is involved in the recombination of electron-hole pairs.

REFERENCES

- [1] M. Ito, K. Kato, K. Komoto, T. Kichimi and K. Kurokawa, "A comparative study on cost and life-cycle analysis for 100 MW very large-scale PV (VLS-PV) systems in deserts using m-Si, a-Si, CdTe, and CIS modules", *Progress in Photovoltaics* **2008**, 16, 17-30
- [2] D. Ginley, M. A. Green and R. Collins, "Solar energy conversion toward 1 terawatt", *Mrs Bulletin* **2008**, 33, 355-364
- [3] A. E. Becquerel, *Comt. Rend. Acad. Sci* **1839**, 9, 561
- [4] D. M. Chapin, C. S. Fuller and G. L. Pearson, "A New Silicon P-N Junction Photocell for Converting Solar Radiation into Electrical Power", *Journal of Applied Physics* **1954**, 25, 676-677
- [5] M. A. Green, K. Emery, Y. Hishikawa and W. Warta, "Solar cell efficiency tables (version 32)", *Progress in Photovoltaics* **2008**, 16, 435-440
- [6] M. A. Green, "Third generation photovoltaics: Ultra-high conversion efficiency at low cost", *Progress in Photovoltaics* **2001**, 9, 123-135
- [7] F. M. Livingstone, W. M. Tsang, A. J. Barlow, R. M. Delarue and W. Duncan, "Si-Cds Heterojunction Solar-Cells", *Journal of Physics D-Applied Physics* **1977**, 10, 1959-1963
- [8] M. Nanu, J. Schoonman and A. Goossens, "Nanocomposite three-dimensional solar cells obtained by chemical spray deposition", *Nano Letters* **2005**, 5, 1716-1719
- [9] L. Reijnen, B. Meester, A. Goossens and J. Schoonman, "Chemical vapor deposition of Cu_xS: Surface contamination by reaction products", *Chemistry of Materials* **2005**, 17, 4142-4148
- [10] H. L. Hwang, C. L. Cheng, L. M. Liu, Y. C. Liu and C. Y. Sun, "Growth and Properties of Sputter-Deposited CuInS₂ Thin-Films", *Thin Solid Films* **1980**, 67, 83-93
- [11] M. Nanu, L. Reijnen, B. Meester, J. Schoonman and A. Goossens, "CuInS₂ thin films deposited by ALD", *Chemical Vapor Deposition* **2004**, 10, 45-49
- [12] M. A. Green, "Solar cells", *Prentice-Hall series in solid state physical electronics* **1982**, 274 blz.
- [13] M. A. Green, "Photovoltaic principles", *Physica E* **2002**, 14, 11-17
- [14] W. Shockley and H. J. Queisser, "Detailed Balance Limit of Efficiency of P-N Junction Solar Cells", *Journal of Applied Physics* **1961**, 32, 510-&
- [15] S. Siebentritt, "Alternative buffers for chalcopyrite solar cells", *Solar Energy* **2004**, 77, 767-775
- [16] R. N. Hall, "Electron-Hole Recombination in Germanium", *Physical Review* **1952**, 87, 387-387
- [17] W. Shockley and W. T. Read, "Statistics of the Recombinations of Holes and Electrons", *Physical Review* **1952**, 87, 835-842

- [18] G. K. Wertheim, "Transient Recombination of Excess Carriers in Semiconductors", *Physical Review* **1958**, 109, 1086-1091
- [19] S. Siebentritt, "Wide gap chalcopyrites: material properties and solar cells", *Thin Solid Films* **2002**, 403, 1-8
- [20] I. Kaiser, K. Ernst, C. H. Fischer, R. Könenkamp, C. Rost, I. Sieber and M. C. Lux-Steiner, "The eta-solar cell with CuInS₂: A photovoltaic cell concept using an extremely thin absorber (eta)", *Solar Energy Materials and Solar Cells* **2001**, 67, 89-96
- [21] J. A. M. AbuShama, S. Johnston, T. Moriarty, G. Teeter, K. Ramanathan and R. Noufi, "Properties of ZnO/CdS/CuInSe₂ solar cells with improved performance", *Progress in Photovoltaics* **2004**, 12, 39-45
- [22] A. M. Gabor, J. R. Tuttle, D. S. Albin, M. A. Contreras, R. Noufi and A. M. Hermann, "High-Efficiency CuIn_xGa_{1-x}Se₂ Solar-Cells Made from (In_xGa_{1-x})₂Se₃ Precursor Films", *Applied Physics Letters* **1994**, 65, 198-200
- [23] K. Siemer, J. Klaer, I. Luck, J. Bruns, R. Klenk and D. Braunig, "Efficient CuInS₂ solar cells from a rapid thermal process (RTP)", *Solar Energy Materials and Solar Cells* **2001**, 67, 159-166
- [24] M. Saad, H. Riaz, E. Bucher and M. C. LuxSteiner, "CuGaSe₂ solar cells with 9.7% power conversion efficiency", *Applied Physics a-Materials Science & Processing* **1996**, 62, 181-185
- [25] M. Kanzari and B. Rezig, "Effect of deposition temperature on the optical and structural properties of as-deposited CuInS₂ films", *Semiconductor Science and Technology* **2000**, 15, 335-340
- [26] R. Klenk, U. Blieske, V. Dieterle, K. Ellmer, S. Fiechter, I. Hengel, A. JägerWaldau, T. Kampschulte, C. Kaufmann, J. Klaer, M. C. LuxSteiner, D. Braunger, D. Hariskos, M. Ruckh and H. W. Schock, "Properties of CuInS₂ thin films grown by a two-step process without H₂S", *Solar Energy Materials and Solar Cells* **1997**, 49, 349-356
- [27] T. T. John, C. S. Kartha, K. P. Vijayakumar, T. Abe and Y. Kashiwaba, "Modification in cell structure for better performance of spray pyrolysed CuInS₂/In₂S₃ thin film solar cell", *Applied Physics a-Materials Science & Processing* **2006**, 82, 703-707
- [28] T. T. John, M. Mathew, C. S. Kartha, K. P. Vijayakumar, T. Abe and Y. Kashiwaba, "CuInS₂/In₂S₃ thin film solar cell using spray pyrolysis technique having 9.5% efficiency", *Solar Energy Materials and Solar Cells* **2005**, 89, 27-36
- [29] M. Krunks, O. Bijakina, V. Mikli, H. Rebane, T. Varema, M. Altosaar and E. Mellikov, "Sprayed CuInS₂ thin films for solar cells: The effect of solution composition and post-deposition treatments", *Solar Energy Materials and Solar Cells* **2001**, 69, 93-98
- [30] M. Krunks, O. Bijakina, T. Varema, V. Mikli and E. Mellikov, "Structural and optical properties of sprayed CuInS₂ films", *Thin Solid Films* **1999**, 338, 125-130
- [31] M. Krunks, O. Kijatkina, H. Rebane, I. Oja, V. Mikli and A. Mere, "Composition of CuInS₂ thin films prepared by spray pyrolysis", *Thin Solid Films* **2002**, 403, 71-75
- [32] M. Krunks, V. Mikli, O. Bijakina, H. Rebane, A. Mere, T. Varema and E. Mellikov, "Composition and structure of CuInS₂ films prepared by spray pyrolysis", *Thin Solid Films* **2000**, 361, 61-64

- [33] R. O'Hayre, M. Nanu, J. Schoonman, A. Goossens, Q. Wang and M. Gratzel, "The influence of TiO₂ particle size in TiO₂/CuInS₂ nanocomposite solar cells", *Advanced Functional Materials* **2006**, 16, 1566-1576
- [34] I. Oja, M. Nanu, A. Katerski, M. Krunks, A. Mere, J. Raudoja and A. Goossens, "Crystal quality studies of CuInS₂ films prepared by spray pyrolysis", *Thin Solid Films* **2005**, 480, 82-86
- [35] M. Nanu, L. Reijnen, B. Meester, A. Goossens and J. Schoonman, "CuInS₂-TiO₂ heterojunctions solar cells obtained by atomic layer deposition", *Spring Meeting of the European-Materials-Research-Society (E-MRS)* **2002**, 492-496
- [36] A. M. Chaparro, M. T. Gutierrez, J. Herrero, J. Klaer, M. J. Romero and M. M. Al-Jassim, "Characterisation of CuInS₂/Zn(Se,O)/ZnO solar cells as a function of Zn(Se,O) buffer deposition kinetics in a chemical bath", *Progress in Photovoltaics* **2002**, 10, 465-480
- [37] J. Klaer, J. Bruns, R. Henninger, K. Seimer, R. Klenk, K. Ellmer and D. Braunig, "Efficient CuInS₂ thin-film solar cells prepared by a sequential process", *Semiconductor Science and Technology* **1998**, 13, 1456-1458
- [38] J. J. M. Binsma, L. J. Giling and J. Bloem, "Phase-Relations in the System Cu₂s-In₂s₃", *Journal of Crystal Growth* **1980**, 50, 429-436
- [39] S. B. Zhang, S. H. Wei, A. Zunger and H. Katayama-Yoshida, "Defect physics of the CuInSe₂ chalcopyrite semiconductor", *Physical Review B* **1998**, 57, 9642-9656
- [40] C. Guillen, J. Herrero, M. T. Gutierrez and F. Briones, "Structure, morphology and optical properties of CuInS₂ thin films prepared by modulated flux deposition", *Thin Solid Films* **2005**, 480, 19-23
- [41] J. Alvarez-Garcia, B. Barcones, A. Perez-Rodriguez, A. Romano-Rodriguez, J. R. Morante, A. Janotti, S. H. Wei and R. Scheer, "Vibrational and crystalline properties of polymorphic CuInC₂ (C=Se,S) chalcogenides", *Physical Review B* **2005**, 71, -
- [42] J. Alvarez-Garcia, J. Marcos-Ruzafa, A. Perez-Rodriguez, A. Romano-Rodriguez, J. R. Morante and R. Scheer, "MicroRaman scattering from polycrystalline CuInS₂ films: structural analysis", *Thin Solid Films* **2000**, 361, 208-212
- [43] J. Alvarez-Garcia, A. Perez-Rodriguez, A. Romano-Rodriguez, J. R. Morante, L. Calvo-Barrio, R. Scheer and R. Klenk, "Microstructure and secondary phases in coevaporated CuInS₂ films: Dependence on growth temperature and chemical composition", *Journal of Vacuum Science & Technology a-Vacuum Surfaces and Films* **2001**, 19, 232-239
- [44] E. Rudigier, T. Enzenhofer and R. Scheer, "Determination of the quality of CuInS₂-based solar cells combining Raman and photoluminescence spectroscopy", *Thin Solid Films* **2005**, 480, 327-331
- [45] D. C. Look and J. C. Manthuruthil, "Electron and Hole Conductivity in CuInS₂", *Journal of Physics and Chemistry of Solids* **1976**, 37, 173-180
- [46] H. Y. Ueng and H. L. Hwang, "The Defect Structure of CuInS₂ .I. Intrinsic Defects", *Journal of Physics and Chemistry of Solids* **1989**, 50, 1297-1305
- [47] D. Perniu, S. Vouwzee, A. Duta and J. Schoonman, "Defect chemistry of solar cell chalcopyrite materials", *Journal of Optoelectronics and Advanced Materials* **2007**, 9, 1568-1571

- [48] S. H. Wei, L. G. Ferreira and A. Zunger, "1st-Principles Calculation of the Order-Disorder Transition in Chalcopyrite Semiconductors", *Physical Review B* **1992**, 45, 2533-2536
- [49] S. H. Wei and S. B. Zhang, "Defect properties of CuInSe₂ and CuGaSe₂", *Journal of Physics and Chemistry of Solids* **2005**, 66, 1994-1999
- [50] J. J. M. Binsma, L. J. Giling and J. Bloem, "Luminescence of CuInS₂ .2. Exciton and near Edge Emission", *Journal of Luminescence* **1982**, 27, 55-72
- [51] J. J. M. Binsma, L. J. Giling and J. Bloem, "Luminescence of CuInS₂ .1. The Broad-Band Emission and Its Dependence on the Defect Chemistry", *Journal of Luminescence* **1982**, 27, 35-53
- [52] J. Krustok, J. Raudoja and H. Collan, "Photoluminescence and the tetragonal distortion in CuInS₂", *Thin Solid Films* **2001**, 387, 195-197
- [53] J. Krustok, J. Raudoja, J. H. Schon, M. Yakushev and H. Collan, "The role of deep donor-deep acceptor complexes in CIS-related compounds", *Thin Solid Films* **2000**, 361, 406-410
- [54] J. Krustok, J. H. Schon, H. Collan, M. Yakushev, J. Madasson and E. Bucher, "Origin of the deep center photoluminescence in CuGaSe₂ and CuInS₂ crystals", *Journal of Applied Physics* **1999**, 86, 364-369
- [55] T. Onishi, K. Abe, Y. Miyoshi, K. Wakita, N. Sato and K. Mochizuki, "Study of deep photoluminescence levels in CuInS₂ crystals", *Journal of Physics and Chemistry of Solids* **2005**, 66, 1947-1949

Time-of-Flight studies on TiO₂ / CuInS₂ heterojunctions

Abstract

Time-of-Flight (ToF) measurements have been performed on n-type TiO₂ / p-type CuInS₂ (CIS) heterojunctions. The TiO₂ film thickness has been varied between 200 and 400 nm, while the CuInS₂ film thickness has been fixed at 500 nm. The ToF response can be accurately modeled, if the potential drop across the pn-heterojunction with a large density of interface states is properly accounted for. Also electron transport in a space-charge region for a not fully depleted semiconductor has to be considered. The electron mobility in TiO₂ is found to be $10^{-2} \text{ cm}^2 \text{ V}^{-1} \text{ s}^{-1}$, independent of the TiO₂ layer thickness. The interface-state densities are 5×10^{11} , 2×10^{12} and $6 \times 10^{12} \text{ eV}^{-1} \text{ cm}^{-2}$ for 200, 300 and 400 nm thick TiO₂ films, respectively.

2.1 Introduction

In order to reduce the energy payback time and the production costs of solar cells, alternative materials and device concepts need to be developed. In the past years, research in our laboratory has been focused on the development of all solid-state 3D solar cells¹⁻³, in which n-type and p-type semiconductors are blended on a nanometer scale. Nanocomposites of anatase TiO₂ and CuInS₂, with In₂S₃ as a buffer layer, exhibit an energy conversion efficiency of about 5%³. Since these solar cells have been obtained by spray pyrolysis in air at a substrate temperature of about 300°C, the economical potential for this device concept has been demonstrated convincingly. Spray pyrolysis⁴⁻⁸ is a simple technique open to large-scale production of thin-film solar cells. Obviously, the material quality is less than that obtained with more advanced technologies and relative high defect concentrations can be expected. Defects in CuInS₂, i.e. interstitials, vacancies, impurities, and anti-sites defects (copper-gold ordering) have a negative effect on the energy conversion efficiency, since they reduce the lifetime and mobility of the charge carriers⁹.

In chalcopyrite-based photovoltaic devices, a heterojunction between the chalcopyrite-structured absorber and the n-type buffer material is formed. Formation of a heterojunction can give rise to interface states, which reduce the efficiency of the device when energy levels are located in the bandgap of the light-absorbing material. When the interface state concentration is high Fermi-level pinning may occur, which affects the internal electric field at the junction^{10, 11}. Not much is known about the influence of interface states on the charge carrier transport in chalcopyrite-based solar cells. The present study is directed to elucidate the relationship between the density of interface states and the charge carrier dynamics in TiO₂/CuInS₂ heterojunctions using the Time-of-Flight (ToF) technique. In ToF, a short laser pulse creates charge carriers at the TiO₂ / CuInS₂ junction, which drift away from the junction region by the internal electric field. The mobile charges are detected using two non-blocking electrodes. In this way, the samples under investigation are solar cells and the outcome of ToF experiments is closely related to the transport of carriers in solar cells under operational conditions.

The magnitude of the internal electric field at the local junctions in nanocomposites is difficult to determine. Therefore, in the present study thin-film bi-layer devices are investigated instead of 3D nanocomposites.

2.1.1 Time-of-Flight background

With the Time-of-Flight technique, the transport time of a sheet of charge carriers through a material is measured¹². Charge carriers, which are generated by laser-induced excitation, drift through a sample between the electrodes under the influence of an applied electric field. If the width of the sheet of charge carriers is small compared to the thickness of the film, the carrier transit time can be detected. The width of the sheet of charge carriers is related to the duration of the laser pulse and is broadening somewhat during the flight¹³. The transit time τ is defined as the moment when half of the charge carriers has crossed the sample. In the simplest case, the mobility follows from

$$\mu = \frac{v}{E} = \frac{d/\tau}{E}, \quad (2.1)$$

where μ and v are the charge carrier mobility and velocity, respectively, E is the electric field, d the sample thickness, and τ the transit time. A relation between the transit time and the electric field can be derived from Equation (2.1),

$$\frac{1}{\tau} = \frac{\mu}{d} E = \frac{\mu}{d^2} V \quad (2.2)$$

in which V is the applied bias, which in this approximation decreases linearly over the thickness of the sample. A plot of $1/\tau$ as a function of V will show a straight line of which the slope relates to the mobility of the charge carrier.

Several important conditions need to be fulfilled in a well-performed Time-of-Flight experiment. First, the generated charge should be much less than the surface charge on the electrodes, to ensure that the internal electric field is not affected by the injected charge carriers¹⁴. Second, to freeze-in slow dielectric relaxation, the DC voltage must be applied just before the laser pulse¹⁴. Third, the response time of the electrical measurement system (including the sample) must be less than the transit time. If not, the measured current response is affected by the instrumental bandwidth¹⁴. Fourth, changing the thickness of the film should not affect the derived carrier mobility when non-dispersive transport is considered.

2.1.2 Time-of-Flight on pn-heterojunctions

The aim of this work is to measure the transport of charge carriers in n-TiO₂ / p-CuInS₂ heterojunctions. In contrast to conventional ToF experiments, two semiconductor materials, instead of one, are involved. However, if one of the two semiconductors has a much higher charge carrier mobility than the other, it merely acts as an electrical contact for the semiconductor with the low charge carrier mobility. In that case, the only difference with the normal ToF experiment is, that the applied voltage is divided over both semiconductors, which implies that the local electric field is not simply V/d . To determine which of the two semiconductors has the lowest charge carrier mobility, the film thickness of both layers has been varied. It appears that in TiO₂ / CuInS₂ heterojunctions the electron mobility in TiO₂ is much smaller than the hole mobility in CuInS₂. By measuring the electron transit time in TiO₂ it is possible to assess the voltage distribution in TiO₂ / CuInS₂ heterojunctions, which depends strongly on the electronic properties of the TiO₂ / CuInS₂ interface.

To relate the measured transit-time values with the applied bias voltage and the film thickness, a model of the TiO₂ / CuInS₂ heterojunction has been elaborated, which is further discussed below.

2.2 Experimental aspects

Both the TiO₂ and the CuInS₂ films have been deposited on SnO₂-coated glass substrates (TCO) using automated aerosol spray-pyrolysis. More information about the synthesis of TiO₂ and CuInS₂ can be found in references⁴⁻⁸. The back contact is a vacuum-evaporated disc of gold with a diameter of 2 mm. Carbon paint is used to make electrical contact with the TCO front electrode. Three samples have been investigated, in which the CuInS₂ layer thickness is kept at 500 nm and the TiO₂ thickness was varied, i.e., 200, 300 and 400 nm. Figure 2.1 schematically describes the Time-of-Flight setup. A Nd-YAG laser (SpectraPhysics QCR) operating at 355 nm, 7 ns pulse width and 10 Hz repetition rate, pumps a MOPO (SpectraPhysics MOPO 710). After passing through several neutral density filters and a pinhole, the energy of the pulse is 0.5 μJ/cm². A fast photodiode is used to trigger the detecting electronics. A pulse generator (Agilent) provides the voltage pulse. The exact timing of the applied voltage pulse is set using the delay-option of the pulse generator. An oscilloscope (Tektronix TDS 744), being triggered by the photodiode, records the photocurrent through its internal 50 Ohm resistance. To measure the dark current at the applied voltage an electronic shutter is closed. The samples are mounted in a liquid-nitrogen cooled cryostat (Oxford Optistat DN) for stabilizing and varying the temperature.

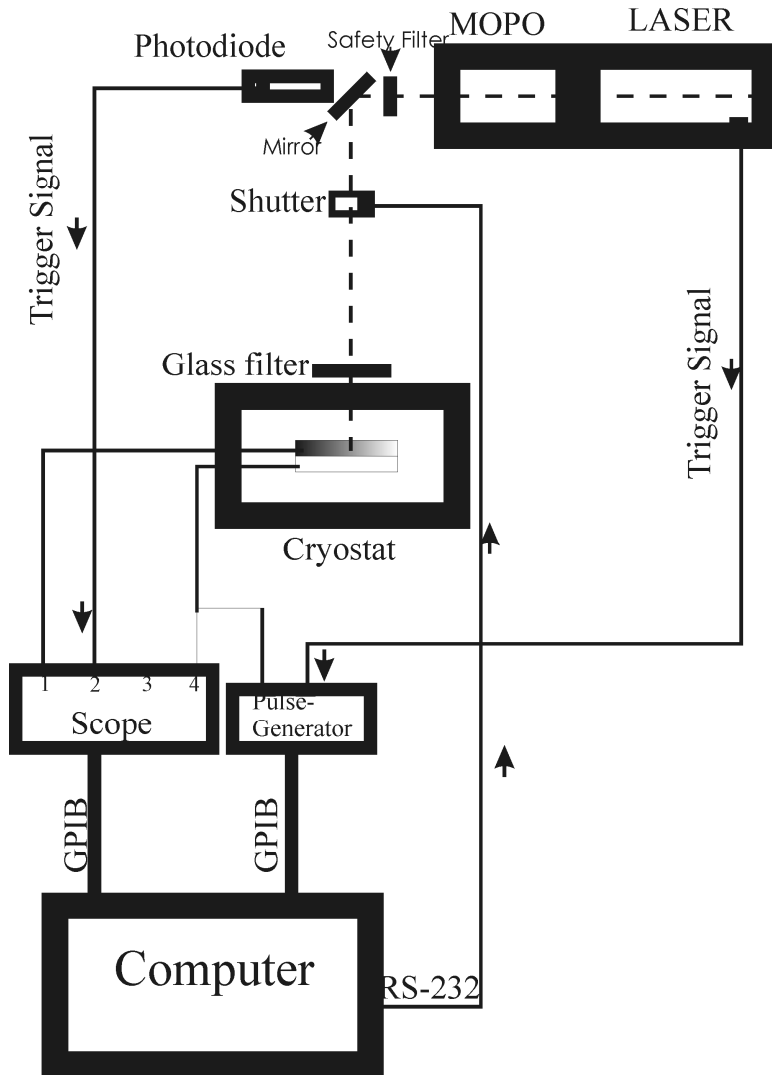


Figure 2.1: Schematical representation of the ToF setup. The solid lines represent electrical wiring. The dashed line represents the laser path. The sample is mounted in an LN-cooled cryostat. The complete experiment is computer controlled.

2.3 Results

Figure 2.2 shows a typical IV-curve in the dark and under illumination for a TiO₂/ CuInS₂ heterojunction with a TiO₂ thickness of 300 nm. The sample shows good diode behavior with a rectification ratio at +/- 1 volt of 10³. Charge extraction experiments have been performed. In these experiments, the bias voltage is set at 0 for some time. At t=0, the bias voltage is stepped to a reverse bias (i.e. -1 volt) and the current transient is measured. The current response shows an exponential decay with a time constant of 10⁻⁶ (s), as shown in the inset of Figure 2.3. The area under the curve represents the extracted charge, which is plotted in Figure 2.3 as a function of applied bias. A linear relation between the extracted charge and the applied bias is found. The ratio between the extracted charge Q and the voltage V , i.e., $\Delta Q/\Delta V$ is the cell capacitance, which is 8×10^{-7} F/cm².

Figure 2.4 shows a ToF photocurrent response on a linear scale. The ToF response shows only a very weak temperature dependence between 260 and 310 K. The area under the ToF curve represents a charge of 10⁻¹⁰ coulomb. For a 300 nm thick sample, with a diameter of 2 mm, the injected charge density amounts to 10¹⁴ cm⁻³, which is well below the donor density in TiO₂ of about 10¹⁷ cm⁻³. Accordingly, the injected charge carriers do not disturb the internal electric field.

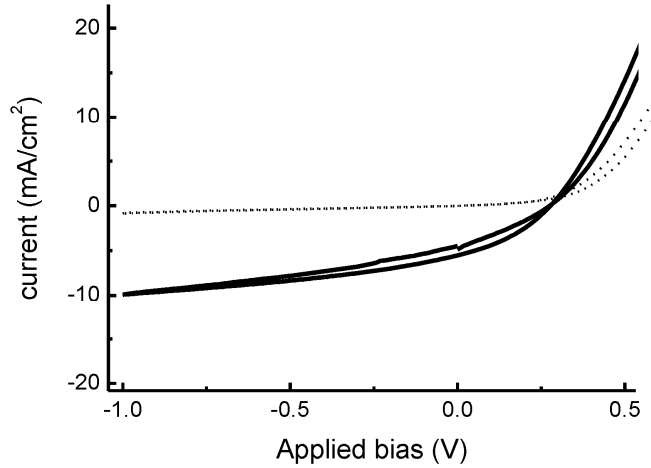


Figure 2.2: IV-curves for the 300 nm TiO_2 sample in the dark (dashed line) and under illumination (solid line).

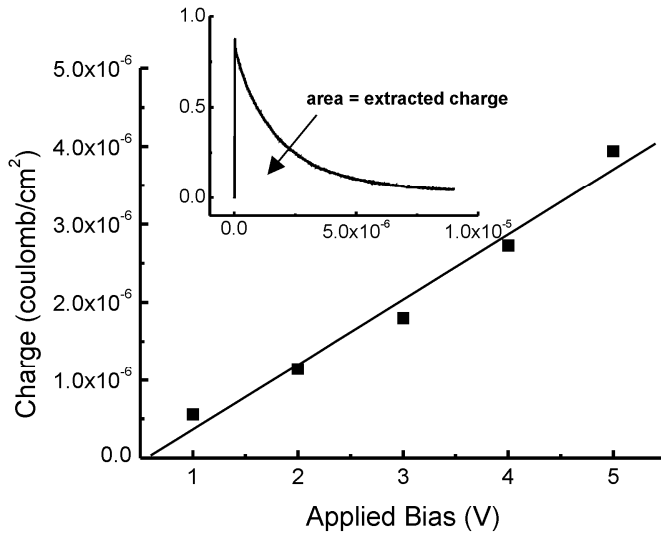


Figure 2.3: Charge extraction measurements. Extracted charge for a 300 nm thick TiO_2 sample. The inset shows the current response after applying a bias step of 2 V.

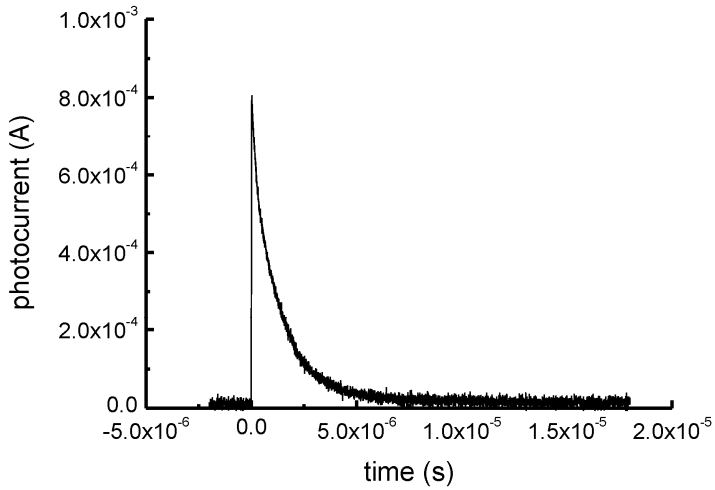


Figure 2.4: Time-of-Flight photocurrent on a linear scale for a 400 nm thick TiO₂ sample at an applied bias of 2.5 V.

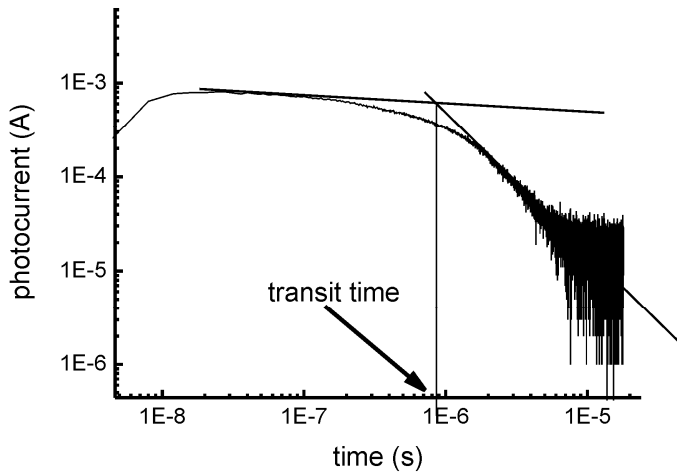


Figure 2.5: Time-of-Flight photocurrent from Figure 2.4 on a log-log scale. The transit time is found from the intersects of the tangents .

As can be seen from Figure 2.4, it is impossible to determine the transit time from this graph in a direct way. Figure 2.5, therefore, shows the same transient on a log-log scale. The transit time is indicated in the figure. Plots of $1/\tau$ as a function of the applied DC bias are presented in Figure 2.6 for all three samples at a temperature of 290 K. For voltages less than 1.5 V the transit time is almost independent of the applied bias. For voltages above 1.5 V, $1/\tau$ is voltage dependent, but the voltage and the film thickness dependence do not follow Equation (2.2). Furthermore, the transit time changes with the TiO₂ layer thickness and does not change upon variation of the CuInS₂ layer thickness (not shown). We conclude that the current response is related to the transport of electrons in TiO₂.

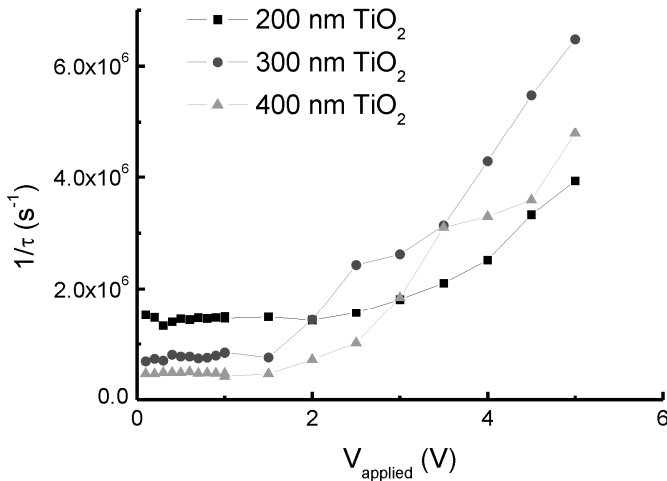


Figure 2.6: The transit time as a function of the applied voltage for 200, 300 and 400 nm thick TiO₂ samples.

2.4 Discussion

From the charge extraction measurements a capacitance of $8 \times 10^{-7} \text{ Fcm}^{-2}$ is found. When comparing this capacitance with a parallel plate capacitance with a dielectric constant of 10 (for CuInS₂), a thickness of about 10 nm is found, which is well below the thickness of the TiO₂ and CuInS₂ films. We conclude that this huge capacitance is not due to space charge formation, but is related to the presence of a high density of interface states. This indicates that storage of charge in interface states is substantial and cannot be neglected. Furthermore, the donor and acceptor densities found for TiO₂ and CuInS₂ are $N_d=10^{17}$ and $N_a=10^{16}$, respectively, as has been determined in previous investigations¹⁵. Therefore, we cannot expect that full depletion is reached in the TiO₂ films at the applied voltages. Accordingly, the assumption that the electric field is constant throughout the TiO₂ layer cannot be made in our case.

In order to interpret the ToF results a model is developed for the potential distribution in a pn junction with interface states and with one of the components (CuInS₂) in full depletion. Next, a charge transport model is developed, in which the inhomogeneous electric field is incorporated. With the aid of these models the ToF results can be explained accurately. By fitting the model parameters to the ToF response, it is possible to determine the concentration and the neutrality level of the interface states, which is of paramount importance for understanding the device physics of CIS-based solar cells.

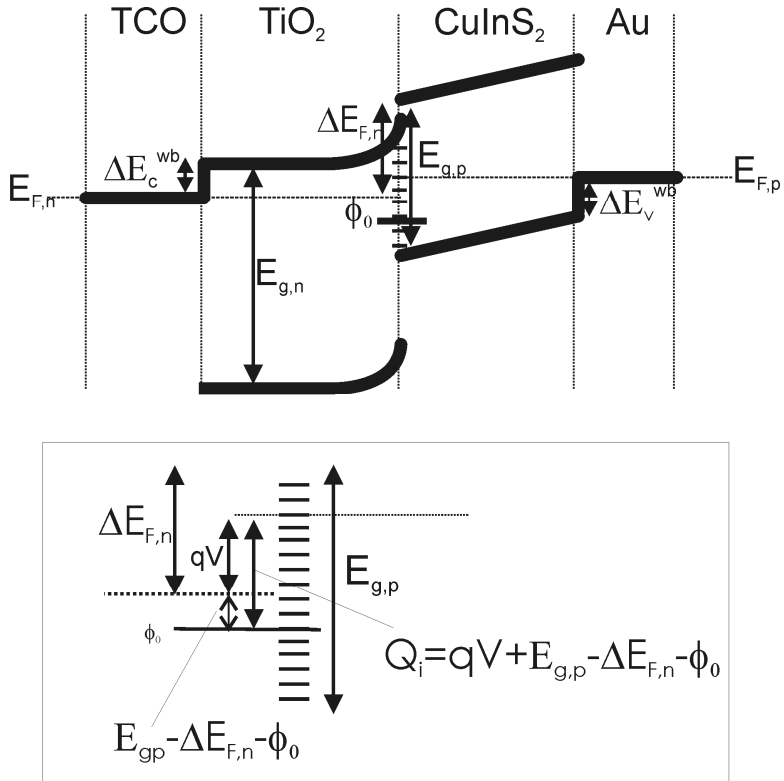


Figure 2.7: Electrostatic model of the $\text{TiO}_2/\text{CuInS}_2$ heterojunction. The potential distribution is governed by the population of the interface states.

2.4.1 Electrostatic model

In the present configuration, the applied voltage V is distributed over the TiO₂ and CuInS₂ films according to

$$V = \phi_n + \phi_p \quad (2.3)$$

in which ϕ_n and ϕ_p are the potential drops over the TiO₂ film and the CuInS₂ film, respectively. In analogy with Rau *et al.*¹⁰⁻¹² a model is elaborated in which interface states determine the distribution of the potential drop over the TiO₂ and the CuInS₂. The model is presented in Figure 2.7.

Following Rau *et al.*, we assume that the interface-state occupation is determined by the Fermi-level in the CuInS₂ and that the interface state density N_i (number of states per area per energy unit) is constant. Four charges are relevant in this model: Q_{Au} , Q_{CIS} , Q_i , and Q_{TiO_2} , which are the charges in the gold back contact, the fully depleted CuInS₂, the interface states, and the TiO₂, respectively. The charge of the interface states, Q_i , shown schematically in the lower part of Figure 2.7, is given by

$$Q_i = qN_i(qV + E_{g,p} - \Delta E_{F,n} - \phi_0) \quad (2.4)$$

in which q is the elementary charge, N_i the interface states density, ϕ_0 the neutrality level of the interface states in eV, $E_{g,p}$ the bandgap of the CuInS₂, V the applied bias and $\Delta E_{F,n}$ the difference between the Fermi-level in the TiO₂ and the conduction band of the CuInS₂, as can be seen in Figure 2.7. Charge neutrality implies

$$Q_{Au} + Q_{CIS} + Q_i + Q_{TiO_2} = 0 \quad (2.5)$$

i.e.,

$$Q_{Au} - qN_a d_p + qN_i(qV + E_{g,p} - \Delta E_{F,n} - \phi_0) + (2q\epsilon_n N_d)^{1/2}(\phi_n - \frac{kT}{q})^{1/2} = 0 \quad (2.6)$$

in which d_p is the thickness of the CuInS₂ layer, ϵ_n the dielectric constant of anatase TiO₂, k Boltzmann's constant, and T the temperature in Kelvin. A closed energy sum can be constructed if one assumes that the Fermi-levels are

flat in the n- and p-type materials. The applied bias relates to a rise in the Fermi-level with qV . Starting at the Fermi-level in the gold contact, first the energy is lowered by the valence band offset ΔE_v^{wb} and the potential drop across the fully-depleted CuInS₂. Next, the energy raises with $E_{g,p}$ to reach the CuInS₂ conduction band. Upon lowering the energy with $\Delta E_{F,n}$ one meets the TiO₂ Fermi-level. Finally, raising the energy with qV the CuInS₂ Fermi-level is reached. This is expressed in the following equations,

$$-\Delta E_v^{wb} - \frac{qN_A d_p^2}{2\epsilon_p} + \frac{Q_{Au} d_p}{\epsilon_p} + E_{g,p} - \Delta E_{F,n} + qV = 0 \quad (2.7)$$

$$-\Delta E_v^{wb} - q\phi_p + E_{g,p} - \Delta E_{F,n} + qV = 0 \quad (2.8)$$

in which ϵ_p is the dielectric constant of CuInS₂. From Eqs.(2.7) and (2.8), the charge on the back contact can be derived according to

$$Q_{Au} = (\Delta E_v^{wb} + \frac{qN_A d_p^2}{2\epsilon_p} - E_{g,p} + \Delta E_{F,n} - qV) \frac{\epsilon_p}{d_p} \quad (2.9)$$

Similar, an expression for $\Delta E_{F,n}$ can be derived from Eq.(2.8), leading to

$$\Delta E_{F,n} = -q\phi_p + qV + E_{g,p} - \Delta E_v^{wb}. \quad (2.10)$$

Upon substitution of Eqs. (2.8) and (2.10) into Eq. (2.6), ϕ_n and ϕ_p can be calculated for every applied bias voltage with the interface states density as parameter. A maximum value for N_i is derived from the capacitance C , which is found with the charge extraction method. From Eqn. (2.4) it follows

$$C = \frac{dQ_i}{dV} = \frac{d[qN_i(qV + E_{g,p} - \Delta E_{F,n} - \phi_0)]}{dV} = \frac{d(q^2VN_i)}{dV} = q^2N_i = 8 \times 10^{-7} \text{ F/cm}^2 \quad (2.11)$$

The interface state density that follows from this formula has the units $\text{J}^{-1}\text{cm}^{-2}$ and one must divide this by q to calculate the interface states per eV. We find an interface states density of $2.5 \times 10^{12} \text{ cm}^{-2}\text{eV}^{-1}$. Figure 2.8 presents the voltage drop over the TiO₂ film as a function of the applied bias V with $N_i = 2.5 \times 10^{12} \text{ cm}^{-2}\text{eV}^{-1}$. Other parameters are: $N_a = 10^{16} \text{ cm}^{-3}$, $N_d = 2 \times 10^{17} \text{ cm}^{-3}$,

$\phi_0 = 0.3$ eV, $d_p = 500$ nm, $E_{g,p} = 1.55$ eV, $\Delta E_v^{wb} = 0.1$ eV, $\epsilon_n = 55$ and $T = 293$ K. Figure 2.8 reveals that the voltage drop over the TiO₂ film has a similar appearance as the ToF plot in Figure 2.6, i.e., for low applied bias voltages the potential drop over the TiO₂ film remains almost constant. This implies that Fermi-level pinning in the TiO₂ is responsible for the ToF behavior of the samples, as will further be discussed below. Moreover, the small voltage drop in the TiO₂ film confirms that the TiO₂ film does not reach full depletion in the ToF experiments.

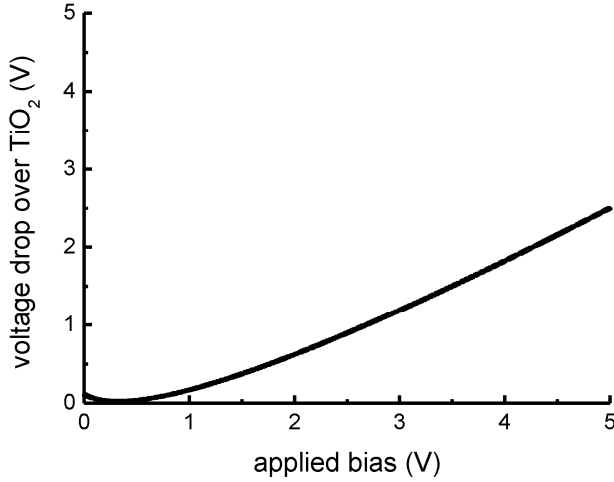


Figure 2.8: Calculated voltage drop over a 300 nm thick TiO₂ film as a function of the applied bias. $N_i = 10^{12}$ cm⁻².

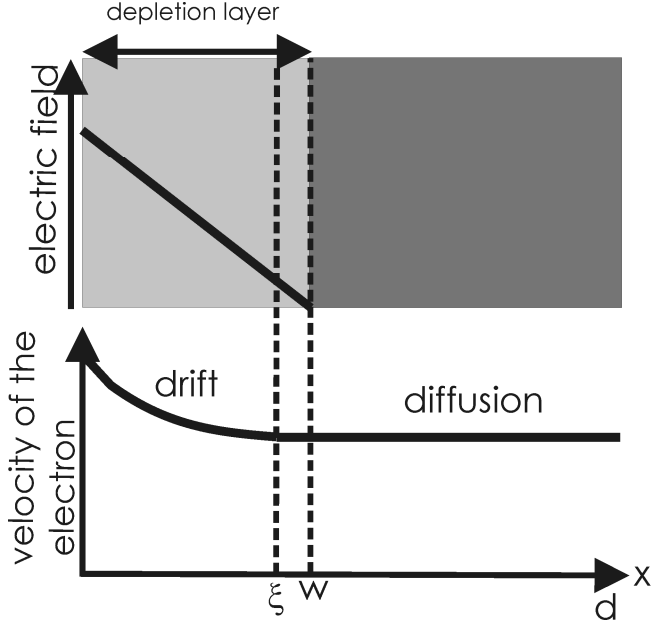


Figure 2.9: Schematical representation of the electric field and electron velocity in the TiO₂. The electric field drops linearly over the depletion region. At ξ , which lies within the depletion region, the velocity becomes diffusion dominated.

2.4.2 Charge transport model

In ToF experiments on TiO₂/CuInS₂ heterojunctions, the voltage drop over the TiO₂ film establishes an electric field, which is a driving force for electron transport. However, as discussed above, TiO₂ does not reach full depletion during the ToF experiment. Following the approach by Emelianova¹⁶ *et al.*, the TiO₂ layer is divided into two regions, a depletion region w , in which the potential drop occurs, and a neutral region $d-w$. The depletion width w of the space-charge region in TiO₂ is given by

$$w = \sqrt{\frac{2\epsilon_n \phi_n}{qN_d}}, \quad (2.12)$$

In the present experiment, the electrons cross the TiO₂ with a velocity

$$v = v_{drift} + v_{diff} , \quad (2.13)$$

in which v_{drift} is the drift velocity and v_{diff} the diffusion velocity. In the depletion layer the electron velocity is dominated by v_{drift} . The electric field, E , in the depletion region is a function of the distance x from the junction and reads

$$E(x) = \frac{qN_d}{\epsilon_n}(w-x) \quad (2.14)$$

As indicated in Figure 2.9 , the electric field drops linearly from $\frac{qN_d w}{\epsilon_n}$ at the surface to zero in the bulk. Accordingly, the drift velocity v_{drift} is given by

$$v_{drift}(x) = \mu E(x) = \frac{\mu q N_d}{\epsilon_n}(w-x) \quad (2.15)$$

and also decreases with x until it equals the diffusion velocity at ξ . At this point, a change from drift-dominated to diffusion-dominated electron transport occurs. In Figure 2.9 the division of TiO₂ in a drift-dominated and a diffusion-dominated region is shown. The point ξ , where diffusion takes over, lies close to the depletion region edge.

The above model can be used to explain the ToF results. The transit time for the drift component is found by integrating Equation (2.15) from $x=0$ to $x=\xi$ (see Figure 2.9) and yields

$$\tau_{drift} = \int_{x=0}^{x=\xi} \frac{\mu q N_d}{\epsilon_n}(w-x) = \frac{\epsilon_n}{\mu q N_d} \ln \left(\frac{w}{w-\xi} \right) \quad (2.16)$$

According to the Einstein equation, the diffusion transit time equals

$$\tau_{diff} = \frac{(d-\xi)^2}{2D} = \frac{(d-\xi)^2 q}{2\mu kT} \quad (2.17)$$

The total transit time τ is the sum of τ_{drift} and τ_{diff}

$$\tau = \frac{1}{\mu} \left[\frac{\varepsilon_n}{qN_d} \ln \left(\frac{w}{w-\xi} \right) + \frac{(d-\xi)^2 q}{2kT} \right]. \quad (2.18)$$

Since w is related to ϕ_n , and ξ is related to w , ϕ_n actually determines the value of τ in Equation (2.18).

2.4.3 Combining the models and fitting the ToF experiments

Equation (2.18), in combination with ϕ_n obtained from the electrostatic model, explains the ToF results very well. The following fit parameters are used: $N_a=10^{16} \text{ cm}^{-3}$, $N_d=2 \times 10^{17} \text{ cm}^{-3}$, $\phi_0=0.3 \text{ eV}$, $d_p=500 \text{ nm}$, $E_{g,p}=1.55 \text{ eV}$, $\Delta E_v^{wb}=0.1 \text{ eV}$, $\varepsilon_n=55$, and $\varepsilon_p=10$. The remaining free parameters are the electron mobility and the interface states density. As a result of the Fermi-level pinning, the voltage drop ϕ_n is almost independent on the applied bias at low applied bias.

Furthermore, because of the low value for ϕ_n , the drift component is much less than the diffusion component in most of the TiO₂ film, i.e. $w \ll d$.

Figure 2.10, Figure 2.11, and Figure 2.12 present the experimental data points and the curves obtained from the model. The agreement is good. From these fits, the electron mobility is found to be $10^{-2} \text{ cm}^2 \text{ V}^{-1} \text{ s}^{-1}$ for all three TiO₂ film thicknesses. Furthermore, the interface states density varies substantially with the TiO₂ film thickness i.e., 5×10^{11} , 2×10^{12} and $6 \times 10^{12} \text{ eV}^{-1} \text{ cm}^{-2}$ for 200, 300 and 400 nm thick TiO₂ films, respectively. Uncertainty in the found values for the mobility and the interface states density has to be considered, since two model parameters (i.e. ϕ_0 and ΔE_v^{wb}) are estimated. Within a range of 0.1-0.5 eV for both parameters, the interface state densities varies ~10% for the 200 nm thick TiO₂ film and 50% for the 400 nm thick TiO₂ film. This variation of the interface state density is of minor importance and does not affect our conclusions. The found values for the mobilities are even less dependent on the ϕ_0 and ΔE_v^{wb} estimates.

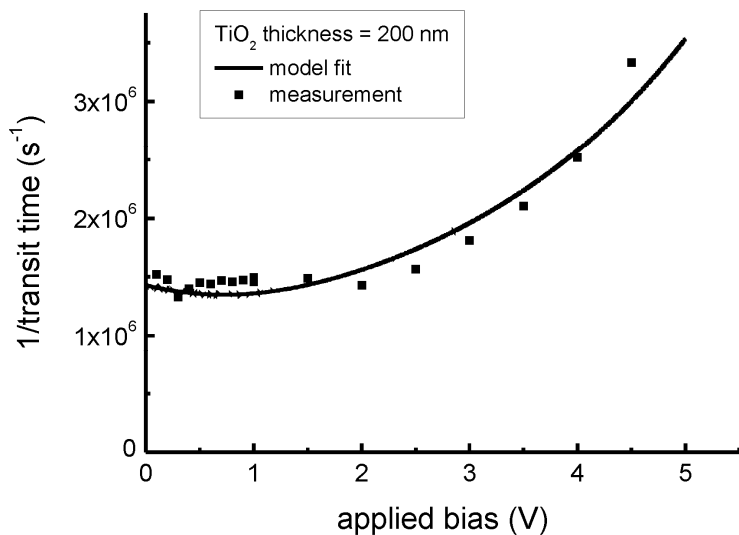


Figure 2.10: Calculated (line) and measured (squares) ToF response for the 200 nm thick TiO₂ film.

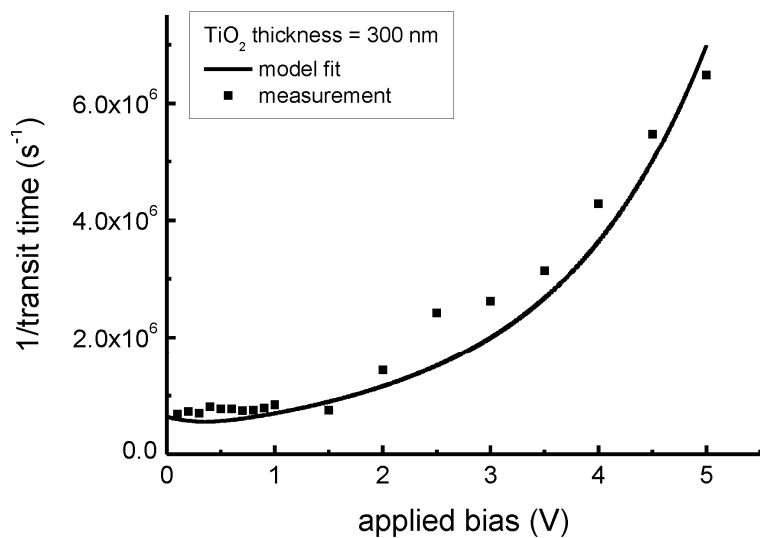


Figure 2.11: Calculated (line) and measured (squares) ToF response for the 300 nm thick TiO₂ film.

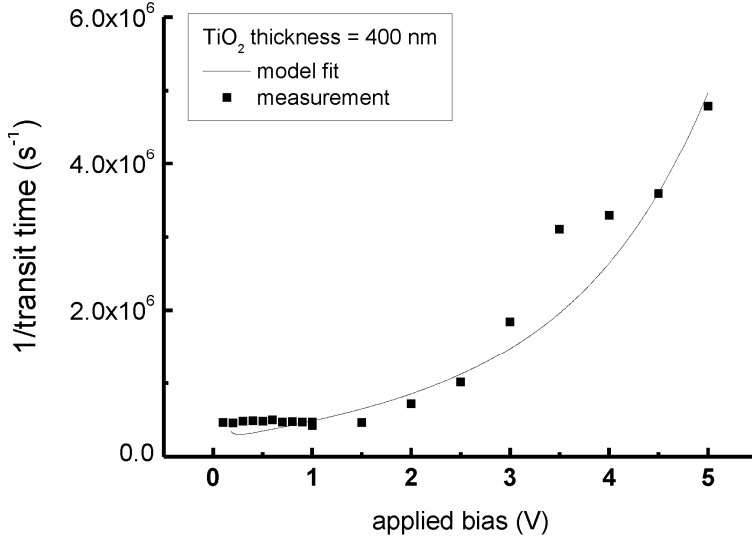


Figure 2.12: Calculated (line) and measured (squares) ToF response for the 400 nm thick TiO₂ film.

Mobility values for electrons in TiO₂ in literature range from beyond 1 cm²/Vs for flat-layer TiO₂ to as small as 10⁻⁷ cm²/Vs for nanoporous TiO₂^{17, 18}. A value of 10⁻² cm²/Vs for the electron mobility in TiO₂ has also been reported by Hendry *et al.*¹⁹ for their nanoporous TiO₂. It is known that the process parameters of spray pyrolysis influence the surface morphology, which ranges from flat to porous²⁰. The mobility found in this work, indicates that the TiO₂ films contain some porosity, which is indeed not unexpected for spray-deposited films.

It is found in this study that an increase of the interface states density with increasing layer thickness occurs. Thicker sprayed TiO₂ films have more surface roughness, leading to a larger interfacial contact area. Accordingly, the concentration of interface states increases, as it had been defined as the number of states per eV per area. The interface states neutrality level is 0.3 eV above the CuInS₂ valance band, irrespective of the TiO₂ film thickness. It is concluded that a rougher surface with a larger contact area results in an increase of interface states, and a stronger pinning of the Fermi level.

2.5 Conclusions

This study successfully performed ToF measurements on TiO₂/CuInS₂ heterojunctions. To allow interpretation of the data, an electrostatic model is introduced in which interface states are dominant and in which CuInS₂ is in full depletion. Furthermore, electron transport in TiO₂ has a drift and a diffusion contribution. With the aid of this model, the ToF data can be explained accurately. The concentration of interface states is found to range between 0.5×10^{12} and 6×10^{12} eV⁻¹cm⁻². The larger surface roughness of thicker TiO₂ films explains this variation well. The neutrality level of these interface states is 0.3 eV above the valence band of CuInS₂. Finally, the electron mobility of TiO₂ is 10^{-2} cm²V⁻¹s⁻¹ irrespective of the film thickness.

Acknowledgements

Advanced Surface Technologies (Bleiswijk, the Netherlands) is acknowledged for supplying the samples. The investigations are financially supported by SenterNovem.

REFERENCES

- [1] F. Lenzmann, M. Nanu, O. Kijatkina and A. Belaidi, "Substantial improvement of the photovoltaic characteristics of TiO₂/CuInS₂ interfaces by the use of recombination barrier coatings", *Thin Solid Films* **2004**, 451-52, 639-643
- [2] M. Nanu, J. Schoonman and A. Goossens, "Solar-energy conversion in TiO₂/CuInS₂ nanocomposites", *Advanced Functional Materials* **2005**, 15, 95-100
- [3] M. Nanu, J. Schoonman and A. Goossens, "Nanocomposite three-dimensional solar cells obtained by chemical spray deposition", *Nano Letters* **2005**, 5, 1716-1719
- [4] M. Krunk, O. Bijakina, V. Mikli, H. Rebane, T. Varema, M. Altosaar and E. Mellikov, "Sprayed CuInS₂ thin films for solar cells: The effect of solution composition and post-deposition treatments", *Solar Energy Materials and Solar Cells* **2001**, 69, 93-98
- [5] M. Krunk, O. Bijakina, T. Varema, V. Mikli and E. Mellikov, "Structural and optical properties of sprayed CuInS₂ films", *Thin Solid Films* **1999**, 338, 125-130
- [6] M. Krunk, O. Kijatkina, H. Rebane, I. Oja, V. Mikli and A. Mere, "Composition of CuInS₂ thin films prepared by spray pyrolysis", *Thin Solid Films* **2002**, 403, 71-75
- [7] M. Krunk, V. Mikli, O. Bijakina, H. Rebane, A. Mere, T. Varema and E. Mellikov, "Composition and structure of CuInS₂ films prepared by spray pyrolysis", *Thin Solid Films* **2000**, 361, 61-64
- [8]
- [9] M. Nanu, J. Schoonman and A. Goossens, "Raman and PL study of defect-ordering in CuInS₂ thin films", *Thin Solid Films* **2004**, 451-52, 193-197
- [10] U. Rau, D. Braunger, R. Herberholz, H. W. Schock, J. F. Guillemoles, L. Kronik and D. Cahen, "Oxygenation and air-annealing effects on the electronic properties of Cu(In,Ga)Se-2 films and devices", *Journal of Applied Physics* **1999**, 86, 497-505
- [11] M. Turcu and U. Rau, "Fermi level pinning at CdS/Cu(In,Ga)(Se,S)₂ interfaces: effect of chalcopyrite alloy composition", *Journal of Physics and Chemistry of Solids* **2003**, 64, 1591-1595
- [12] U. Rau and M. Schmidt, "Electronic properties of ZnO/CdS/Cu(In,Ga)Se-2 solar cells aspects of heterojunction formation", *Thin Solid Films* **2001**, 387, 141-146
- [13] H. Scher and E. W. Montroll, "Anomalous Transit-Time Dispersion in Amorphous Solids", *Physical Review B* **1975**, 12, 2455-2477
- [14] W. E. Spear, "Drift mobility techniques for the study of electrical transport properties in insulating solids", *Journal of Non-Crystalline Solids* **1969**, 1, 197-214
- [15] R. Loeff, J. Schoonman and A. Goossens, "Elucidation of homojunction formation in CuInS₂ with impedance spectroscopy", *Journal of Applied Physics* **2007**, 102, -

- [16] E. V. Emelianova, V. I. Arkhipov and G. J. Adriaenssens, "Time-of-flight measurements in inhomogeneous electric fields", *Journal of Non-Crystalline Solids* **2006**, 352, 1122-1125
- [17] T. Dittrich, "Porous TiO₂: Electron transport and application to dye sensitized injection solar cells", *Physica Status Solidi a-Applied Research* **2000**, 182, 447-455
- [18] B. van der Zanden and A. Goossens, "The nature of electron migration in dye-sensitized nanostructured TiO₂", *Journal of Physical Chemistry B* **2000**, 104, 7171-7178
- [19] E. Hendry, M. Koeberg, B. O'Regan and M. Bonn, "Local field effects on electron transport in nanostructured TiO₂ revealed by terahertz spectroscopy", *Nano Letters* **2006**, 6, 755-759
- [20] A. Duta, "TiO₂ thin layers with controlled morphology for ETA (extremely thin absorber) solar cells", *Thin Solid Films* **2006**, 511, 195-198

Elucidation of the excited-state dynamics in CuInS₂ thin films

Abstract

Transient Absorption (TA) and photoluminescence (PL) spectroscopy have been performed on spray-deposited CuInS₂ thin films. Sulfur and indium vacancies introduce electronic states in the bandgap located at 1.5 and 0.15 eV above the valence band, respectively. Deep donor and deep acceptor doublet states at 1.1 and 0.2 eV are assigned to copper/indium anti-site defects. The excited-state dynamics, which are derived from TA experiments, show electronic coupling between indium anti-site defects and indium vacancies. The Shockley, Read, and Hall recombination model has been modified to account for this coupling and to simulate the TA results. Furthermore, the lifetime of the 1.1 eV state is found to be 20-50 μ s, which is related to the low photovoltage of CuInS₂ based solar cells.

3.1 Introduction

As member of the Cu-chalcopyrite family, CuInS₂ is an excellent candidate as absorber in low-cost solar cells. It has a direct bandgap of 1.55 eV¹, an absorption coefficient² of 10⁵ cm⁻¹ at 500 nm, is chemically stable, has self-healing properties³, and can be made on a large area with simple deposition techniques. As for all Cu-chalcopyrite based solar cells, the actual efficiency is much below the theoretical efficiency. For CuInS₂ an efficiency of 12.5% has been obtained⁴, while the theoretical value is 28.5%⁵. Different cell configurations and preparation methods have been developed in order to maximize the solar cell efficiency and to lower the production costs⁶. A maximum efficiency of 5.5% has been reported for an In₂S₃/CuInS₂ cell made with spray pyrolysis, using a halogen lamp in combination with a water filter⁷. The spray deposited 3D nanocomposite TiO₂/CuInS₂ cell has reached a reproducible efficiency of 5% measured with a solar simulator⁸. Spray pyrolysis is a simple technique open to large-scale production of thin-film solar cells. Previous investigations in our laboratory have shown that the quality of spray deposited Cu-rich p-type CuInS₂ is good enough to produce thin film solar cells^{8,9} with an efficiency of more than 5%. At Advanced Surface Technology, a spin off company of our group, the deposition parameters have been adjusted to obtain a conversion efficiency of 7%. Obviously, the material quality of spray deposited films is still less than that obtained with more advanced deposition techniques and relative high defect concentrations can be expected.

Recombination via defects in the bandgap is a major cause of efficiency loss in solar cells. Shallow defect levels are always present in the bandgap of CuInS₂ and are related to native point defects^{10,11}. For CuInS₂, copper vacancies, indium vacancies and sulfur vacancies are the dominating point defects, but also interstitials and anti-site defects can occur^{12,13}. As for all Cu-chalcopyrite solar cells, the open circuit voltage of CuInS₂ has reached a value of about half of the band gap⁵. Native point defects are not responsible for this limited open cell voltage. Recently, photo-emissions at shorter wavelengths have been found, indicating the presence of deep defect states for which the chemical origin has not been assigned yet¹⁴⁻¹⁸. Rudigier *et al.*¹⁸ show that the presence of a photoluminescence (PL) emission at 1.1 eV is strongly related to the efficiency of a CuInS₂ solar cell. If the PL emission at 1.1 eV is strong, the open-cell voltage is low. Surprisingly, the presence of a 1.1 eV emission does not seem to affect the photocurrent much. They relate the 1.1 eV emission to the density of defect centers but the type of defects that are involved could not be specified.

Krustok *et al.*¹⁴⁻¹⁶ have developed a donor-acceptor pair (DAP) model, in which the presence of deep defect states explains the near infra-red PL bands. In agreement with Onishi *et al.*¹⁷, the DAP model predicts that charge carrier recombination between donor-acceptor pairs at nearest neighbor and next-nearest neighbor positions leads to two PL-bands (D1 and D2) at 0.95 and 0.85 eV, respectively. We will refer to these states as a donor doublet state and an acceptor doublet state. Based on a defect model calculation, Krustok concluded that at least one of the defects involved is an interstitial atom. Onishi *et al.* found PL-emissions at 0.83, 0.99, and 1.24 eV, which show no temperature dependence. They suggest that the deep electronic states originate from a deformation of the crystal structure rather than from a deviation from stoichiometry.

In this paper, we postulate the occurrence of Cu/In anti-site defect association in CuInS₂. At low concentrations, the Cu/In anti-site defects are expected to be present as insulated point defects within the chalcopyrite crystal. An increase of the concentration of Cu/In anti-site defects leads to pair association. At even higher concentrations the defect pairs can cluster and form a new phase, which is known as Cu-Au ordering.

In the present investigations, the defect structure and recombination dynamics of spray pyrolysis deposited CuInS₂ are studied by means of photoluminescence and transient absorption spectroscopy. To the best of our knowledge this is the first transient absorption study on CuInS₂ thin films. We have been able to determine the energy positions of the shallow and deep electronic states in the bandgap of CuInS₂. Furthermore, also the dynamics of filling and emptying of these states could be elucidated.

3.2 Transient absorption

With the transient absorption technique, the change of the absorption of a probe light beam as response to charge carrier generation is measured, as is illustrated in Figure 3.1. In our setup, the sample under investigation is probed with continuous monochromatic light. The transition of interest is selected by the energy of the probe light. At $t=0$, a short laser pulse excites electrons from the valence band into the conduction band. Thermalisation of the electron occurs within the laser pulse duration. The excited electrons either recombine directly or are first trapped in a defect state. The charge carrier occupation of the defect states changes temporarily, which affects the absorption of the probe light. By measuring the change of the transmission of the probe light as a function of time, the lifetime of charges in a defect state can be determined. The change of the absorption is defined as

$$\Delta A(t) = -\frac{I(t) - I_0}{I_0}, \quad (3.1)$$

in which $I(t)$ is the intensity of the transmitted probe light and I_0 the initial transmitted light intensity. The change of the absorption of the probe beam can either be positive (transient absorption) or negative (transient bleaching), as indicated in Figure 3.1.

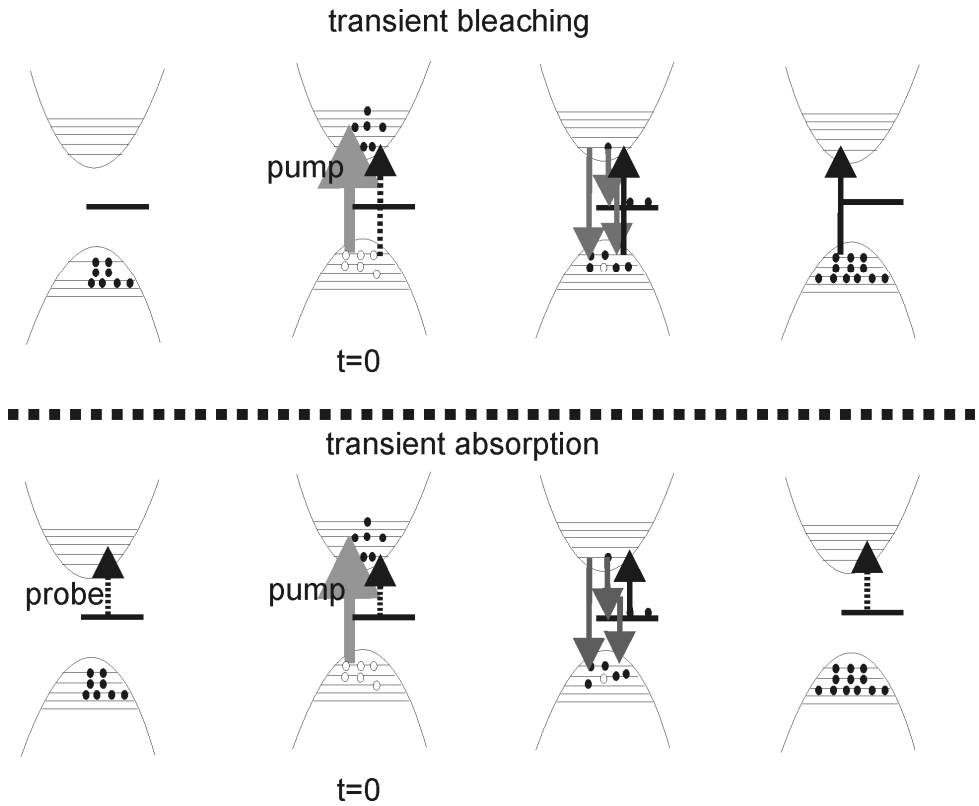


Figure 3.1: schematic representation of the transient absorption method. The upper graph illustrates transient bleaching. The graph below shows transient absorption.

3.3 Experimental aspects

3.3.1 Sample preparation

CuInS₂ samples have been prepared on quartz substrates using spray pyrolysis deposition as is described elsewhere¹⁹⁻²³. Sample production is performed by the company Advanced Surface Technology (AST), Bleiswijk, the Netherlands. An automatic spray robot is used to deposit a thin layer of CuInS₂ onto quartz substrates. The quartz substrates (thickness of 2 mm) are cleaned by successive immersion in acetone and ethanol in an ultrasonic bath. The deposition of CuInS₂ films requires the use of CuCl₂·2 H₂O (98% Aldrich), InCl₃ (98%, Aldrich), and thiourea (98%, Aldrich) solved in demi-water. The composition of the solution is such that Cu-rich material is formed. The best results are obtained if the deposition temperature is rigorously maintained at 300 °C. Small deviation in temperature results in large differences in the optoelectronic properties of CuInS₂. The film thickness is controlled by the number of sprays, which has been varied between 10 and 20. The spray pyrolysis is performed in ambient atmosphere. The film thickness is estimated from optical absorption measurements being about 250 nm.

3.3.2 Photoluminescence spectroscopy

Photoluminescence measurements are performed in the backscatter mode. The sample is mounted in a closed-cycle helium Cryostat (APD Cryogenics CSW-204sl) and cooled to 10 K. Excitation occurs by a Nd:YVO₄ laser, operating at a wavelength of 532 nm (SpectraPhysics Millennia) with 200 mW power. Neutral density filters are used to vary the laser power. The excitation wavelength is removed from the PL signal by a notch filter (Kaiser) and a 620 nm Schott high-pass filter. An optical fiber carries the signal to a monochromator (Acton SpectroPro 2500i). Finally, the spectrum is recorded by a liquid-nitrogen cooled CCD array (Princeton Instruments LN/CCD-1100PB) for the visible range, or a liquid-nitrogen cooled InGaAs detector (Princeton Instruments OMA-V) for the NIR range. PL measurements are integrated over 60 seconds.

3.3.3 Transient Absorption

The transient absorption (TA) setup is schematically presented in Figure 3.2. The probe beam is generated by a halogen lamp (Oriel) and a monochromator (Acton SpectroPro 150) and is focused onto the sample. Behind the sample, another lens is used to direct the beam into a second monochromator (Acton SpectroPro 150), Silicon and InGaAs photodiodes are used as detectors. The electrical signal is amplified (Femto HCA-200M-20K-C) and recorded with an oscilloscope (Tektronix TDS 744). The pulse beam is generated by a Nd-YAG laser (SpectraPhysics QCR) operating at 355 nm and 10 Hz repetition rate, which pumps an optical parametric oscillator (SpectraPhysics MOPO 710) to generate 532 nm pulses with a duration of 5 ns. After passing through several neutral density filters the energy of the pulse is 4 μ J/pulse.

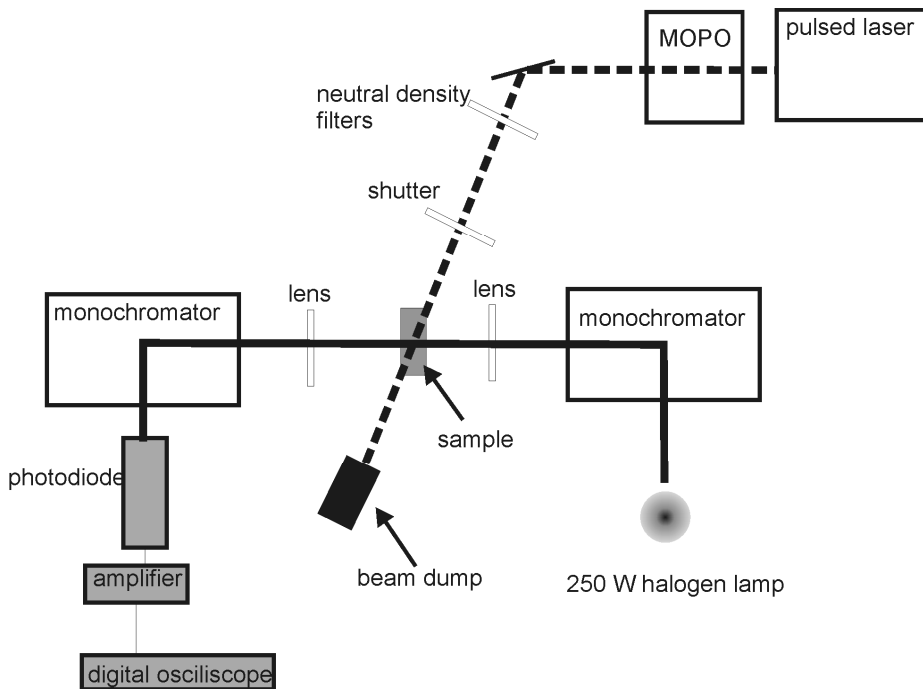


Figure 3.2: Schematical presentation of the TA setup. The probe beam is indicated by a solid line and the pump beam is indicated by a dashed line.

3.4 Results

3.4.1 PL results

Figure 3.3 shows the photoluminescence spectra of CuInS₂ in the visible (Figure 3.3a) and near-infra red (Figure 3.3b) regime at a temperature of 10 K. Several peaks are observed, which are summarized in Table 3.1. The photoluminescence peaks are collected in groups, which have been numbered (1-6) as given in Figure 3.3a, Figure 3.3b, and Table 3.1.

3.4.2 TA results

Transient absorption is performed between 800 and 1700 nm probe wavelengths, corresponding with 1.65-0.85 eV, at a fixed pump wavelength of 532 nm. The transients are fitted with a multiple component exponential decay function with two or three time constants. For each PL-group, one transient will be shown below. The corresponding decay times and the exponential pre-factors are given in Table 3.2.

Table 3.1: PL emissions and their assignments, according to literature.

PL Group	PL energy (eV)	Transition	defect involved	ref.
1	1.520	donor to VB	$V_s^{\bullet\bullet}$ (0.035 eV)	¹⁰
	1.513	bound exciton emission	-	¹⁰
	1.509	bound exciton emission	-	¹⁰
2	1.47/1.46	donor to VB	$In_i^{\bullet\bullet} / In_{Cu}^{\bullet\bullet}$ (0.072 eV)	¹¹
	1.41	CB to $V_{In}^{\bullet\bullet}$	$V_{In}^{\bullet\bullet}$ (0.15 eV)	¹¹
	1.35	$V_s^{\bullet\bullet}$ to $V_{In}^{\bullet\bullet}$	$V_s^{\bullet\bullet}$ and $V_{In}^{\bullet\bullet}$	^{10, 11}
3	1.30	CB to 0.2 eV state	$Cu_{In}^{\bullet\bullet}$	this work
	1.26	CB to 0.25 eV state	$Cu_{In}^{\bullet\bullet}$	this work
4	1.1-1.2	1.1-1.2 eV state to VB	$In_{Cu}^{\bullet\bullet}$	this work
5	0.95	DAP pair - nearest neighbor	-	¹⁴⁻¹⁶
6	0.85	DAP pair - next nearest neighbor	-	¹⁴⁻¹⁶

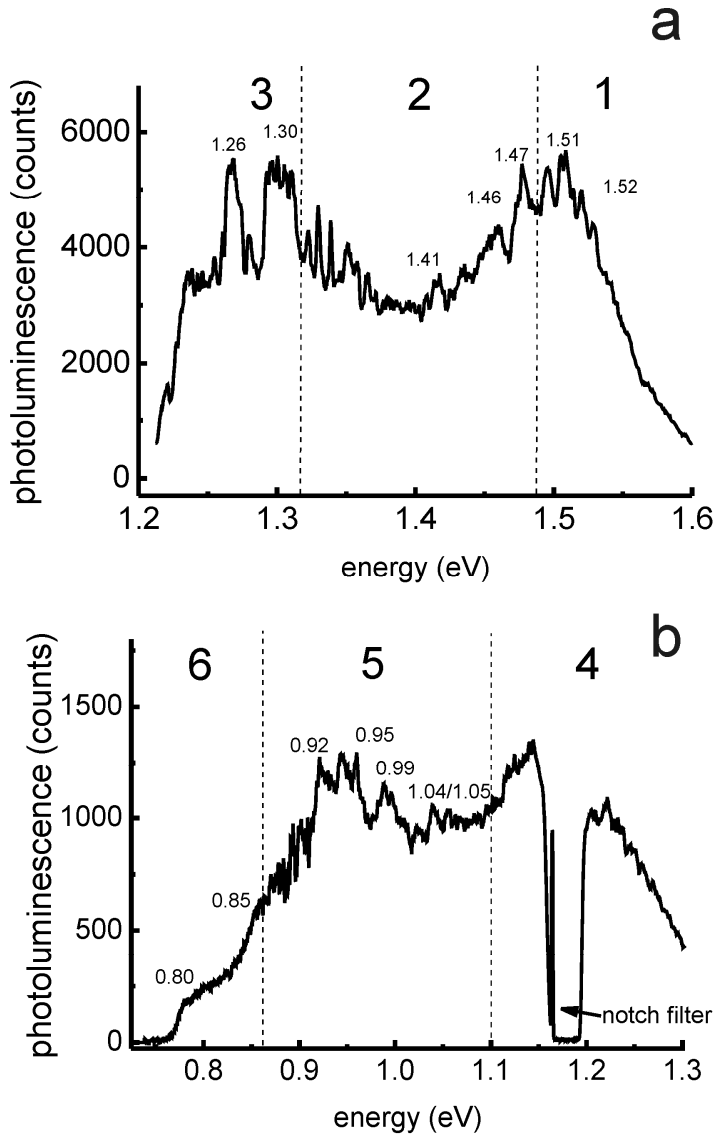


Figure 3.3: (a) Photoluminescence spectrum of CuInS_2 in the visible region, recorded at 10 K. The peaks are collected in three groups, as indicated in the figure. (b) Photoluminescence spectrum of CuInS_2 in the near- infrared region, recorded at 10 K. The peaks are collected in three groups, as indicated in the figure.

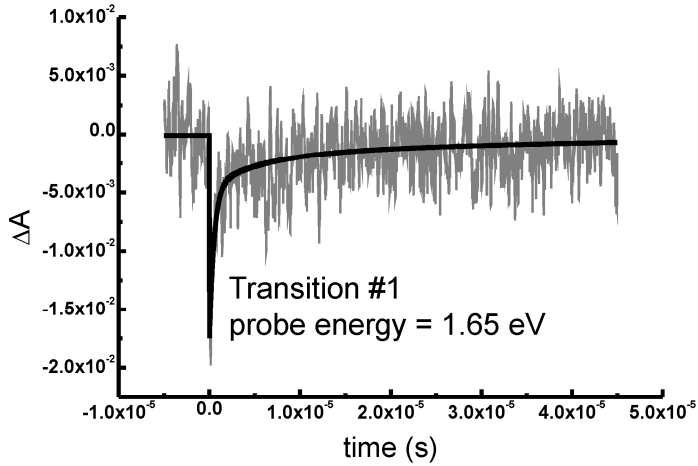


Figure 3.4: Transient Absorption of CuInS₂ for a probe energy of 1.65 eV, corresponding with PL-group #1.

Figure 3.4 shows the transient absorption for a probe energy of 1.65 eV, corresponding with PL-group #1. The curve shows a bleach of the absorption and can be fitted with a three-exponential decay function. The found decay times are 0.5, 5.6, and 40 μ s.

Figure 3.5 shows the transient absorption at a probe energy of 1.38 eV, which corresponds to PL-group #2. First a fast bleach of the absorption occurs, which is followed by a long increase of the absorption. The transients are fitted with a three-exponential decay function. The time constants found are 0.4 μ s for the fast bleach and 3.0 and 30 μ s for the double-exponential absorption decay.

Figure 3.6 shows the transient absorption for a probe energy of 1.3 eV, which belongs to PL-group #3. A fast bleach is followed by slow absorption with two decay times. The found time constants are 0.65 μ s for the fast bleach and 3.8 and 50 μ s for the double-exponential absorption decay.

Figure 3.7 shows the transient absorption for a probe energy of 1.08 eV, which corresponds to PL-group #4. A fast bleach is followed by a slow bleach with a single decay time. The found time constants are 0.22 μ s for the fast bleach and 20 μ s for the slow bleach.

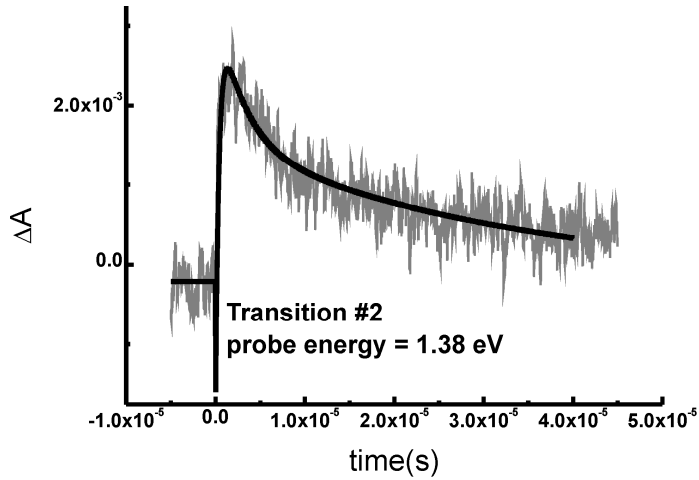


Figure 3.5: Transient Absorption of CuInS₂ for a probe energy of 1.38 eV, corresponding with PL-group #2.

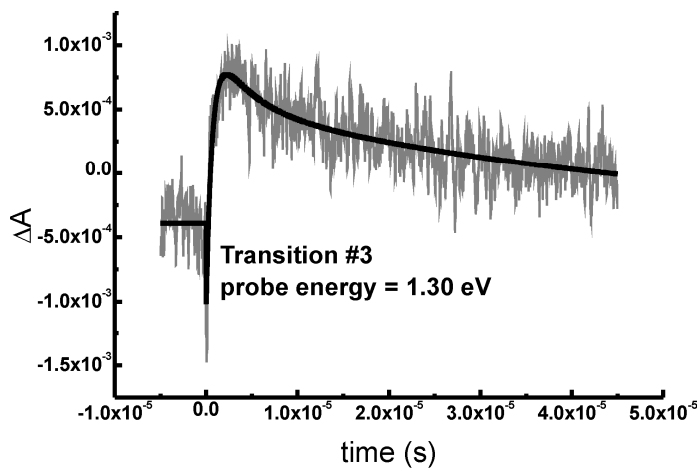


Figure 3.6: Transient Absorption of CuInS₂ for a probe energy of 1.30 eV, corresponding with PL-group #3.

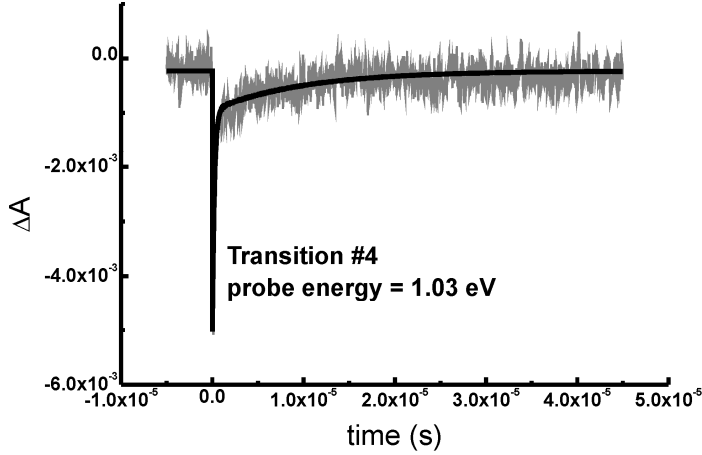


Figure 3.7: Transient Absorption of CuInS₂ for a probe energy of 1.03 eV, corresponding with PL-group #4.

Table 3.2: Transient Absorption results. The pre-factors indicate whether the signal is a bleach (negative pre-factor) or an absorption (positive pre-factor).

PL group #	probe energy (eV)	A1 x10 ⁻³	τ1 (μs)	A2 x10 ⁻³	τ2 (μs)	A3 x10 ⁻³	τ3 (μs)
1	1.65	-13.2	0.51 ± 0.06	-2.66	5.6 ± 2.4	-1.81	40 ± 20
2	1.38	-5.00	0.40 ± 0.05	1.80	3.0 ± 0.1	1.76	30 ± 0.7
3	1.30	-2.2	0.65 ± 0.05	0.6	3.8 ± 0.5	0.94	50 ± 0.5
4	1.08	-3.73	0.22 ± 0.01			-0.32	20 ± 0.5
5	0.95	-3.45	0.36 ± 0.01			-0.85	20 ± 0.5
6	0.86	-2.3	0.50 ± 0.05			-0.84	20 ± 0.2

Figure 3.8 shows the transient absorption for PL-group #5 at a probe energy of 0.95 eV and Figure 3.9 shows the transient absorption for PL-group #6 at a probe energy of 0.86 eV. Both transitions show a bleach of the probe light with a short and a long decay component. The decay times found are 0.36 and 20 μs for the 0.95 eV probe energy and 0.5 μs and 20 μs for the 0.85 eV probe energy.

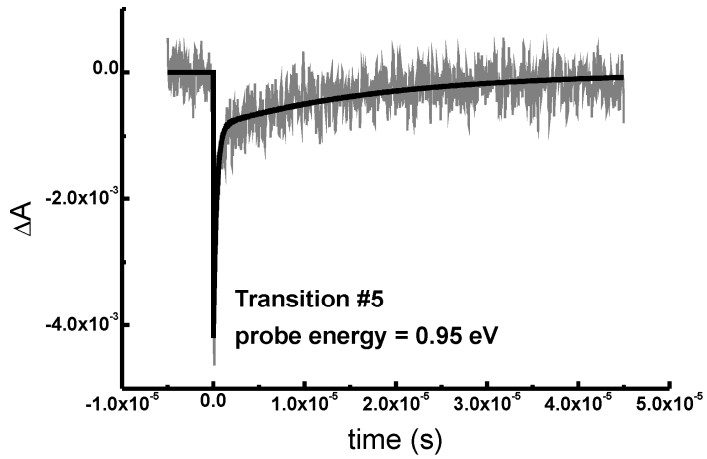


Figure 3.8: Transient Absorption of CuInS₂ for a probe energy of 0.95 eV, corresponding with PL-group #5.

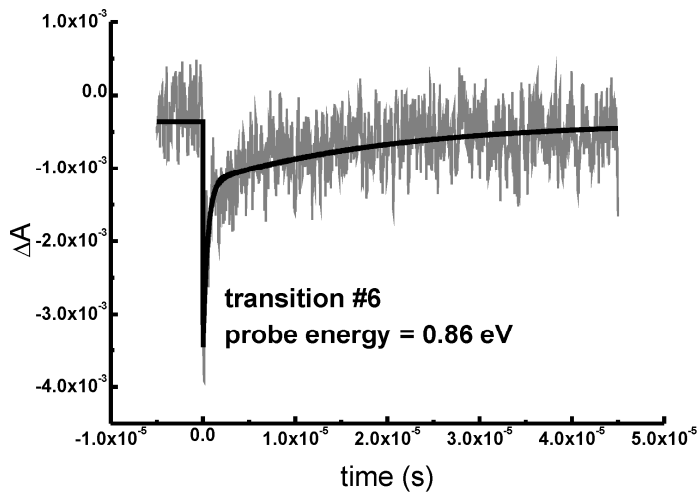


Figure 3.9: Transient Absorption of CuInS₂ for a probe energy of 0.86 eV, corresponding with PL-group #6.

3.5 Discussion

3.5.1 Discussion of the PL data

The spray-deposited CuInS₂ film exists of numerous microscopic sized grains, slightly different in orientation, composition, and size. This causes the dispersion of the PL spectra. Inhomogeneous broadening occurs and only the strongest emission lines emerge from the background. It should be realized that the spectral line width of our set-up as well as the read-out noise of the CCD camera is much less than the observed emission peaks. In the visible region, the band-to-band emission and emission from shallow traps close to the conduction band is found above 1.5 eV (group #1). PL emissions at 1.509, 1.513, and 1.520 eV (see Figure 3.4a) are found, in agreement with the observations of Binsma *et al.*¹⁰. These emissions have been assigned to shallow donor-shallow acceptor transitions^{10, 11}. No emissions are found that can be related to In-rich CuInS₂, from which we conclude that the studied CuInS₂ is Cu-rich (p-type)¹¹. Cu-rich CuInS₂ is known to have indium-vacancies (V_{In}'') at 0.15 eV above the valence band¹³. Additional peaks at 1.41, 1.46, 1.4, and 1.35 eV (group #2) are also observed, which have been assigned to PL transitions from the shallow donor states to the acceptor state at 0.15 eV (V_{In}'')¹¹.

Peaks at 1.3 and 1.26 eV (group #3) indicate transitions from the conduction band and shallow donor states to deep acceptor states at 0.2 and 0.25 eV. In the NIR photoluminescence spectrum, a broad peak at 1.1-1.2 eV (group #4) attracts attention. Unfortunately, second order reflection of the notch-filter in the setup blocks some part of the spectrum, which does not allow us to define the exact peak position. Still, it is clear that an emission occurs between 1.1 and 1.2 eV. This emission cannot be assigned to a transition between known defect levels, but since the emission is very strong, we conclude that a deep defect state is present at 1.1-1.2 eV above the valence band. As will be explained below, a doublet state is present at 1.1 eV above the valence band.

Transitions at 0.95 and 0.85 eV (group #5 and #6) are present, which is in agreement with the observations of Krustok¹⁴⁻¹⁶ and indicate transitions between the DAP doublets. The energy difference between the 0.2 and 0.25 eV acceptor states is in agreement with the acceptor doublet of the DAP model. At 0.95 and 0.85 eV above the 0.2 and 0.25 eV states the donor doublet can be found at 1.15 and 1.1 eV, respectively. It appears that the found state at 1.1-1.2 eV actually is a deep donor doublet. Furthermore, the DAP model predicts discrete energy levels, which explains the sharp PL peaks of group #5. In

agreement with the DAP model, the 0.95 eV emission is related to the nearest neighbor transition (1.15 eV state to 0.2 eV state) and the 0.86 eV emission is related to the next-nearest neighbor transition (1.1 eV state to 0.25 eV state). The final band diagram, extracted from the PL measurements, is shown in Figure 3.10, which includes the doublet states.

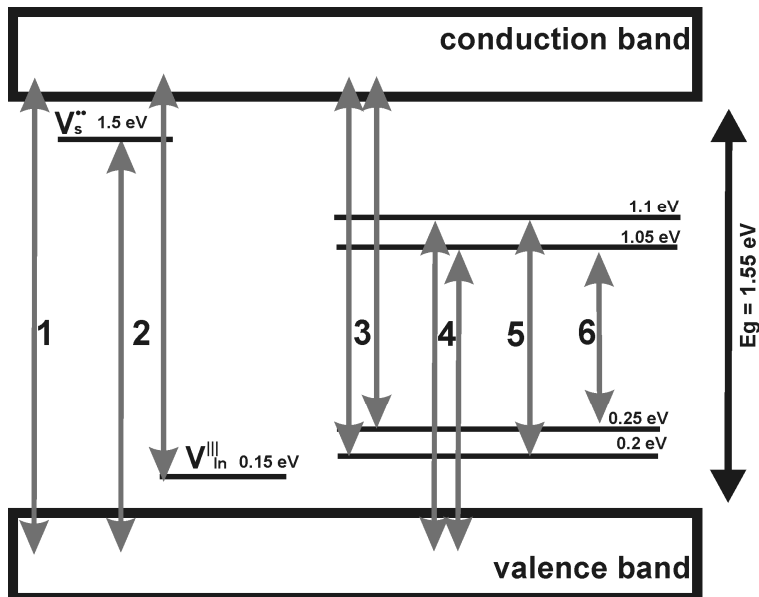


Figure 3.10: Band diagram for CuInS_2 , extracted from the PL spectra at 10K. The numbers corresponds to the PL bands of Figure 3.3. The arrows represent the PL emissions and the TA probe energies.

3.5.2 Discussion of the TA data

Since the optical resolution of the TA measurements is not high enough to discriminate between the deep donor doublet and the deep acceptor doublet these states are considered as two single states at 1.1 eV and at 0.2 eV, respectively. The band diagram of Figure 3.10 is used to discuss the transient absorption response. The transitions in this figure are numbered according to the data in Table 3.2. Transition #1 shows a bleach of the absorption with three decay times. This bleach is caused by an increase in hole-concentration in the valence band, which reduces the band-to-band optical absorption strength. Direct electron-hole recombination has been investigated by Wakita *et al.*²⁴ and has a lifetime in the order of 40-70 ps at a temperature of 10 K, which is much shorter than the time-resolution of our TA setup. Therefore, the decay component of 0.5 μ s can not be assigned to direct recombination. Since the TA measurements have been carried out at room temperature, thermal processes are important. The 0.5 μ s component can be explained by a thermal process, in which trapped electrons in the shallow donor state at 1.5 eV are thermally back-injected into the conduction band. This process increases the electron population of the conduction band, which reduces the band-to-band optical absorption. The existence of two longer decay times shows that some valence band holes live longer and disappear with lifetimes of 2 and 40 μ s.

Transition #2 corresponds to a transition from the 0.15 acceptor state to the conduction band. The signal first shows a fast bleach of the absorption with a decay time that corresponds to the thermally-activated injection from the 1.5 eV state. This bleach is the result of electrons that populate the conduction band, which inhibits the absorption of the probe. An increase in electron population in the acceptor states causes an increase of the absorption. The decay time of this increased absorption relates to the population decay of 0.15 eV state with a component of 4-7 μ s and a component of 50 μ s.

Transition #3 corresponds to the transition from the 0.2 and 0.25 eV states to the conduction band. Similar to Transition #2, first a fast bleach indicates electron-population of the conduction band. The slow absorption represents the population of the 0.2 and 0.25 eV states, which also has two decay times being 4-8 and 50 μ s, respectively. The pre-factor of the slow component of transition #2 is much larger than that of transition #3, which indicates that the slow component of transition #2 is a dominant process.

Transition #4 corresponds to a transition from the valence band to the state at 1.1 eV and shows a transient bleach with two time constants. Similar to Transition #1, a fast bleach occurs because of the increase of the hole concentration in the valence band. The long bleach is the result of filling the 1.1

eV state, which reduces the probe beam absorption. It has a single decay component of 20 μ s.

Finally, Transition #5 and Transition #6 represent the transition between the DAP defects for the nearest neighbor (#5) and the next-nearest neighbor (#6) situation, respectively. As with all other transitions, first a fast bleach occurs. The initial high concentration of holes in the valence band increases the hole capture rate of the 0.2 eV doublet, leading to its fast depopulation. After the fast bleach, when the electron population of the 0.2 eV state increased, a long bleach with a lifetime of 20-30 μ s is present. This bleach is caused by population of the 1.1 eV state which reduces the probe absorption. The multi-component recombination mechanism extracted from the TA measurements is summarized in Figure 3.11. Since both the 0.15 eV state and the 0.2 eV doublet state have an identical decay component, we conclude that electron transfer between the 1.1 eV doublet and both acceptor states occurs, as indicated in Figure 3.11. By introducing this population pathway of both acceptor states the lifetime of these states is coupled to that of the 1.1 eV state, as is experimentally observed.

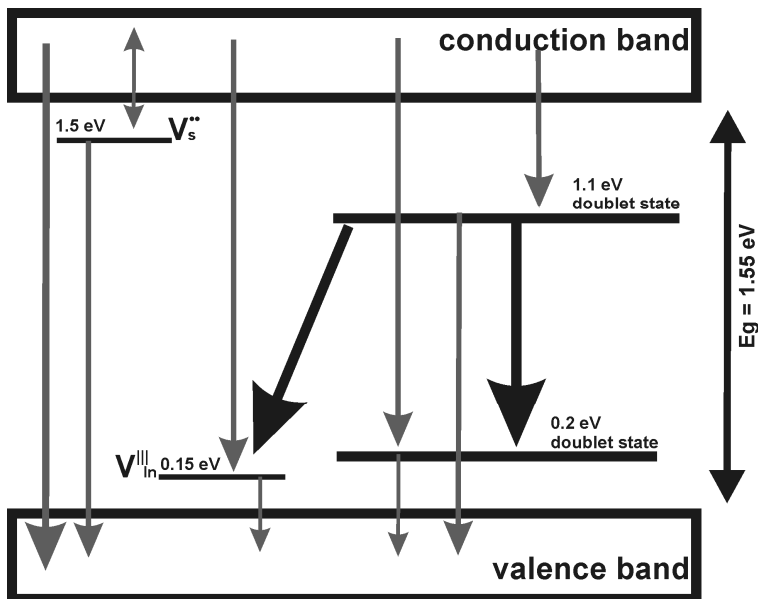


Figure 3.11: Recombination mechanism for CuInS₂, extracted from the transient absorption experiments.

3.5.3 Modeling the recombination mechanism

In order to better understand the kinetics of charging/discharging of the sub-bandgap states, a kinetic model has been elaborated. This model can be used to simulate the TA experiments using the recombination mechanism of Figure 3.11. The well-known Shockley, Read, and Hall mechanism^{25, 26}, referred to as the SRH-model, is generally applied to describe the recombination of excited charge carriers via a single recombination center. Wertheim extended this model by adding multiple recombination centers²⁷. However, coupling between two or more recombination centers is not included in Wertheim's model. Therefore, we extended his model and included the electronic coupling between deep donors and -acceptors. Our model consists of multiple coupled differential equations, which can be solved analytically only under certain restrictions²⁸, but can be solved with numerical methods. In this way, we calculated the occupation of the recombination centers as a function of time.

The model

Following Wertheim, the recombination mechanism for a non-degenerate semiconductor can be described in terms of the capture rates for electrons and holes, U_{ni} and U_{pi} , respectively, in which index ni denotes electron capture from the conduction band to state i and pi hole capture from the valence band to state i . All the symbols are explained in Table 3.3.

$$U_{ni} = \alpha_{ni} \left[N_i^0 \delta n - (n_0 + n_{i1} + \delta n) \delta N_i \right] \quad (3.2)$$

$$U_{pi} = \alpha_{pi} \left[N_i^- \delta p + (p_0 + p_{i1} + \delta p) \delta N_i \right] \quad (3.3)$$

The rate of recombination by direct processes, U_d , without the involvement of a recombination center, is

$$U_d = \alpha_d (n_0 \delta p + p_0 \delta n + \delta n \delta p) \quad (3.4)$$

The Wertheim-model is extended to include state-to-state recombination. First, we define the capture rate for an electron from state k to state i , U_{ki} , in which $E_k > E_i$

$$U_{ki} = \alpha_{ki} (N_k^- + \delta N_k) (N_i^0 - \delta N_i) - \varepsilon_{ik} (N_i^- + \delta N_i) (N_k^0 - \delta N_k) \quad (3.5)$$

In equilibrium, $\delta N_k=0$, $\delta N_i=0$, and $U_{ki}=0$ leading to

$$\mathcal{E}_{ik} = \alpha_{ki} \frac{N_k^- N_i^0}{N_i^- N_k^0} \quad (3.6)$$

Fermi-Dirac statistics is applied for the deep states N_k^- , N_k^0 , N_i^- , and N_i^0 , i.e.,

$$N_k^- = \frac{N_k}{1 + e^{\frac{E_k - E_F}{kT}}} \quad (3.7)$$

$$N_k^0 = \frac{N_k}{1 + e^{\frac{E_F - E_k}{kT}}} \quad (3.8)$$

$$N_i^- = \frac{N_i}{1 + e^{\frac{E_i - E_F}{kT}}} \quad (3.9)$$

$$N_i^0 = \frac{N_i}{1 + e^{\frac{E_F - E_i}{kT}}} \quad (3.10)$$

Upon substituting of Eqns. (3.7), (3.8), (3.9), and (3.10) into Eqn. (3.6) we find

$$\mathcal{E}_{ik} = \alpha_{ki} e^{\frac{E_i - E_k}{kT}} \quad (3.11)$$

Substitution of Eqn.(3.11) into Eqn.(3.5), yields

$$U_{ki} = \alpha_{ki} \left[(N_i^0 - \delta N_i)(N_k^- + \delta N_k) - e^{\frac{E_i - E_k}{kT}} (N_k^0 - \delta N_k)(N_i^- + \delta N_i) \right] \quad (3.12)$$

In this way the deviation from equilibrium of the charge carriers in the bands and the recombination centers, denoted as δn , δp and δN_i , are found via

$$\frac{d\delta n}{dt} = g - U_d - \Sigma U_{ni} \quad (3.13)$$

$$\frac{d\delta p}{dt} = g - U_d - \Sigma U_{pi} \quad (3.14)$$

$$\frac{d\delta N_i}{dt} = U_{ni} - U_{pi} + \sum_i^{E_k > E_i} U_{ki} - \sum_i^{E_k < E_i} U_{ik} \quad (3.15)$$

Obviously, the electro-neutrality condition must be fulfilled at all times

$$\sum_i \delta N_i + \delta n = \delta p \quad (3.16)$$

To solve the set of differential equations (Eqns. (3.13)-(3.16)), the initial conditions have to be known. We define $t=0$ as the moment that the laser pulse has excited the charge carriers over the bandgap. To obtain the initial conditions,

$$\delta n(0) = \delta p(0) \quad (3.17)$$

and

$$\delta N_i(0) = 0 \quad (3.18)$$

The model parameters are the capture cross sections, α_i , which determine the probability that an electron or a hole is being captured by state i .

Table 3.3: symbols used in the extended SRH-Wertheim model

α_{ni}	product of electron-capture cross section and thermal velocity of electrons for state i
α_{pi}	as above, but for holes for state i
α_{ki}	as above, but for the transition from state k to state i , with $E_k > E_i$
ε_{ik}	as above, but for the transition from state i to state k , with $E_k > E_i$
N_i^0	density of empty recombination center i (from the electron point of view)
N_i^-	density of filled recombination center i
δN_i	deviation from the thermal equilibrium occupancy of a set of recombination centers
n_0, p_0	thermal equilibrium carrier concentration
n_{1i}, p_{1i}	carrier concentration with the Fermi-level at the energy level of the trap for state i
$\delta n, \delta p$	deviations from the thermal-equilibrium carrier concentrations
g	rate of external generation of carriers

3.5.4 Simulation results

The model described above has been used to simulate the experimental data following the proposed mechanism of Figure 3.11 and the results are presented in Figure 3.12 and Table 3.4. The capture cross sections found are in good agreement with values found for Cu(In,Ga)Se₂ materials^{29, 30}, which vary from 10^{-21} to 10^{-23} cm⁻². The deviation of the equilibrium carrier concentration for the bands and the states as a function of time is shown in Figure 3.12. To reveal the exponential decay processes, a single logarithmic graph is used. First of all, from Figure 3.12a, it is evident that immediately after the laser pulse the hole concentration is larger than the electron concentration, showing that electrons are being trapped. The initial process shown in this Figure involves the population of the conduction band which is coupled to the depopulation of the 1.5 eV state. In addition, Figure 3.12b shows the filling of the deep defect states with a similar rate. The 1.5 eV state is emptied after ~ 10 μ s, but the other states stay populated a much longer time. It can be seen in Figure 3.12b that the electron occupation decay of the 0.15 and the 0.2 eV doublet state has two decay times. For the 1.1 eV doublet state the numerical simulation reveals a

single decay component, in agreement with the TA response. Clearly, there is an excellent correspondence between this recombination model and the TA experimental findings. Disabling the state-to-state recombination in the model (not shown), restores the original Wertheim-model, i.e. a single decay-time for all defect states. This contradicts our findings. State-to-state recombination explains the experimentally found multi-component recombination mechanism. In a future paper we shall elaborate on how state-to-state recombination affects the photoluminescence yield.

Table 3.4: parameters used for simulating the TA experiments

defect state #	1	2	3	4	5	6
energy level (eV)	0.15	0.2	0.25	1.05	1.1	1.5
Density of States (cm ⁻³)	10 ¹⁴	10 ¹⁴	10 ¹⁴	10 ¹⁶	10 ¹⁶	10 ¹⁴
electron capture cross section (cm ²)	10 ⁻¹⁹	10 ⁻¹⁹	10 ⁻¹⁹	10 ⁻²¹	10 ⁻²¹	10 ⁻¹⁷
hole capture cross section (cm ²)	1.4x10 ⁻²⁰	2.4x10 ⁻²⁰	2.5x10 ⁻²⁰	2x10 ⁻²¹	2x10 ⁻²¹	1x10 ⁻²¹
electron state-to-state cross sections (cm ²)						
<i>state 5 to 1</i>	10 ⁻¹⁹					
<i>state 5 to 2</i>	10 ⁻¹⁹					
<i>state 4 to 3</i>	10 ⁻¹⁹					
direct recombination α_d	2x10 ⁻¹⁸					

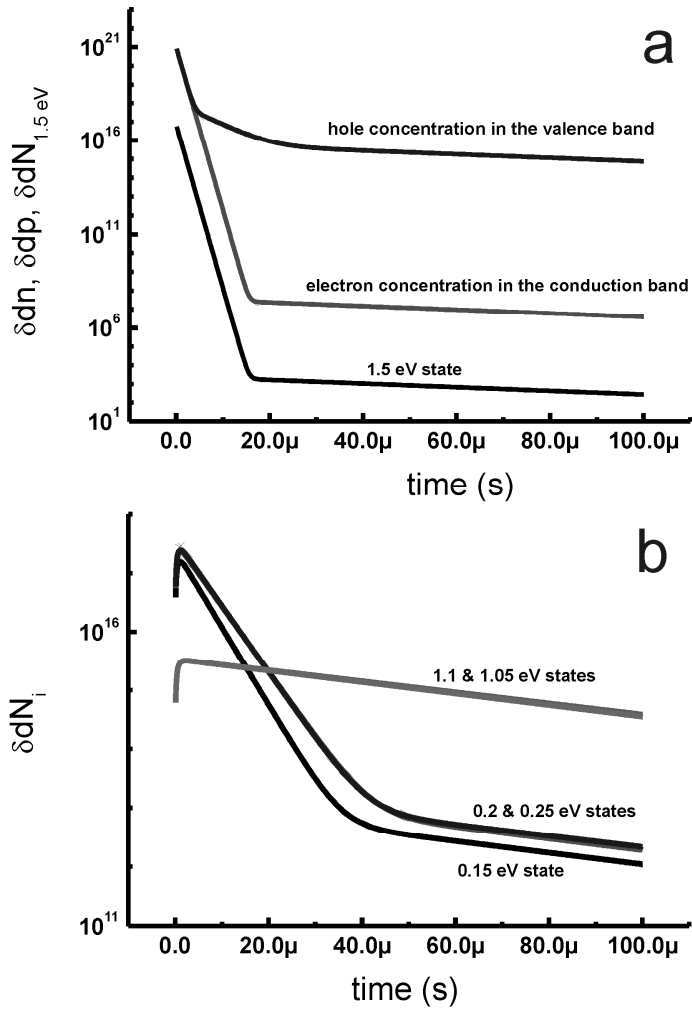


Figure 3.12: Numerical simulation of the excited state dynamics. The used model parameters are given in Table 3.4.

3.5.5 Cu/In anti-site defects

We have determined the energy positions of the deep doublets from the DAP model and related the emission at 1.1-1.2 eV to the DAP defect. Raman scattering shows a peak at 295 cm⁻¹, confirming the presence of the chalcopyrite structure in our material^{31,32}. The FWHM of this peak is 12 cm⁻¹. Rudigier *et al.* related the Raman peak-width to the intensity of the 1.1 eV PL emission, which is a measure for defect concentration. The 1.1 eV PL emission found for our samples confirms the presence of a large concentration of defects that can be responsible for the broad Raman-peak.

We postulate that the deep donor – deep acceptor pair is related to the presence of associated copper/indium anti-site defects in CuInS₂, i.e. Cu_{In}" and In_{Cu}". A Cu/In anti-site defect that is present in a chalcopyrite matrix is described as the interchange of copper- and indium atoms. In Kröger-Vink notation, Cu/In anti-site defects are a combination of the following defects: In_{Cu}•, In_{Cu}", Cu_{In}' and Cu_{In}". Zhang *et al.*³³ have calculated the energy levels of these four defect states for CuInSe₂, which is closely related to CuInS₂. The calculated values are 0.29 and 0.58 eV from the valence band for Cu_{In}' and Cu_{In}", respectively and 0.25 and 0.34 eV from the conduction band for In_{Cu}• and In_{Cu}", respectively. Although these values are based on computational approximations for CuInSe₂, they correspond to the observed deep defect levels that we and others, i.e., Krustok, Onishi, and Rudigier, find. In the calculations of Zhang, it is assumed that the defect is always at the exact lattice position, which does not need to be the case since defects may polarize the material.

We postulate that the 1.1 eV donor doublet and the 0.2 eV acceptor doublet originate from In_{Cu}" and Cu_{In}" defects, respectively. Since the defect levels are deep, the charge of the defects is expected to be at least 2 times the elementary charge, in analogy with the calculations of Zhang and Wei. Additionally, the 1.05 eV and 0.25 eV defect levels are the next-nearest neighbor In_{Cu}" and Cu_{In}" defects, in agreement with the DAP model. Cu/In anti-site defect association explains the electronic coupling between the 1.1 and 0.2 eV defect states that is responsible for the DAP-transitions found by Krustok, which is confirmed by the transient absorption experiments of this work. Krustok *et al.* have suggested that one of the two DAP defects most likely involves an interstitial position. Indeed it seems possible that the Cu_{In}" defect occupies an off-center lattice position. Therefore, we postulate that the DAP defects are related to the presence of Cu/In anti-site defects. Further investigations are in progress to clarify this hypothesis.

Although the energy of the anti-site defect is neutral, the mechanism of its formation has not yet been reported. With both photoluminescence and transient absorption we found electronic coupling between the electronic states at 1.1 and 0.15 eV. This electronic coupling between the anti-site defects and the $V_{\text{In}}^{\text{'''}}$ strongly suggests a mechanism of anti-site defect formation. Below, we propose a mechanism in which $V_{\text{In}}^{\text{'''}}$ initiates the formation of anti-site defects. As has been pointed out above, $V_{\text{In}}^{\text{'''}}$ are present in p-type Cu-rich CuInS₂. The first step of the mechanism is the occupation of the $V_{\text{In}}^{\text{'''}}$ by a copper ion



Next, the indium ion jumps to the vacant copper position, leaving a $V_{\text{In}}^{\text{'''}}$ behind,



Accordingly anti-site defects are preferably formed near indium vacancies, leading to a $(V_{\text{In}}^{\text{'''}} - \text{In}_{\text{Cu}}^{\text{''}} - \text{Cu}_{\text{In}}^{\text{'}})^{\text{'''}}$ defect association. This explains the observed electronic coupling between the 0.15 eV $V_{\text{In}}^{\text{'''}}$ and the 1.1 eV $\text{In}_{\text{Cu}}^{\text{''}}$ defects.

3.5.6 Effect on solar cell properties

Rudigier *et al.* have related the PL emission at 1.1 eV to the solar cell efficiency¹⁸. They found a correlation between the intensity of the 1.1 eV PL peak and the photovoltage that is generated by a solar cell. The PL emission at 1.1 eV shows that the $\text{In}_{\text{Cu}}^{\text{''}}$ is present in the sample. The measured TA lifetime of 20-50 μs for the 1.1 eV doublet state explains the observations of Rudigier. A defect state in the bandgap, with such a long lifetime, is able to store charge by which the quasi Fermi-level of electrons and, therefore, the solar cell voltage output, i.e., the difference between the electron and hole quasi Fermi-levels at the electrodes, is affected. However, because of its long lifetime, this defect level does not act as a recombination center and, therefore, has little effect on the photocurrent yield. To our best knowledge we are the first reporting the lifetime of the defect state at 1.1 eV in the bandgap of CuInS₂. Others have reported the relation between this defect state and the solar cell performance¹⁸. Further research is in progress to elucidate the effect of the 1.1 eV defect state on electron capture rate in order to clarify the performance of CuInS₂ solar cells.

3.6 Conclusions

This study successfully elaborated the excited state dynamics of spray deposited CuInS₂ thin films. A kinetic model has been developed, which supports state-to-state electron recombination and explains the experimental observations. Deep donor and deep acceptor doublet states at 1.1 eV and 0.2 eV have been assigned to the associated anti-site defects $\text{In}_{\text{Cu}}^{\bullet\bullet}$ and $\text{Cu}_{\text{In}}^{\bullet}$, respectively. The 1.1 eV doublet state shows an electron lifetime of 20-50 μs . This state is electronically coupled to the 0.15 eV state, which indicate that $\text{V}_{\text{In}}^{\bullet}$ associates to $\text{In}_{\text{Cu}}^{\bullet\bullet}$. The long electron lifetime of the $\text{In}_{\text{Cu}}^{\bullet\bullet}$ defect explains the low photovoltage that is generally observed in CuInS₂ based solar cells.

Acknowledgements

Advanced Surface Technologies (Bleiswijk, the Netherlands) is acknowledged for supplying the samples. The investigations are financially supported by SenterNovem.

REFERENCES

- [1] R. Klenk, U. Blieske, V. Dieterle, K. Ellmer, S. Fiechter, I. Hengel, A. JagerWaldau, T. Kampschulte, C. Kaufmann, J. Klaer, M. C. LuxSteiner, D. Braunger, D. Hariskos, M. Ruckh and H. W. Schock, "Properties of CuInS₂ thin films grown by a two-step process without H₂S", *Solar Energy Materials and Solar Cells* **1997**, 49, 349-356
- [2] M. Kanzari and B. Rezig, "Effect of deposition temperature on the optical and structural properties of as-deposited CuInS₂ films", *Semiconductor Science and Technology* **2000**, 15, 335-340
- [3] J. F. Guillemoles, U. Rau, L. Kronik, H. W. Schock and D. Cahen, "Cu(In,Ga)Se-2 solar cells: Device stability based on chemical flexibility", *Advanced Materials* **1999**, 11, 957-+
- [4] J. Klaer, J. Bruns, R. Henninger, K. Seimer, R. Klenk, K. Ellmer and D. Braunig, "Efficient CuInS₂ thin-film solar cells prepared by a sequential process", *Semiconductor Science and Technology* **1998**, 13, 1456-1458
- [5] S. Siebentritt, "Wide gap chalcopyrites: material properties and solar cells", *Thin Solid Films* **2002**, 403, 1-8
- [6] M. Kemell, M. Ritala and M. Leskela, "Thin film deposition methods for CuInSe(2) solar cells", *Critical Reviews in Solid State and Materials Sciences* **2005**, 30, 1-31
- [7] T. T. John, C. S. Kartha, K. P. Vijayakumar, T. Abe and Y. Kashiwaba, "Modification in cell structure for better performance of spray pyrolysed CuInS₂/In₂S₃ thin film solar cell", *Applied Physics a-Materials Science & Processing* **2006**, 82, 703-707
- [8] M. Nanu, J. Schoonman and A. Goossens, "Nanocomposite three-dimensional solar cells obtained by chemical spray deposition", *Nano Letters* **2005**, 5, 1716-1719
- [9] R. O'Hayre, M. Nanu, J. Schoonman, A. Goossens, Q. Wang and M. Gratzel, "The influence of TiO₂ particle size in TiO₂/CuInS₂ nanocomposite solar cells", *Advanced Functional Materials* **2006**, 16, 1566-1576
- [10] J. J. M. Binsma, L. J. Giling and J. Bloem, "Luminescence of CuInS₂ .2. Exciton and near Edge Emission", *Journal of Luminescence* **1982**, 27, 55-72
- [11] H. Y. Ueng and H. L. Hwang, "The Defect Structure of CuInS₂ .1. Intrinsic Defects", *Journal of Physics and Chemistry of Solids* **1989**, 50, 1297-1305
- [12] D. Perniu, S. Vouwzee, A. Duta and J. Schoonman, "Defect chemistry of solar cell chalcopyrite materials", *Journal of Optoelectronics and Advanced Materials* **2007**, 9, 1568-1571
- [13] J. J. M. Binsma, L. J. Giling and J. Bloem, "Luminescence of CuInS₂ .1. The Broad-Band Emission and Its Dependence on the Defect Chemistry", *Journal of Luminescence* **1982**, 27, 35-53
- [14] J. Krustok, J. Raudoja and H. Collan, "Photoluminescence and the tetragonal distortion in CuInS₂", *Thin Solid Films* **2001**, 387, 195-197

- [15] J. Krustok, J. Raudoja, J. H. Schon, M. Yakushev and H. Collan, "The role of deep donor-deep acceptor complexes in CIS-related compounds", *Thin Solid Films* **2000**, 361, 406-410
- [16] J. Krustok, J. H. Schon, H. Collan, M. Yakushev, J. Madasson and E. Bucher, "Origin of the deep center photoluminescence in CuGaSe₂ and CuInS₂ crystals", *Journal of Applied Physics* **1999**, 86, 364-369
- [17] T. Onishi, K. Abe, Y. Miyoshi, K. Wakita, N. Sato and K. Mochizuki, "Study of deep photoluminescence levels in CuInS₂ crystals", *Journal of Physics and Chemistry of Solids* **2005**, 66, 1947-1949
- [18] E. Rudigier, T. Enzenhofer and R. Scheer, "Determination of the quality of CuInS₂-based solar cells combining Raman and photoluminescence spectroscopy", *Thin Solid Films* **2005**, 480, 327-331
- [19] M. Krunks, O. Bijakina, V. Mikli, H. Rebane, T. Varema, M. Altosaar and E. Mellikov, "Sprayed CuInS₂ thin films for solar cells: The effect of solution composition and post-deposition treatments", *Solar Energy Materials and Solar Cells* **2001**, 69, 93-98
- [20] M. Krunks, O. Bijakina, T. Varema, V. Mikli and E. Mellikov, "Structural and optical properties of sprayed CuInS₂ films", *Thin Solid Films* **1999**, 338, 125-130
- [21] M. Krunks, O. Kijatkina, H. Rebane, I. Oja, V. Mikli and A. Mere, "Composition of CuInS₂ thin films prepared by spray pyrolysis", *Thin Solid Films* **2002**, 403, 71-75
- [22] M. Krunks, V. Mikli, O. Bijakina, H. Rebane, A. Mere, T. Varema and E. Mellikov, "Composition and structure of CuInS₂ films prepared by spray pyrolysis", *Thin Solid Films* **2000**, 361, 61-64
- [23] I. Oja, M. Nanu, A. Katerski, M. Krunks, A. Mere, J. Raudoja and A. Goossens, "Crystal quality studies of CuInS₂ films prepared by spray pyrolysis", *Thin Solid Films* **2005**, 480, 82-86
- [24] K. Wakita, K. Nishi, Y. Ohta and N. Nakayama, "Time-resolved photoluminescence studies of free excitons in CuInS₂ crystals", *Applied Physics Letters* **2002**, 80, 3316-3318
- [25] R. N. Hall, "Electron-Hole Recombination in Germanium", *Physical Review* **1952**, 87, 387-387
- [26] W. Shockley and W. T. Read, "Statistics of the Recombinations of Holes and Electrons", *Physical Review* **1952**, 87, 835-842
- [27] G. K. Wertheim, "Transient Recombination of Excess Carriers in Semiconductors", *Physical Review* **1958**, 109, 1086-1091
- [28] D. Debuf, "General theory of carrier lifetime in semiconductors with multiple localized states", *Journal of Applied Physics* **2004**, 96, 6454-6469
- [29] J. A. M. AbuShama, S. W. Johnston, R. S. Crandall and R. Noufi, "Meyer-Neldel rule and the influence of entropy on capture cross-section determination in Cu(In,Ga)Se₂", *Applied Physics Letters* **2005**, 87, -
- [30] D. L. Young and R. S. Crandall, "An electrostatic barrier to trap filling in CuIn_{1-x}Ga_xSe₂", *Applied Physics Letters* **2003**, 83, 2363-2365

- [31] J. Alvarez-Garcia, J. Marcos-Ruzafa, A. Perez-Rodriguez, A. Romano-Rodriguez, J. R. Morante and R. Scheer, "MicroRaman scattering from polycrystalline CuInS₂ films: structural analysis", *Thin Solid Films* **2000**, 361, 208-212
- [32] J. Alvarez-Garcia, A. Perez-Rodriguez, A. Romano-Rodriguez, J. R. Morante, L. Calvo-Barrio, R. Scheer and R. Klenk, "Microstructure and secondary phases in coevaporated CuInS₂ films: Dependence on growth temperature and chemical composition", *Journal of Vacuum Science & Technology a-Vacuum Surfaces and Films* **2001**, 19, 232-239
- [33] S. B. Zhang, S. H. Wei, A. Zunger and H. Katayama-Yoshida, "Defect physics of the CuInSe₂ chalcopyrite semiconductor", *Physical Review B* **1998**, 57, 9642-9656

How multiple decay paths affect the photoluminescence intensity in CuInS₂

Abstract

The influence of the excitation power on the photoluminescence (PL) intensity of spray-deposited CuInS₂ has been studied. Above a certain threshold power, the PL intensity decreases when the excitation power increases, which is a new phenomenon for these materials. The recombination model that we developed earlier to explain the transient absorption behavior of CuInS₂ is modified to simulate the power dependent PL measurements. The model includes state-to-state recombination pathways. It is found that saturation of deep defect states at 1.1 eV inhibits the recombination from the conduction band to defect states at 0.15 and 0.2 eV, when state-to-state coupling is enabled.

4.1 Introduction

Fundamental understanding of recombination processes of excited charge carriers in semiconductors is of paramount importance for optoelectronic devices. Photoluminescence (PL) spectroscopy is a widely used tool for the investigation of recombination in semiconductors. From photoluminescence spectroscopy, bandgaps can be determined along with the relative energetic position of sub-bandgap defect states. Sub-bandgap PL emission is related to electron-hole recombination mediated by a defect state. As will be shown in this paper the (sub-bandgap) PL intensity as a function of the excitation power contains valuable information about the recombination mechanism¹. Phenomenological studies have shown that the PL emission intensity I and the excitation power L often follows a power law², i.e.,

$$I \sim L^k \quad (4.1)$$

It is found that for band-to-band recombination $1 < k < 2$, while for band-to-state and donor-acceptor pair transitions $k < 1$ holds.

Three types of electron-hole recombination can be distinguished. The first one (Type I) involves a single defect state in the bandgap, along with band-to-band recombination. This recombination type is described by the well-known Shockley, Read, and Hall (SRH) mechanism^{3,4}, in which band-to-band recombination and recombination via a single defect state is considered. Using the SRH model, the lifetime of a charge carrier in a defect state can be calculated.

The second type of recombination mechanism (Type II), which is modeled by Wertheim⁵, has multiple defect states in the bandgap. This model is an extension of the SRH model and describes band-to-band recombination as well as recombination via multiple defect states. In Wertheim's model, the defect states do not have interactions with each other.

A more complicated situation occurs when, besides band-to-band and multiple band-to-state recombination, also state-to-state recombination is present. This is the third type of recombination mechanism (Type III). This type III recombination model is developed by Schmidt *et al.*². In order to explain the deviations from the power law of Eq.(4.1) Schmidt *et al.* elaborated on the intensity-dependence of near-band-edge PL, using a set of rate equations for band-to-band, band-to-state, state-to-band, and state-to-state recombination, respectively. Numerical solutions obtained by Schmidt *et al.* are in agreement

with experimental findings, in which different types of transitions are involved. They also report that k -values (see Eq.(4.1)) for different recombination pathways which occur simultaneously are related. Rega *et al.*⁶ have studied the temperature and excitation power dependence of the PL in Cu(In,Ga)Se₂ thin films. Their experiments show a relation between the k -values for band-to-band and defect-related emissions, in analogy with the model of Schmidt *et al.*

In the present paper, the PL of CuInS₂ thin films is investigated as a function of excitation power. To explain the observations, our previously developed recombination model, which is of Type III, is applied. This model can be applied to any defect structure and recombination mechanism, including that of Types I and II. It is an extension of the model of Schmidt *et al.*, which only considers a single donor-acceptor pair. In the present model, an unlimited number of donor-acceptor pairs can be included. Furthermore, Schmidt *et al.* assume that the electron concentration in the conduction band equals the hole concentration in the valence band, thus neglecting the charge that is temporarily stored in the defect states. As will be shown in this paper, the charge carrier population in the defect states is of paramount importance when state-to-state coupling is present.

4.2 Experimental aspects

CuInS₂ samples have been prepared on quartz substrates using spray pyrolysis deposition as is described elsewhere⁷⁻¹¹. The quartz substrates (thickness of 2 mm) are cleaned by successive immersion in acetone and ethanol in an ultrasonic bath. The deposition of CuInS₂ films requires the use of CuCl₂·2 H₂O (99.99% Aldrich), InCl₃ (98%, Aldrich), and thiourea (98%, Aldrich) solved in demi-water. The best results are obtained if the deposition temperature is rigorously maintained at 300 °C. Small deviation in temperature results in large differences in the CuInS₂ opto-electronic properties. The thickness is controlled by the number of sprays, which has been varied between 10 and 20. Spray pyrolysis is performed in ambient atmosphere.

Photoluminescence measurements are performed in the backscatter mode. The sample is mounted in a closed-cycle helium cryostat (APD Cryogenics CSW-204sl) and cooled to 10 K. Excitation occurs by a Nd:YVO₄ laser, operating at a wavelength of 532 nm (SpectraPhysics Millennia) with a power range of 200 mW to 5 W. Neutral-density filters are used to vary the laser power below 200 mW. The excitation wavelength is removed from the PL signal by a 620 nm Schott high-pass filter. An optical fiber carries the signal to a monochromator (Acton SpectroPro 2500i). Finally, the spectrum is recorded by a CCD array (Princeton Instruments PIXIS-100). PL measurements are integrated over 60 seconds.

4.3 Results

Figure 4.1 shows the PL spectra for thin films of CuInS₂ at 10K for excitation intensities of 0.02, 0.2, 2, 20, and 50 mW. The PL spectra are fitted by multiple Gaussian functions. Emissions are observed at 1.28, 1.37, and 1.54 eV. Figure 4.2 shows the PL intensity, as derived from the Gaussian fits, as a function of excitation power. The emissions at 1.28, 1.37, and 1.54 eV increase strongly with increasing excitation power for values below 5 mW. However, when the excitation power rises above 5 mW, the PL intensity of the 1.28 and 1.37 eV emissions decrease and saturates at a low level. The emission at 1.54 eV behaves differently. After the initial increase, the PL intensity stabilizes at the maximum value obtained at 5 mW. The PL spectra are not dependent on the excitation history; the same PL behavior is found upon increasing or decreasing the excitation power.

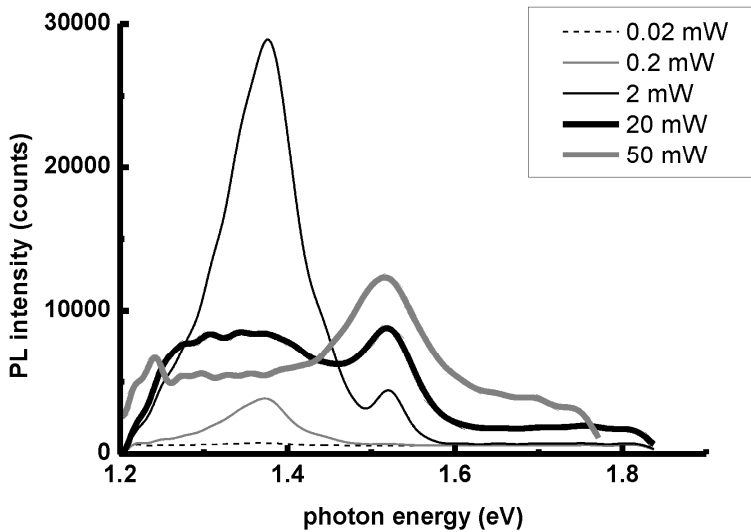


Figure 4.1: PL emissions of CuInS₂ for excitation powers of 0.02, 0.2, 2, 20, and 50 mW.

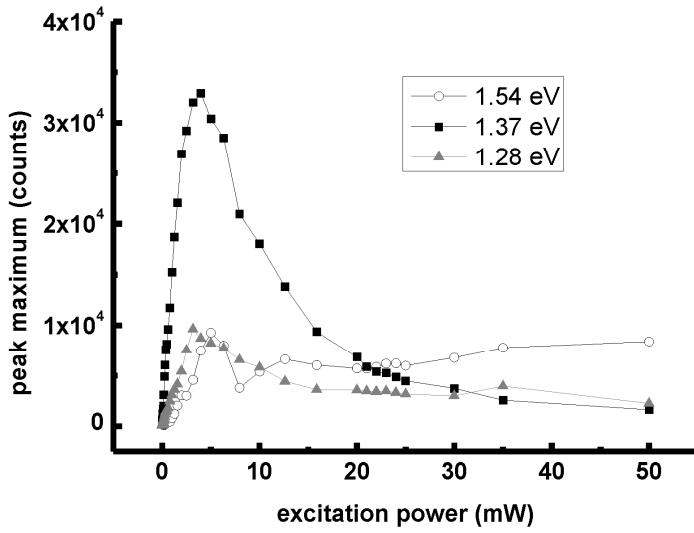


Figure 4.2: PL intensity as a function of excitation power for the emissions at 1.37, 1.28, and 1.54 eV. The intensity is derived from the peak-maximum of the Gaussian fit of the PL emissions.

4.4 Discussion

The PL spectrum of CuInS₂ shows three emissions, which have been assigned in a previous paper¹². The emission at 1.54 eV originates from band-to-band and/or shallow defects recombination. Recombination from the conduction band to the $V_{In}^{\prime\prime}$ state at 0.15 eV yields an emission at 1.37 eV. Recombination from the conduction band and shallow donor states to the acceptor doublet state at 0.2 eV yields an emission at 1.28 eV. Nearest-neighbor and next-nearest neighbor interactions split the energy level of the doublet state in two levels, at 0.2 and 0.25 eV, respectively.

The observed decrease of the PL intensities of the 1.37 and 1.28 eV emissions above a threshold excitation power is not predicted by the recombination models of Types I and II. The reason for this remarkable behavior is that for CuInS₂ more than one recombination pathway is present for certain defect states, as we concluded from PL and TA experiments in our previous investigations¹². Associated defects at nearest-neighbor and next-nearest neighbor lattice positions enable state-to-state recombination, in addition to band-to-state and state-to-band recombination. The recombination pathways for CuInS₂, derived from TA spectroscopy, are presented in Figure 4.3. For the 0.15 eV state and the 0.2 eV doublet state, two population paths are present, and for the 1.1 eV state three depopulation pathways exist. With this model, the recombination dynamics of CuInS₂ can be explained accurately. In this paper, the same model is applied to study the excitation power dependent PL of CuInS₂.

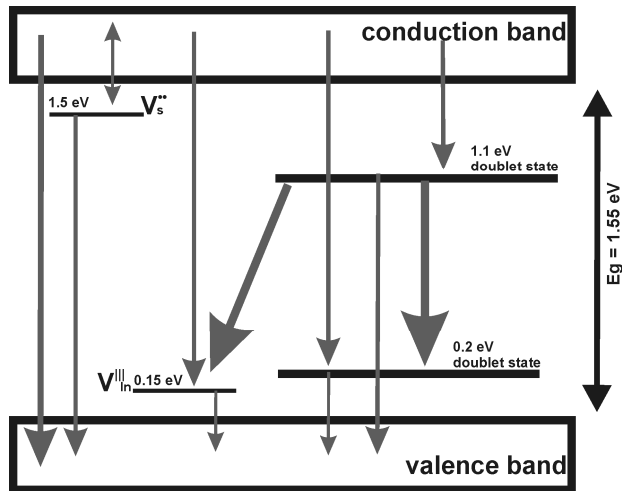


Figure 4.3: recombination diagram for CuInS₂, derived from PL and transient absorption measurements¹²

4.4.1 The recombination model

Following Wertheim⁵, the recombination dynamics for a non-degenerate semiconductor can be described in terms of the capture rates for electrons and holes, U_{ni} and U_{pi} , respectively, in which index ni denotes electron capture from the conduction band to state i and pi the hole capture from the valence band to state i . All the symbols are explained in Table 4.1. For band-to-state and state-to-band recombination, the following expressions hold.

$$U_{ni} = \alpha_{ni} \left[N_i^0 \delta n - (n_0 + n_{1i} + \delta n) \delta N_i \right] \quad (4.2)$$

$$U_{pi} = \alpha_{pi} \left[N_i^- \delta p + (p_0 + p_{1i} + \delta p) \delta N_i \right] \quad (4.3)$$

The band-to-band (geminate) recombination rate is given by

$$U_d = \alpha_d (n_0 \delta p + p_0 \delta n + \delta n \delta p) \quad (4.4)$$

State-to-state recombination, in which index ki denotes electron transfer from state k to state i , is given by

$$U_{ki} = \alpha_{ki} \left[(N_i^0 - \delta N_i)(N_k^- + \delta N_k) - e^{-\frac{E_i - E_k}{kT}} (N_k^0 - \delta N_k)(N_i^- + \delta N_i) \right] \quad (4.5)$$

The derivation of this expression can be found in our previous publication¹².

The deviation from equilibrium of the charge carriers in the bands and the states, denoted as δn , δp , and δN_i , can be derived from

$$\frac{d\delta n}{dt} = g - U_d - \Sigma U_{ni} \quad (4.6)$$

$$\frac{d\delta p}{dt} = g - U_d - \Sigma U_{pi} \quad (4.7)$$

$$\frac{d\delta N_i}{dt} = U_{ni} - U_{pi} + \sum_i^{E_k > E_i} U_{ki} - \sum_i^{E_k < E_i} U_{ik} \quad (4.8)$$

Table 4.1: Symbols used in the present recombination model

α_{ni}	product of electron-capture cross section and thermal velocity of electrons for state i
α_{pi}	as above, but for holes for state i
α_{ki}	as above, but for the transition from state k to state i , with $E_k > E_i$
ε_{ik}	as above, but for the transition from state i to state k , with $E_k > E_i$
N_i^0	density of empty states i (from the electron point of view)
N_i^-	density of filled states i
δN_i	deviation from the thermal equilibrium occupancy of state i
n_0, p_0	thermal equilibrium carrier concentration
n_{i0}, p_{i0}	carrier concentration with the Fermi-level at the energy level of the trap for state i
$\delta n, \delta p$	deviations from the thermal-equilibrium electron and hole concentrations
g	rate of external generation of carriers

Obviously, the electro-neutrality condition must be fulfilled at all times.

$$\sum_i \delta N_i + \delta n = \delta p. \quad (4.9)$$

The two summations in Eq. (4.8) represent the extension of Wertheim's model. Eqns. (4.6)-(4.9) form a set of differential equations that describes the charge carrier population as a function of time.

4.4.2 Simulating power dependent PL experiments

In PL experiments, a continuous excitation source is used to excite charge carriers beyond the bandgap energy, which is represented by the parameter g in Eqns. (4.6) and (4.7). The PL intensity is related to the rates U_{ni} , U_{pi} , and U_{ki} . We assume that a constant fraction of the decay is radiative. For instance, the PL intensity from the conduction band to State 1 is given by U_{n1} and the PL intensity from State 3 to the valence band is U_{3p} . To simulate steady-state PL experiments, integration of Eqns. (4.6) and (4.7) must continue until stable solutions for the carrier concentrations are found.

To explain the outcome of the present model, first a simplified recombination scheme, involving three defect states, is elaborated. In Figure 4.4, the recombination pathways that are included are indicated by arrows. States 1

and 2 are acceptor states at 0.1 eV above the valence band. State 1 is coupled to State 3 at 1.1 eV above the valence band, while State 2 is not. Therefore, for States 1 and 3 multiple recombination paths are present. For State 1, multiple population pathways exist, and for State 3 multiple depopulation paths are present. The corresponding time-dependent recombination model, i.e., Eqns. (4.6)-(4.9), is numerically solved at 10 K and the capture rates are extracted for the steady-state situation. The model parameters are shown in Table 4.2 and the results of the simulation are shown in Figure 4.5 - Figure 4.8.

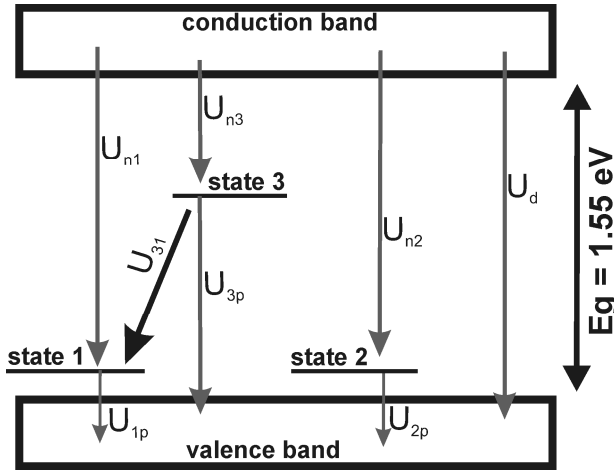


Figure 4.4: Simplified recombination diagram for demonstrating the state-to-state coupling recombination model.

Table 4.2: Parameters used for simulating the model presented in Figure 4.4. These parameters are estimations based on literature data.

defect state #	1	2	3
energy level (eV)	0.1	0.1	1.1
Density of States (cm ⁻³)	10 ¹⁴	10 ¹⁴	10 ¹⁶
electron capture cross section (cm ²)	10 ⁻¹⁹	10 ⁻¹⁹	10 ⁻²¹
hole capture cross section (cm ²)	1x10 ⁻²⁰	1x10 ⁻²⁰	2x10 ⁻²¹
<i>electron state-to-state cross sections (cm²)</i>			
state 3 to 1	10 ⁻¹³		
direct recombination α_d	1x10 ⁻¹⁹		

Figure 4.5 shows the calculated deviation from the thermal equilibrium occupation as a function of time for the electrons and holes in the conduction- and valence bands (δn and δp), and for the 3 defect states (δN_1 , δN_2 , and δN_3). It can be seen that steady state is reached long before $t=1$ ms. The influence of the excitation power g on the occupation of States 1, 2, and 3 are shown in Figs. Figure 4.6, Figure 4.7, and Figure 4.8, respectively. In these figures, the normalized deviation from the defect-state equilibrium occupation, $\delta N_i/N_i$ (a), the recombination rate from the defect state to/from the bands (b), and, if present, the state-to-state recombination rate (c) are shown. In all cases, 1 ms is chosen as the reference time to ascertain that a steady state has established.

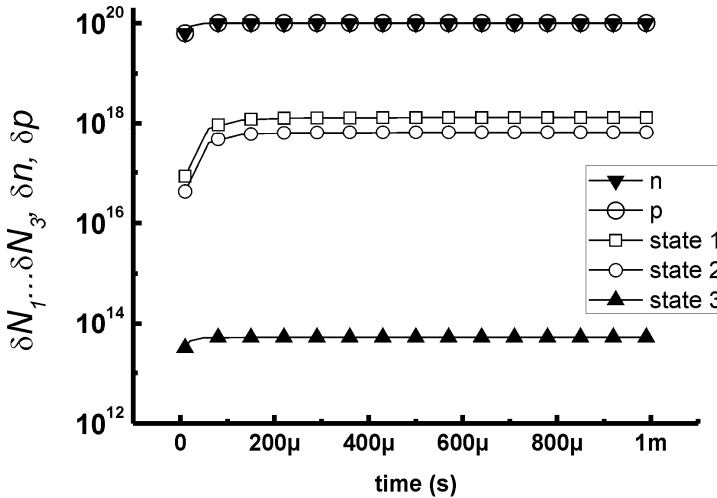


Figure 4.5: Results of the recombination model as a function of time for $g=10^{25}$ $\text{m}^{-3}\text{s}^{-1}$. δN_i for States 1, 2, and 3, and the electron concentration in the conduction band and the hole concentration in the valence band are shown. It can be seen that the concentrations reach a steady state long before 1 ms.

Figure 4.6a shows the normalized deviation from the equilibrium occupation of State 2, $\delta N_2/N_2$, which starts to increase at $g=10^{25} \text{ m}^{-3}\text{s}^{-1}$. From $g=10^{27} \text{ m}^{-3}\text{s}^{-1}$, $\delta N_2/N_2$ increases slower with g until it settles at a value of 0.5 for $\delta N_2/N_2$. Figure 4.6b shows that U_{n2} follows the $I \sim L^k$ law, and the k -factor changes at $g=10^{27} \text{ m}^{-3}\text{s}^{-1}$ from 1.0 to 0.2. Since a steady state for the population of State 2 has established at $t=1 \text{ ms}$, $U_{n2}=U_{2p}$. It should be noted that the k -factor changes at the same excitation power where $\delta N_2/N_2$ starts to increase slower with g . Here, we define the threshold excitation power g_{th} , as is indicated in Figure 4.6. The correspondence between the change in k -factor, the change in $\delta N_2/N_2$, and g_{th} will be discussed below.

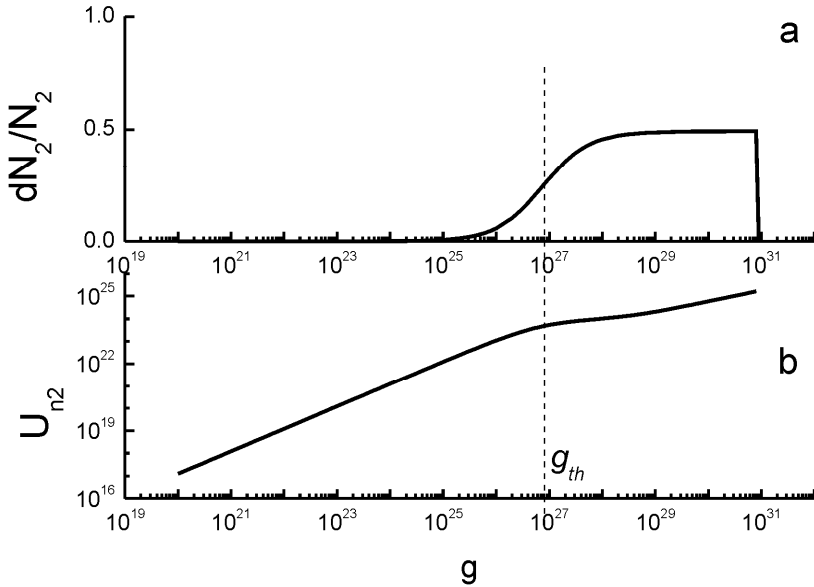


Figure 4.6: Results for the recombination model at $t=1 \text{ ms}$ for State 2, according to the recombination mechanism in Figure 4.4. In (a) $\delta N_2/N_2$ is shown. Graph (b) shows the electron capture rate, which equals the hole capture rate.

Figure 4.7 shows that the calculated behavior of State 1 differs from that of State 2. The normalized deviation from the equilibrium occupation $\delta N_1/N_1$ starts to increase at $g=10^{25} \text{ m}^{-3}\text{s}^{-1}$, but it increases much faster than is found for State 2. Again, $\delta N_1/N_1$ saturates at $\delta N_1/N_1=0.5$, but now this already occurs at the threshold excitation power g_{th} . Figure 4.7b shows that the capture rate U_{n3} starts to become smaller just before g_{th} . In Figure 4.7c can be seen that the capture rate U_{31} shows a change in the slope at g_{th} . Finally, it is also clear that U_{n1} does not equal U_{1p} , which is due to the multiple population pathways of State 1.

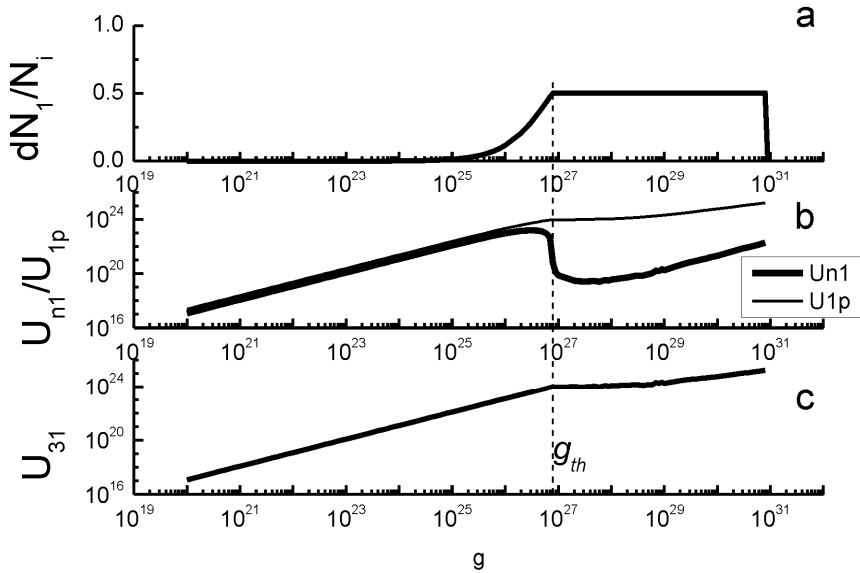


Figure 4.7: Results of the simulations at $t=1 \text{ ms}$ for State 1, according to the recombination mechanism in Figure 4.4. In part (a) $\delta N_1/N_1$ is shown, part (b) shows the electron-and hole capture rates, and part (c) shows the capture rate from State 3 to State 1.

Figure 4.8 shows the calculated behavior for State 3. The normalized deviation from the equilibrium occupation, $\delta N_3/N_3$, shown in Figure 4.8a, starts to increase at $g=10^{27} \text{ m}^{-3}\text{s}^{-1}$ and is much larger than for State 1 and State 2. Again, it settles at a value of 0.5 for $\delta N_3/N_3$. In Figure 4.8b can be seen that U_{3p} does not equal U_{n3} , which is caused by the multiple depopulation states that are present for State 3. At g_{th} , the capture rate U_{3p} starts to increase until it equals U_{n3} . Figure 4.8c is similar to Figure 4.7c and illustrates the behavior of U_{31} .

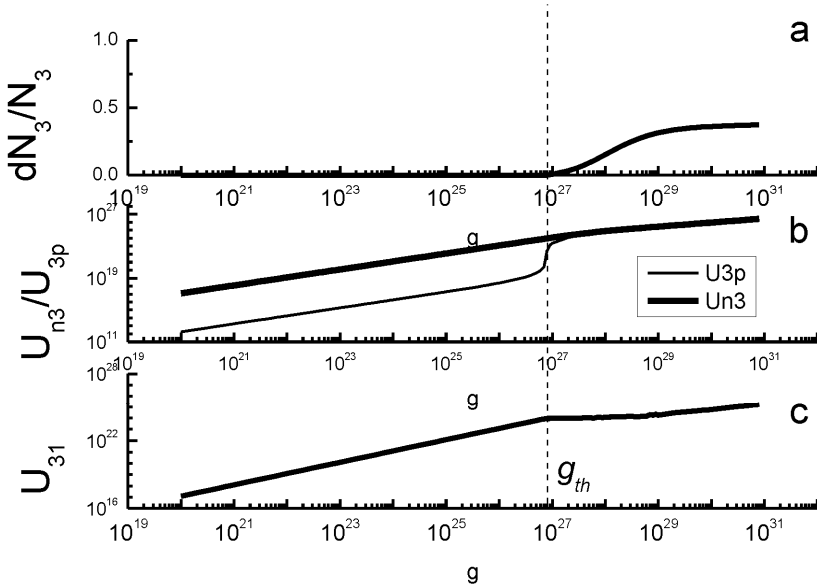


Figure 4.8: Results of the simulations at $t=1 \text{ ms}$ for State 3, according to the recombination mechanism in Figure 4.4. In part (a) $\delta N_3/N_3$ is shown. Part (b) shows the electron-and hole capture rates, and part (c) shows the capture rate from State 3 to State 1.

4.4.3 Filling of the defect states

For State 1, U_{n1} decreases above g_{th} but this does not happen for State 2. The difference in behavior at g_{th} between State 1 and State 2 can be understood by taking a closer look at Eqns. (4.2) and (4.5), which describe the recombination rates U_{n1} , U_{n2} , U_{n3} , and U_{31} . In Eq. 2, parameter N_i^0 reflects the density of empty defect states. In the dark, when the system is in thermal equilibrium, $N_{i\ dark}^0$ is determined by the Fermi-Dirac distribution

$$f = \left(1 + e^{\frac{E_i - E_F}{kT}} \right)^{-1}, \quad (4.10)$$

and the density of empty defect states in the dark follows from

$$N_{i\ dark}^0 = N_i - N_i f, \quad (4.11)$$

in which N_i is the defect-state density. Upon charge carrier excitation and recombination, δN_i increases and, consequently, N_i^0 decreases. According to Eq.(4.6), δn is determined by the generation rate g . Upon increasing g , the population of electrons in the conduction band and in all the states increases. At a certain generation rate, the increase in the state population δN_i matches the density of empty states N_i^0 . When this happens $\delta N_i = N_i^0$ and, according to Eq.(4.2), the filling rates U_{ni} become independent of δn and hence also independent of g . Accordingly, the increase of the state population δN_i saturates at N_i^0 . It should be noted that actually the condition $\delta N_i = N_i^0$ is never reached completely, but close enough to reduce the influence of δn (and g) on U_{ni} in Eq. (4.2), as will be discussed below.

When g is increased to g_{th} , U_{n2} is affected by an increase of δn and δN_2 , which brings the defect-state population to the condition $\delta N_2 = N_2^0$. The shape of the curve in Figure 4.6a shows that the dependence of $\delta N_2/N_2$ on g starts to decrease at g_{th} (the slope of the curve decreases). At this point reduction of the δn term in Eq.(4.2) becomes prominent, and the k -factor changes.

For State 1, when the condition $N_1^0 = \delta N_1$ is reached for 50%, the dependency of U_{n1} on g is expected to decrease, similar to State 2. However, in contrast to State 2, the increase of the occupation level $\delta N_1/N_1$ does not change, as can be seen clearly in Figure 4.7a. This is caused by the second population pathway of State 1, U_{31} , which is not limited by $N_1^0 = \delta N_1$. Because the increase

of $\delta N_i/N_i$ does not change, the population of State 1 will reach the condition $\delta N_i=N_i^0$ much closer than for State 2. This strengthens the cancellation of the δn term in Eq.(4.2) and finally results in a decrease of U_{nl} , rather than a change in k -factor. This explains why the presence of state-to-state recombination leads to a drop of the PL emission of the conduction band to State 1 with increasing excitation power.

4.4.4 The influence of temperature upon defect-state saturation and g_{th}

It is worth noting that the simulated defect-state population of all three states settles exactly at $\delta N_i/N_i=0.5$. The value at which $\delta N_i/N_i$ settles is related directly to the temperature, as will be explained below. Above, it has been shown that stabilization of the defect-state population occurs when the condition $\delta N_i=N_i^0$ is fulfilled. At a temperature of 10 K, f is approximately zero and $N_{i\ dark}=N_i$. In this case the condition $\delta N_i=N_i^0$ is fulfilled at $0.5N_i$, and $\delta N_i/N_i$ yields 0.5. Note that the condition $\delta N_i=N_i^0$ is reached at different values for g for the different defect states.

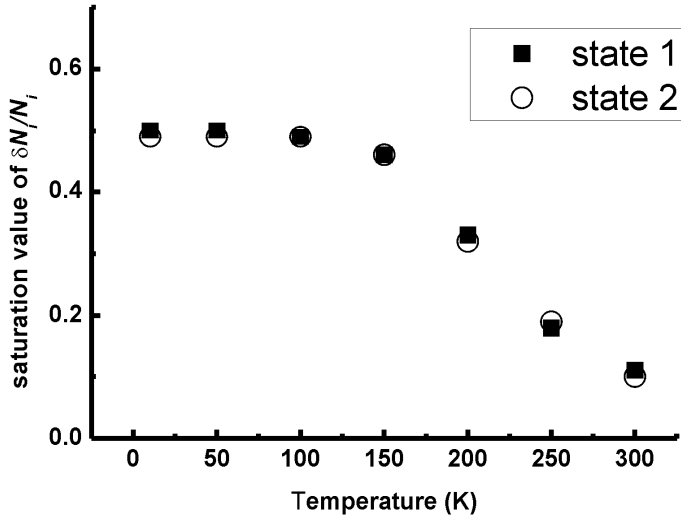


Figure 4.9: Influence of the temperature on the value at which $\delta N_1/N_1$ and $\delta N_2/N_2$ saturate.

At elevated temperatures, f increases. Consequently, N_i^0 decreases with temperature, which affects the value for δN_i where the condition $\delta N_i = N_i^0$ is fulfilled. Figure 4.9 illustrates for State 1 and State 2 how the saturation value for $\delta N_1/N_1$ and $\delta N_2/N_2$ vary upon temperature. At elevated temperatures, the defect-state occupation saturates at lower values, indicating that the condition $\delta N_i = N_i^0$ is reached for lower values of δN_i .

Figure 4.10 shows the influence of the temperature on g_{th} for State 1 and State 2. From this figure it can be seen that at elevated temperatures g_{th} is lower for the coupled defect State 1. This reveals that at higher temperatures a lower excitation power is needed to enable the effect of defect state coupling. Surprisingly, for the uncoupled State 2, g_{th} does not increase with temperature until 200 K, which is in contrast to the behavior of g_{th} related to State 1. This illustrates the effect of thermal ionization, by which electrons are thermally excited to an acceptor state, leaving a hole in the valence band. The hole concentration, p_0 increases and N_2^0 decreases, as is described above. According to Eq.(4.4), direct recombination increases, and U_{n2} decreases (which is the PL intensity) according to Eq.(4.2). The decrease of the sub-bandgap PL intensity with increasing temperature is commonly known for semiconductors.

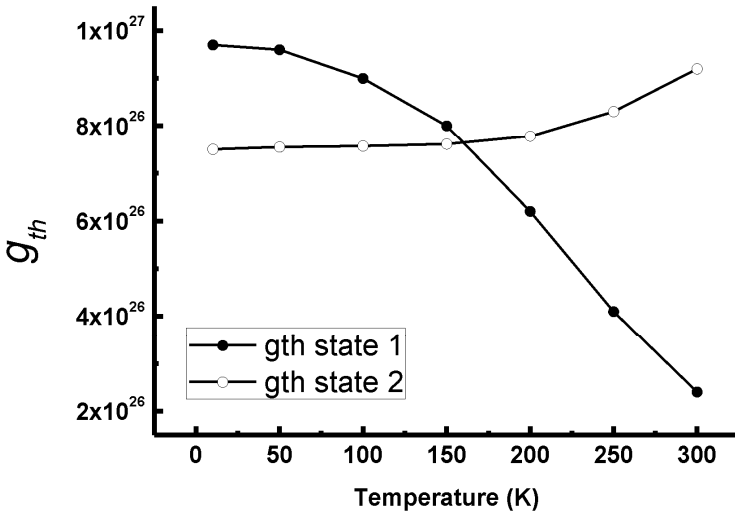


Figure 4.10: Effect of temperature on g_{th} for defect State 1 and 2.

4.4.5 Applying the model to CuInS₂

This elaborated recombination model is now applied to CuInS₂, having a recombination mechanism as presented in Figure 4.3. The initial values of the simulation parameters are obtained from the transient absorption experiments of our previous work¹², for which the same model is used. Next, the parameters are varied carefully to match the experimental observation as close as possible. For the capture cross section of traps in Cu(In,Ga)Se₂ values have been found varying from 10^{-21} to 10^{-23} cm⁻² using the method of DLTS^{13, 14}. The range of 10^{-21} - 10^{-20} cm² that we find for the cross section of holes in CuInS₂ is in good agreement with those. The densities of defect-states of our samples are estimated to be around 10^{14} - 10^{16} cm⁻³. It appears, however, that the simulation results do not change qualitatively when the defect-state density is varied over a large range. The excitation power density g is obtained from the diameter of the focused laser beam, which estimated to be 2 μm. The generation rate ranges from 1×10^{26} (photons/m³) to 4×10^{28} (photons/m³) for the power range used in the experiment

In Table 4.3 the simulation parameters are collected and Figure 4.11a, b, and c show the results for the three emissions at 1.37, 1.28, and 1.54 eV, respectively. In these figures, the simulation and the measured photoluminescence are shown together. Figure 4.11a shows the simulation of $U_{n-0.15}$ and the emission at 1.37 eV as a function of the excitation power, Figure 4.11b shows the simulation of $U_{n-0.2}$ and the PL emission at 1.28 eV as a function of the excitation power, and Figure 4.11c shows the simulation of $U_{1.5-p}$ and the PL emission at 1.54 eV as a function of the excitation power. It should be noted that a linear scale is used in all figures. The scale of the x-axis, which represents the laser power and the parameter g , is similar for all three figures. The simulation shows that $U_{n-0.2}$ and $U_{n-0.15}$ first increase sharply with increasing excitation power. At a certain power a maximum is reached after which the capture rate starts to decrease. While the decrease is initially quite strong it becomes more gradual at higher laser powers. As is evident in Figure 4.11, good agreement between the simulated curve and the experimental data points is found. We conclude that the recombination model derived from transient absorption spectroscopy explains the steady-state photoluminescence of CuInS₂ very well.

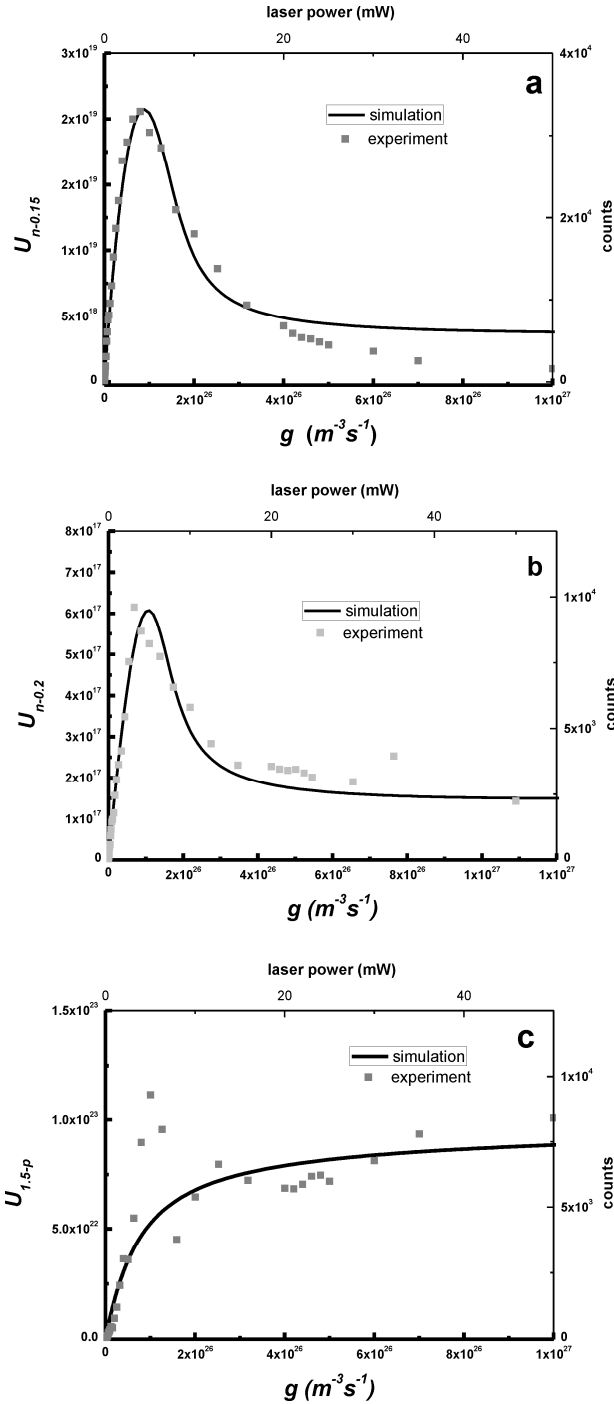


Figure 4.11: Simulation of the PL of CuInS₂, according to the recombination model in Figure 4.3. Shown are the capture rates $U_{n-0.15}$ (a), $U_{n-0.2}$ (b), and $U_{1.5-p}$ (c), which correspond to the PL signal of 1.37, 1.28 and 1.54 eV, respectively, in Figure 4.1 and Figure 4.2. The squares represent the experimental PL data.

The simulation of $U_{n-0.15}$, however, is not completely in agreement with the experiment for high values of g , see Figure 4.11a. Münzberg *et al.*¹⁵ investigated the effect of a nearest-neighbor interaction of a donor-acceptor pair on the capture cross section. They found that the capture cross section is dependent on the charge carrier concentration in the defect state. A change of 2 orders of magnitude is found, when the relative defect-state occupation increases above 10^{-5} . As is shown above, the relative electron concentration of the 0.15 eV state reaches 0.5 at high excitation powers. Following the findings of Münzberg *et al.*, a decrease of the capture cross section at high excitation powers can be expected.

In our model, the capture cross section is considered as a constant, according to the SRH-theory. To investigate the influence of a concentration-dependent capture cross section, we have extended our model by changing the model parameter α , which is the product of the capture cross section, σ , and the thermal velocity of the charge carriers, v_{th} . Since no physical relation of the concentration dependence of the cross section is known, three arbitrarily chosen types of dependencies are investigated, which are presented in Eqns. (4.12), (4.13), and (4.14).

$$\alpha = v_{thermal} \sigma \left(\frac{N - dN}{N} \right), \quad (4.12)$$

$$\alpha = v_{thermal} \sigma \left(\frac{N - dN}{N} \right)^2, \quad (4.13)$$

and

$$\alpha = v_{thermal} \sigma \exp\left(\frac{N - dN}{N} \right) \quad (4.14)$$

The best result is found for correction according to Eq.(4.13). Figure 4.12 shows the results of the modeling, including the concentration dependent capture cross section for $U_{n-0.15}$. As can be seen, the fit matches much better with the experiment.

Table 4.3: Parameters used for simulating the PL experiments

defect state #	1	2	3	4	5	6
energy level (eV)	0.15	0.2	0.25	1.05	1.1	1.5
Density of States (cm ⁻³)	4x10 ¹³	8x10 ¹²	10 ¹⁴	10 ¹⁶	10 ¹⁶	10 ¹⁴
electron capture cross section (cm ²)	10 ⁻²²	10 ⁻²³	10 ⁻¹⁹	10 ⁻²¹	10 ⁻²¹	10 ⁻¹⁹
hole capture cross section (cm ²)	5x10 ⁻²¹	10 ⁻²¹	2.5x10 ⁻²⁰	2x10 ⁻²¹	2x10 ⁻²¹	10 ⁻²¹
electron state-to-state cross sections (cm ²)						
state 5 to 1	1x10 ⁻¹⁶					
state 5 to 2	1x10 ⁻¹⁷					
state 4 to 3	6x10 ⁻¹⁶					
direct recombination α_d	1x10 ⁻¹⁹					

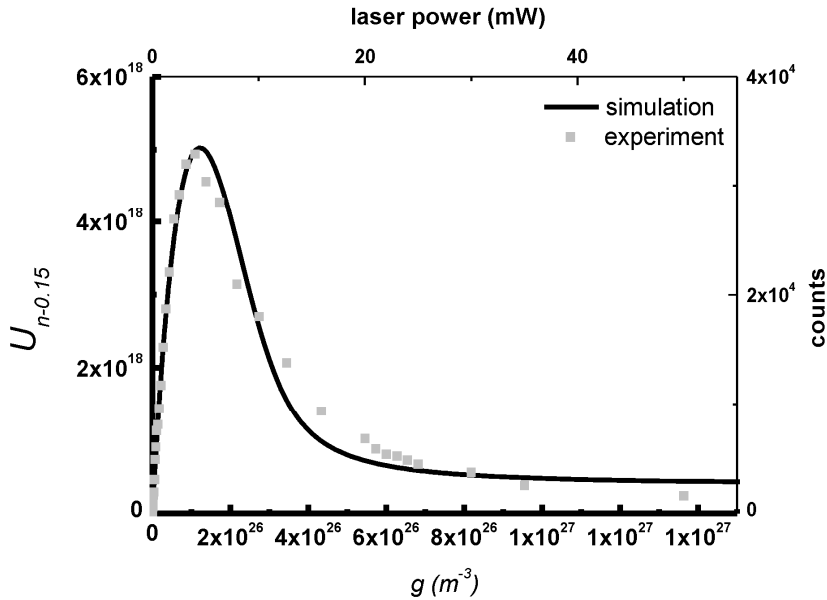


Figure 4.12: Simulation of the PL of CuInS₂, according to the extended recombination model for the capture rate $U_{n-0.15}$. The model has been extended by a concentration dependent capture cross section.

4.5 Summary and conclusions

A recombination model, in which multiple recombination pathways for a single defect state and state-to-state coupling are present, has been developed. This model is applied to simulate excitation power dependent PL measurements. It is shown that the PL intensity of a coupled defect state decreases with increasing excitation power above a certain threshold if state-to-state coupling is strong. The effect of state-to-state coupling is more pronounced at elevated temperatures. The model is applied to explain the laser power dependence of the sub-bandgap photoluminescence of CuInS₂ thin films. It is shown that the model explains the experimental findings for CuInS₂ very well.

REFERENCES

- [1] P. J. Dean, "Photo-Luminescence as a Diagnostic of Semiconductors", *Progress in Crystal Growth and Characterization of Materials* **1982**, 5, 89-174
- [2] T. Schmidt, K. Lischka and W. Zulehner, "Excitation-Power Dependence of the near-Band-Edge Photoluminescence of Semiconductors", *Physical Review B* **1992**, 45, 8989-8994
- [3] R. N. Hall, "Electron-Hole Recombination in Germanium", *Physical Review* **1952**, 87, 387-387
- [4] W. Shockley and W. T. Read, "Statistics of the Recombinations of Holes and Electrons", *Physical Review* **1952**, 87, 835-842
- [5] G. K. Wertheim, "Transient Recombination of Excess Carriers in Semiconductors", *Physical Review* **1958**, 109, 1086-1091
- [6] N. Rega, S. Siebentritt, J. Albert, S. Nishiwaki, A. Zajogin, M. C. Lux-Steiner, R. Kniese and M. J. Romero, "Excitonic luminescence of Cu(In,Ga)Se-2", *Thin Solid Films* **2005**, 480, 286-290
- [7] M. Krunks, O. Bijakina, V. Mikli, H. Rebane, T. Varema, M. Altosaar and E. Mellikov, "Sprayed CuInS₂ thin films for solar cells: The effect of solution composition and post-deposition treatments", *Solar Energy Materials and Solar Cells* **2001**, 69, 93-98
- [8] M. Krunks, O. Bijakina, T. Varema, V. Mikli and E. Mellikov, "Structural and optical properties of sprayed CuInS₂ films", *Thin Solid Films* **1999**, 338, 125-130
- [9] M. Krunks, O. Kijatkina, H. Rebane, I. Oja, V. Mikli and A. Mere, "Composition of CuInS₂ thin films prepared by spray pyrolysis", *Thin Solid Films* **2002**, 403, 71-75
- [10] M. Krunks, V. Mikli, O. Bijakina, H. Rebane, A. Mere, T. Varema and E. Mellikov, "Composition and structure of CuInS₂ films prepared by spray pyrolysis", *Thin Solid Films* **2000**, 361, 61-64
- [11] I. Oja, M. Nanu, A. Katerski, M. Krunks, A. Mere, J. Raudoja and A. Goossens, "Crystal quality studies of CuInS₂ films prepared by spray pyrolysis", *Thin Solid Films* **2005**, 480, 82-86
- [12] J. Hofhuis, J. Schoonman and A. Goossens, "Elucidation of the excited-state dynamics in CuInS₂ thin films", *Journal of Physical Chemistry C* **2008**, 112, 15052-15059
- [13] J. A. M. AbuShama, S. W. Johnston, R. S. Crandall and R. Noufi, "Meyer-Neldel rule and the influence of entropy on capture cross-section determination in Cu(In,Ga)Se-2", *Applied Physics Letters* **2005**, 87, -
- [14] D. L. Young and R. S. Crandall, "An electrostatic barrier to trap filling in CuIn_{1-x}Ga_xSe₂", *Applied Physics Letters* **2003**, 83, 2363-2365
- [15] M. Munzberg, H. Palm and M. Schulz, "Nearest Neighbor Effect on Capture Cross-Sections Measured in Ir Phototransients on Si-In", *Applied Physics a-Materials Science & Processing* **1990**, 50, 255-263

How flash-annealing affects defect association in spray deposited CuInS₂

Abstract

Spray-deposited CuInS₂ is subjected to a flash-anneal experiment in a sulfur environment. Raman-, photoluminescence-, and transient absorption spectroscopy are applied to elucidate the effect of flash-annealing on the crystal quality and the excited state dynamics. It is found that the crystal quality improves substantially upon flash-annealing in sulfur. Deep defect states at 0.2 and 1.1-1.3 eV above the valence band are observed, which are assigned to Cu/In anti-site defects. Excited charge carrier recombination via the deep defect states is found to be present for as-deposited CuInS₂. The recombination rate via the deep defect states decreases after flash-annealing in sulfur, while the Cu/In anti-site defect is not removed. The sulfur vacancy is found to be responsible for charge carrier recombination to the deep defect states. Flash-annealing in sulfur removes the sulfur vacancy and inhibits the recombination via the deep defect states, which is related to the efficiency of CuInS₂- based solar cells.

5.1 Introduction

CuInS₂ (CIS) has excellent properties for conversion of sunlight into electricity. It has a bandgap of 1.55 eV^{1, 2} and an absorption coefficient² of 10⁵ cm⁻¹. CuInS₂-based solar cells with an efficiency of 12.5 % have been demonstrated by Klaer *et al.*³. However, the theoretical efficiency of a CuInS₂-based solar cell of 28.5% is much beyond the record cell for yet unknown reasons⁴.

In order to lower the production costs, novel methods for depositing CIS and CuInSe₂ (CISe) thin films have been developed in the past decade. A reliable and low-cost deposition method for CuInS₂ is spray pyrolysis deposition⁵⁻⁹, which is also investigated in our laboratory^{10, 11}. The spin-off company from our laboratory, i.e., Advanced Surface Technology (AST, Bleiswijk, The Netherlands) has optimized the spray pyrolysis deposition parameters, resulting in an all-sprayed solar cell with an efficiency of 7%. Recently, Valdes *et al.* have successfully deposited CuInSe₂ onto nanoporous TiO₂ using electrodeposition¹². Surprisingly, expensive deposition techniques are not essential for production of cost-efficient CIS-based solar cells. Nevertheless, fundamental research is still needed for a better understanding of the opto-electronic processes in chalcopyrite-based solar cells.

5.1.1 Chalcopyrite material quality

The efficiency of a solar cell is determined by various parameters, among which the presence of crystallographic defects. The chalcopyrite structure of CuInS₂ is complicated because a small deviation from the stoichiometric and/or molecular composition can introduce ionic and/or electronic defects in the material^{13, 14}. From earlier studies of the defect chemistry of chalcopyrite semiconductors the energy positions of several native defects are known¹⁵⁻¹⁷. Most of these defects form shallow donor or acceptor states. Furthermore, besides the chalcopyrite structure another crystal structure for CIS is known, which is referred to as the Cu-Au ordered structure¹⁸. The effect of sulfur- or H₂S-annealing on the quality of chalcopyrite thin films, both CIS and CISe, is a topic of interest. It has been shown that sulfur diffuses into the film by which the crystalline quality of a Cu(In,Ga)Se₂ film improves after annealing in an H₂S atmosphere¹⁹. Siemer *et al.* developed a rapid annealing process, in which the chalcopyrite CuInS₂ structure is formed by sulfurisation of a Cu-In alloy²⁰. Rodriguez-Alvarez *et al.*²¹ contributed to this synthesis route

and investigated the annealing of sputtered Cu-In films in a sulfur or H₂S environment. The improvement of the crystalline quality of spray-deposited CuInS₂ upon annealing in sulfur has been demonstrated by Marsillac *et al.*²².

5.1.2 Anti-site defects

Recently, near infra-red (NIR) photoluminescence (PL) emission in CIS has been investigated in different research groups²³⁻²⁸. Rudigier *et al.*²⁷ have shown that the intensity of the NIR-PL emission is strongly related to the solar cell efficiency. The NIR-PL emissions indicate the presence of deep defect states in the bandgap of CIS. Krustok *et al.*²³⁻²⁵ have developed a nearest neighbor donor-acceptor pair model that explains the origin of the NIR-PL emissions.

In a previous paper²⁸ we have postulated the occurrence of the Cu/In anti-site defect association in CuInS₂, in which the indium-ion and the copper-ion have interchanged their lattice positions, denoted as (Cu_{ln}"In_{cu}"")^x. At low concentration, the Cu/In anti-site defect pair is expected to be present as an isolated point defect within the chalcopyrite structure. An increase of the concentration of these anti-site defects will lead to Cu/In anti-site pair ordering. At even higher concentrations the defect pairs can cluster and form a new crystallographic phase, which is known as the Cu-Au ordered phase. Although the crystallographic geometry of the (Cu_{ln}"In_{cu}"")^x anti-site defect is similar to that of the Cu-Au ordered structure, they are not identical. The Cu-Au ordered structure should be considered as a separate crystallographic phase that co-exists with the chalcopyrite structure. The anti-site defect, however, is a local defect associate and, therefore, does not form long-range order. Cu-Au ordered crystals can be identified by XRD and/or Raman-spectroscopy, while anti-site defects are isolated, or weakly associated defects that appear within the chalcopyrite structure.

We have assigned the NIR-PL emissions to the Cu/In anti-site defect, as is summarized in Table 5.1. Strong evidence is found that these defect pairs prefer a nearest neighbor configuration, which matches with the ideas of Krustok²³⁻²⁵. Furthermore, we have found that the indium vacancy is associated to the Cu/In anti-site defect.

Table 5.1: PL emissions related to the (Cu_{In}^{''}In_{Cu}^{''})^x anti-site defect²⁸

PL emission (eV)	initial state	final state
1.15	In _{Cu} ^{''} at nearest neighbor position	valence band
1.10	In _{Cu} ^{''} at next-nearest neighbor position	valence band
0.95	In _{Cu} ^{''} at nearest neighbor position	Cu _{In} ^{''} at nearest neighbor position
0.85	In _{Cu} ^{''} at next-nearest neighbor position	Cu _{In} ^{''} at next-nearest neighbor position

5.1.3 Recombination mechanism

The recombination of excited charge carriers via defect states in the bandgap is a major route for the loss of solar energy conversion. It is important to understand the influence of the defect chemistry on the recombination mechanisms of charge carriers, in order to develop strategies to improve the conversion efficiency. We have shown that NIR-PL and transient absorption (TA) spectroscopy are excellent tools for studying the role of the Cu/In anti-site defect on the recombination mechanism of CuInS₂ thin films²⁸.

In this paper a rapid thermal procedure in a sulfur environment is applied to spray-deposited CuInS₂ thin films, in order to improve the crystalline quality of the films. The recombination mechanism of the annealed CuInS₂ films is studied in detail with PL and TA spectroscopy. From these investigations we have been able to elucidate how the Cu/In anti-site defect affects the recombination mechanism of excited charge carriers in CuInS₂ thin films.

5.2 Experimental aspects

5.2.1 Sample preparation

CuInS₂ samples have been deposited on quartz substrates by spray pyrolysis deposition as described elsewhere⁵⁻⁹. An automatic spray robot is used to deposit a thin layer of CuInS₂ onto TCO (Pilkington TEC 15, 2.5 mm thickness) substrates. The TCO substrates are cleaned by successive immersion in ethanol in an ultrasonic bath. The deposition of CuInS₂ films was performed by the use of CuCl₂·2 H₂O (99.99% Aldrich), InCl₃ (98%, Aldrich), and thiourea (98%, Aldrich) solved in demi-water. The composition of the solution is such that Cu-rich material is formed. The best results are obtained if the deposition temperature is maintained at 300 °C. The film thickness is controlled by the number of sprays, which has been varied between 50 and 100. The thickness of the film is estimated from the optical density and yields about 0.5-1.0 μm. Spray pyrolysis is performed in ambient atmosphere. After the spray deposition the samples are chemically etched in a 0.5 M KCN solution to remove the excess Cu_xS from the surface.

CuInS₂ that is classified as 'as-deposited' follows the above described deposition sequence. CuInS₂ denoted as 'flash-annealed' is additionally annealed in a sulfur environment by a rapid thermal anneal (RTA) process. In the RTA process the sample is placed in a quartz tube together with an alumina boat containing sulfur powder (Sigma Aldrich, 99.998%). After flushing the tube to remove the oxygen and water from the atmosphere, it is filled with argon slightly above atmospheric pressure, thus preventing air from leaking in. To maintain the small overpressure, a continuous flow is applied during the entire flash-anneal procedure. The sample and the sulfur powder are heated by an IR oven (Research Inc., quad ellipse chamber 5528), which brings the temperature to 500-600°C within a few minutes. The temperature, which heats up to 400 °C within the first minute and reaches 600°C after 3 minutes, is monitored by a thermocouple. The maximum temperature is limited to 630°C by adjusting the power of the IR oven to prevent thermal cracking of the glass substrate. After the anneal time of 5 minutes the IR oven is turned off and the sample is cooled down to room temperature. The cooling down rate is about 500°C in 15 minutes.

5.2.2 Photoluminescence spectroscopy

Photoluminescence measurements are performed in the backscatter mode. The sample is mounted in a closed-cycle helium cryostat (APD Cryogenics CSW-204sl) and cooled to 10 K. Excitation occurs by a Nd:YVO₄ laser, operating at a wavelength of 532 nm (SpectraPhysics Millennia) with a power range of 200 mW to 5 W. Neutral-density filters are used to reduce the laser power below 200 mW. The excitation wavelength is removed from the PL signal by a 620 nm Schott high-pass filter. An optical fiber carries the signal to a monochromator (Acton SpectroPro 2500i). Finally, the spectrum is recorded by a liquid-nitrogen cooled InGaAs detector (Princeton Instruments OMA-V), which is sensitive to the near infra-red (NIR) spectral window between 900 and 1700 nm. PL measurements are integrated over 60 seconds. The PL signal is corrected for the spectral response of the combination of monochromator and CCD camera using a black body spectrum.

Raman measurements are performed in the same setup, also in the backscatter mode. A microscopic lens is used to focus the laser on the sample. A notch filter (Kaiser) is used to filter the excitation wavelength at 532 nm. The Raman-signal is recorded by a silicon CCD array (Princeton Instrument PIXIS-100).

5.2.3 Transient absorption

Transient absorption (TA) spectroscopy is a well know technique but is used scarcely in thin-film solar cell studies. In our previous study we introduced the technique to investigate CuInS₂ thin films²⁸. With transient absorption spectroscopy changes in the optical absorption by electronic states in the bandgap are monitored. A continuous wave monochromatic light beam passes the sample. The photon energy of this so-called probe beam is tunable and can be made resonant with an optical transition. A short laser pulse (the pump beam) excites electrons from the valence band to the conduction band. These excited electrons relax back via the inter bandgap states. This process gives rise to a temporal change in the state populations, which is coupled to the optical absorption strength. A temporal change of the probe beam absorption is measured. The absorption increases when either the initial state is filled or the final state is emptied. The absorption decreases when the opposite occurs. Such temporal decrease in the absorption is referred to as a bleach.

The transient absorption setup is schematically presented in Figure 5.1. The probe beam is generated by a halogen lamp (Oriel) and a monochromator (Acton SpectroPro 150) and is focused onto the sample. Behind the sample, another lens is positioned to direct the beam into a second monochromator

(Acton SpectroPro 150). Silicon and InGaAs photodiodes are used as detectors. The electrical signal is amplified (Femto HCA-200M-20K-C) and recorded with an oscilloscope (Tektronix TDS 744). The pulse beam is generated by a Nd-YAG laser (SpectraPhysics QCR) operating at 355 nm and 10 Hz repetition rate, which pumps an optical parametric oscillator (SpectraPhysics MOPO 710) to generate 532 nm pulses with a duration of 5 ns. After passing through several neutral density filters the energy of the pulse is 4 $\mu\text{J}/\text{pulse}$.

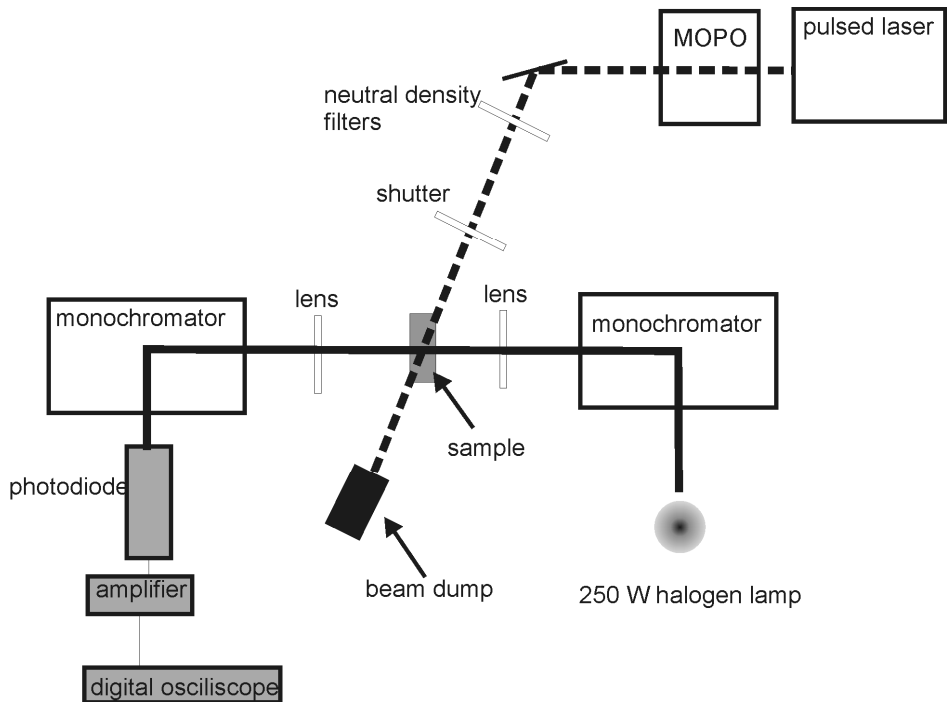


Figure 5.1: Schematic presentation of the TA setup. The probe beam is indicated by a solid line and the pump beam is indicated by a dashed line.

5.3 Results

5.3.1 Raman and PL spectroscopy

Figure 5.2a and b show the Raman spectra for as-deposited CuInS₂ and flash-annealed CuInS₂, respectively. The as-deposited sample has a Raman-peak at 290 cm⁻¹ with a Full Width Half Maximum (FWHM) of 20 cm⁻¹. The flash-annealed sample has a Raman-peak at 290 cm⁻¹ with a FWHM of 3.4 cm⁻¹. For flash-annealed samples, a second peak is observed at 323 cm⁻¹.

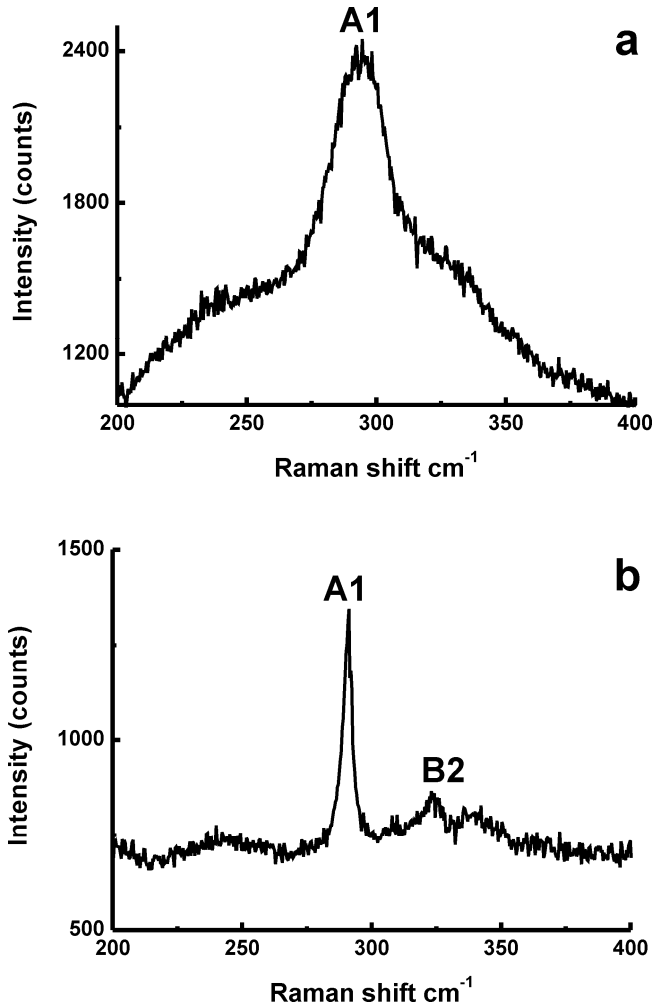


Figure 5.2: (a) Raman spectrum of as-deposited CuInS₂. The Raman-peak at 290 cm⁻¹ has a FWHM of 20 cm⁻¹. (b) Raman spectrum of flash-annealed CuInS₂. The Raman-peak at 290 cm⁻¹ has a FWHM of 3.4 cm⁻¹. At 323 cm⁻¹ a second vibration mode is observed.

Figure 5.3 shows the PL spectrum in the NIR regime for as deposited and flash-annealed CuInS_2 , respectively. The PL curves are fitted by multiple Gaussian distributions, which are shown by the dashed curves in Figure 5.3. For the as-deposited CuInS_2 , an emission at 1.29 eV and a broad emission at 1.15 eV are present. Also PL emissions at 0.85 and 0.95 eV are found.

Compared to as-deposited CuInS_2 , the PL spectrum of the flash-annealed CuInS_2 has less emission at 1.29 eV. The broad emission at 1.15 eV has shifted to 1.18 eV and is reduced in intensity. The inset of Figure 5.3 shows that for flash-annealed CIS a small emission is observed at 0.95 eV, but no emission is found at 0.85 eV.

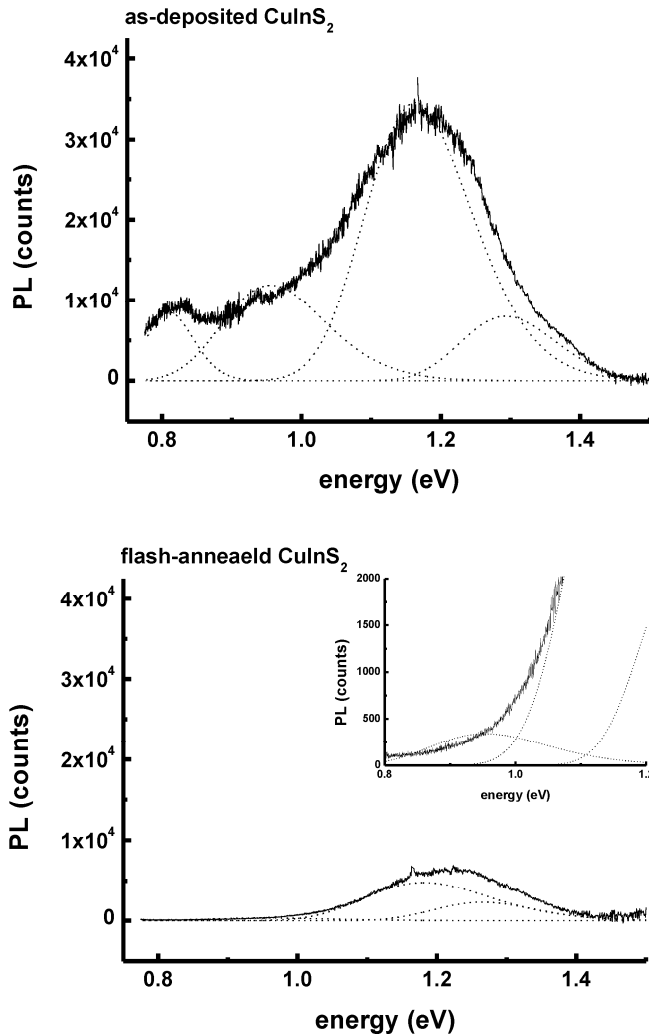


Figure 5.3: Near infra-red PL response of the as-deposited and flash-annealed CuInS_2 . The inset shows a magnification of the PL response of the flash-annealed sample between 0.8 and 1.2 eV.

5.3.2 Transient absorption spectroscopy

Transient absorption experiments are performed at a number of different probe energies for the as-deposited and flash-annealed CuInS₂. All transients are fitted to an exponential decay function with two or three time constants. Table 5.2 and Table 5.3 summarize the transient absorption results for the as-deposited and the flash-annealed CuInS₂, respectively. These tables include the exponential pre-factors and the time constants that result from the exponential fit. A positive pre-factor indicates a transient absorption and a negative pre-factor indicates a bleach of the probe beam.

Table 5.2: TA results for the as-deposited sample.

energy (eV)	A1 ($\times 10^{-3}$)	$\tau 1$ (μs)	A2 ($\times 10^{-3}$)	$\tau 2$ (μs)	A3 ($\times 10^{-3}$)	$\tau 3$ (μs)
1.38	6.00	0.1	18.56	4.2	5.37	72
1.31	7.00	0.1	11.58	5.1	3.62	75
1.24	2.57	0.1	7.24	5.7	2.44	74
1.13	-2.30	1.3	2.21	7.6	0.83	57
1.08	-3.67	1.5	0.99	5.5	0.72	23
1.03	-4.32	1.5			0.63	11
0.99	-4.89	1.5			-0.12	20
0.95	-5.34	1.9			-0.63	170
0.92	-5.78	2.2			-0.95	112
0.88	-6.17	2.6			-1.27	101
0.86	-6.23	3.0			-1.62	91

Table 5.3: TA results for the flash-annealed sample.

energy (eV)	A1 ($\times 10^{-3}$)	$\tau 1$ (μs)	A2 ($\times 10^{-3}$)	$\tau 2$ (μs)	A3 ($\times 10^{-3}$)	$\tau 3$ (μs)
1.38	13.5	0.42	5.73	4.9	2.42	85
1.31	4.95	0.85	2.49	7.1	1.21	96
1.24	3.31	1.20	1.87	8.1	0.97	97
1.13			2.79	3.4	1.06	61
1.08			2.33	3.9	0.92	63
1.03			2.01	4.2	0.81	61
0.99			1.66	4.4	0.67	58
0.95			1.32	4.5	0.53	47

5.3.3 Transient absorption spectroscopy at 1.38 eV

Figure 5.4a and b show the TA response at a probe energy of 1.38 eV for as-deposited and the flash-annealed CuInS₂, respectively. The as-deposited sample shows a transient absorption with three time constants, which are 0.1, 4.2, and 72 μ s. The flash-annealed CuInS₂ has a similar transient. The three time constants for annealed samples are 0.4, 4.9 and 85 μ s. The pre-factors for the second and third time constants (A2 and A3 in Table 5.2 and Table 5.3) become smaller by flash-annealing the CuInS₂ film. The pre-factor of the shortest time constant (A1) increases by flash-annealing.

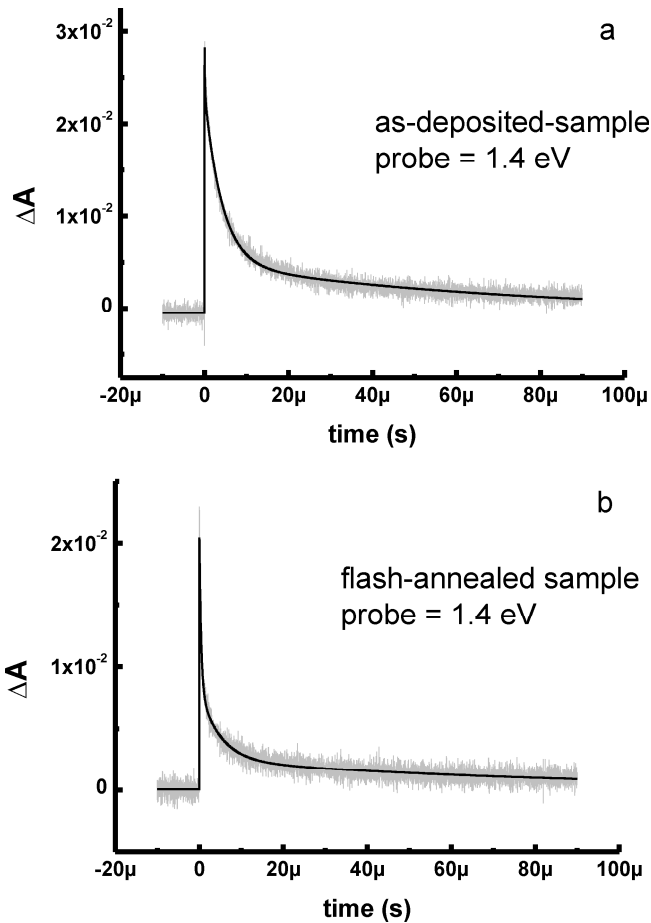


Figure 5.4: Transient Absorption of (a) as deposited CuInS₂ and (b) flash-annealed CuInS₂ for a probe energy of 1.38 eV.

5.3.4 Transient absorption spectroscopy at 1.13-1.03 eV

Figure 5.5a, b, and c show the TA response for the as-deposited samples for probe energies of 1.13, 1.08, and 1.03 eV, respectively. These transients combine a bleach and an absorption with one and two time constants, respectively. At a probe of 1.13 eV, see Figure 5.5a, the transient absorption is dominant and the bleach is weak. At a probe of 1.08 eV, see Figure 5.5b, the transient absorption has decreased while the bleach has increased. Figure 5.5c shows that for a probe energy of 1.03 eV the absorption is weak, and the bleach has become dominant. The time constant of the bleach is 1.3-1.5 μ s, and the time constants of the absorption are 5.5-7.6 μ s and 11-57 μ s, respectively.

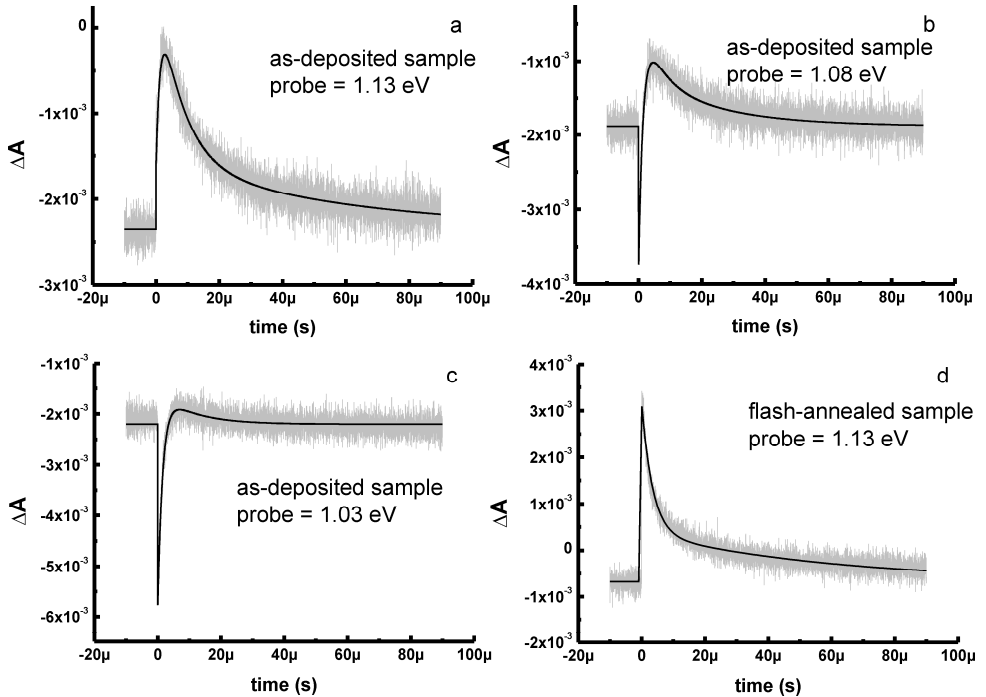


Figure 5.5: Transient Absorption of the as-deposited CuInS₂ for a probe energy of (a) 1.13 eV, (b) 1.08 eV, and (c) 1.03 eV. (d) Transient absorption of the flash-annealed sample for a probe energy of 1.13 eV.

Figure 5.5d shows the TA result for flash-annealed CuInS₂. The transients for these three probe energies are the same, therefore, only the transient at a probe energy of 1.13 eV is shown. This transient has a bleach with two time constants 3.8 μ s and 62 μ s, respectively.

5.3.5 Transient absorption spectroscopy at 0.95 and 0.85 eV

Figure 5.6 shows the TA response for probe energies of 0.95 and 0.85 eV for as-deposited and flash-annealed CuInS₂, respectively. The as-deposited samples have a transient bleach with two time constants of 1.9 μ s and 170 μ s for the 0.95 eV probe, and 3.0 μ s and 91 μ s for the 0.85 eV probe. These transients are shown in Figure 5.6 a and b.

The TA response for the flash-annealed CuInS₂ is shown Figure 5.6c and d. At 0.95 eV, a weak absorption with two time constants of 4.5 en 47 μ s is present. At 0.85 eV, no TA signal is found.

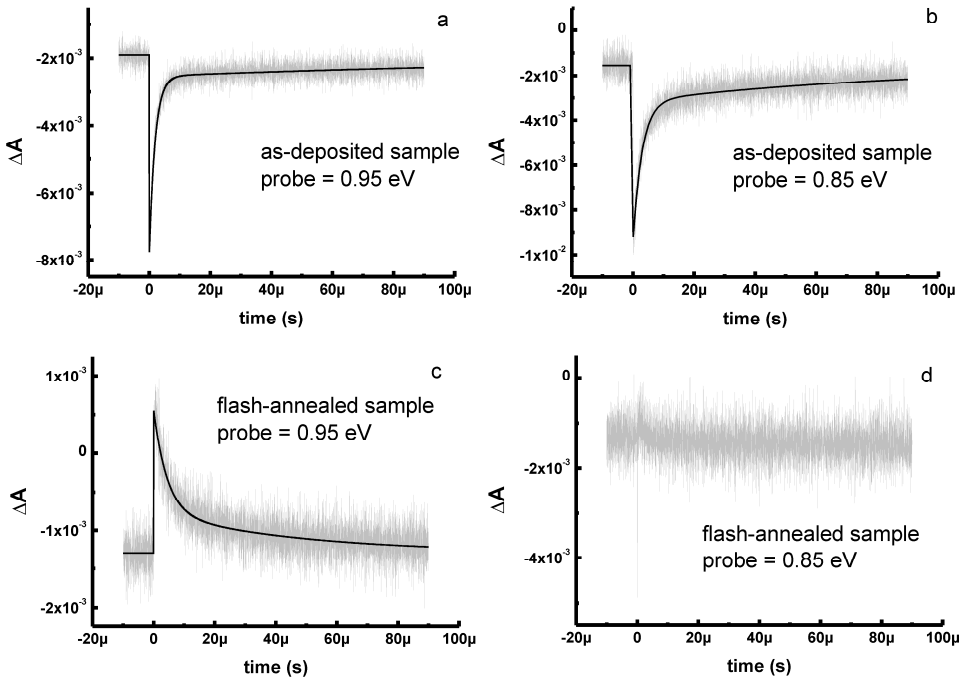


Figure 5.6: Transient absorption for the as-deposited CuInS₂ (a and b) and flash-annealed CuInS₂ (c and d) for a probe energy of 0.95 and 0.85 eV, respectively.

5.4 Discussion

5.4.1 Raman and PL measurements of the as-deposited samples

The Raman-peak at 290 cm⁻¹ for the as-deposited CuInS₂ films (see Figure 5.2) shows that the CuInS₂ film has the chalcopyrite structure^{29, 30}. No Cu-Au crystals are present, since a Raman-peak at 305 cm⁻¹ is not observed. Rudigier *et al.*²⁷ correlated the width of the 290 cm⁻¹ Raman peak to the defect concentration. From the FWHM of 20 cm⁻¹ for as-deposited CuInS₂, a high defect density is concluded.

The NIR PL spectrum of the as-deposited sample, see Figure 5.3, confirms this conclusion. Strong PL emissions are found, which have been assigned to donor-acceptor transitions in previous investigations²⁸. The peak at 1.29 eV is assigned to a PL transition from the conduction band or shallow donor state to the 0.2 eV Cu_{In}" defect state and the 1.15 eV emission is related to recombination from the In_{Cu}" anti-site defect at 1.15 eV to the valence band. The PL emissions at 0.95 and 0.85 eV are assigned to deep-donor (In_{Cu}"") to deep-acceptor (Cu_{In}"") transitions at nearest neighbor and next-nearest neighbor positions, respectively²³⁻²⁵. Raman and PL measurements of the flash-annealed samples

The FWHM of the 290 cm⁻¹ Raman-peak for the flash-annealed sample is similar to that of high-quality CuInS₂, which is grown with more conventional methods^{27, 29, 30}. Also, a peak at 323 cm⁻¹ appears after flash-annealing the CuInS₂ films, which is assigned to the B₂ vibrational mode of CuInS₂ single crystals^{29, 30}. It is concluded that flash-annealing spray-deposited CuInS₂ films in a sulfur atmosphere improves the material quality significantly.

The PL spectrum of the flash-annealed sample, see Figure 5.3, shows that the deep-donor to deep-acceptor transition at 0.85 eV has disappeared. This transition is assigned to the next-nearest neighbor transition of the (Cu_{In}"In_{Cu}"")^x anti-site defect, as is presented in Table 5.1. From this, it is concluded that the next-nearest neighbor defect state association is removed by flash-annealing CuInS₂ in sulfur. A small emission at 0.95 eV shows that the nearest neighbor defect association is not completely removed, but is reduced strongly in PL emission strength. Also the 1.29 and 1.15 eV PL transmissions are reduced in intensity after annealing.

5.4.2 Construction of the band diagrams

As-deposited CuInS₂

The PL measurements of as-deposited CuInS₂ show similar behavior as in our previous work²⁸. Therefore, the band diagram for as-deposited CuInS₂ is taken from this work, and is shown in Figure 5.7a. The PL emission at 1.1 eV is assigned to the nearest neighbor and next-nearest neighbor $\text{In}_{\text{Cu}}^{\bullet\bullet}$ anti-site defect at 1.15 and 1.1 eV above the valence band, respectively. The PL emission at 0.95 eV is assigned to the $\text{In}_{\text{Cu}}^{\bullet\bullet} \rightarrow \text{Cu}_{\text{In}}^{\bullet}$ transition in the nearest neighbor configuration and the PL emission at 0.85 eV to the $\text{In}_{\text{Cu}}^{\bullet\bullet} \rightarrow \text{Cu}_{\text{In}}^{\bullet}$ transition in the next-nearest neighbor configuration. The defect states that belong to the nearest neighbor anti-site defect (0.2 eV and 1.15 eV) and the next-nearest neighbor anti-site defect (0.25 and 1.1 eV) differ only 0.05 eV in energy. Therefore, the $\text{Cu}_{\text{In}}^{\bullet}$ and $\text{In}_{\text{Cu}}^{\bullet\bullet}$ defect states are considered as doublet states at 0.2 and 1.1 eV, respectively.

Flash-annealed CuInS₂

The band diagram of the flash-annealed CuInS₂ is constructed from the PL data of this work, in analogy to the as-deposited samples. According to the PL emission at 1.1-1.2 eV, a defect state at 1.1 eV above the valence band is expected. This defect level belongs to the $\text{In}_{\text{Cu}}^{\bullet\bullet}$ anti-site defect. The PL emission at 0.95 eV is assigned to the $\text{In}_{\text{Cu}}^{\bullet\bullet} \rightarrow \text{Cu}_{\text{In}}^{\bullet}$ transition in the nearest neighbor configuration, which gives reason to include a defect state at 0.2 eV that is assigned to the $\text{Cu}_{\text{In}}^{\bullet}$ defect. The $\text{Cu}_{\text{In}}^{\bullet}$ and $\text{In}_{\text{Cu}}^{\bullet\bullet}$ defect states at 0.2 and 1.1 eV, respectively, are not a doublet for the flash-annealed CuInS₂ since the next-nearest neighbor emission at 0.85 eV is not present. Because the PL emission at 1.1 eV is more intense than the 0.95 eV emission, the coupling between the associated defects, i.e., the $\text{In}_{\text{Cu}}^{\bullet\bullet} \rightarrow \text{Cu}_{\text{In}}^{\bullet}$ transition, is not strong, as is indicated by the thickness of the arrows in Figure 5.7. The constructed band-diagrams will be used to explain the TA experiments.

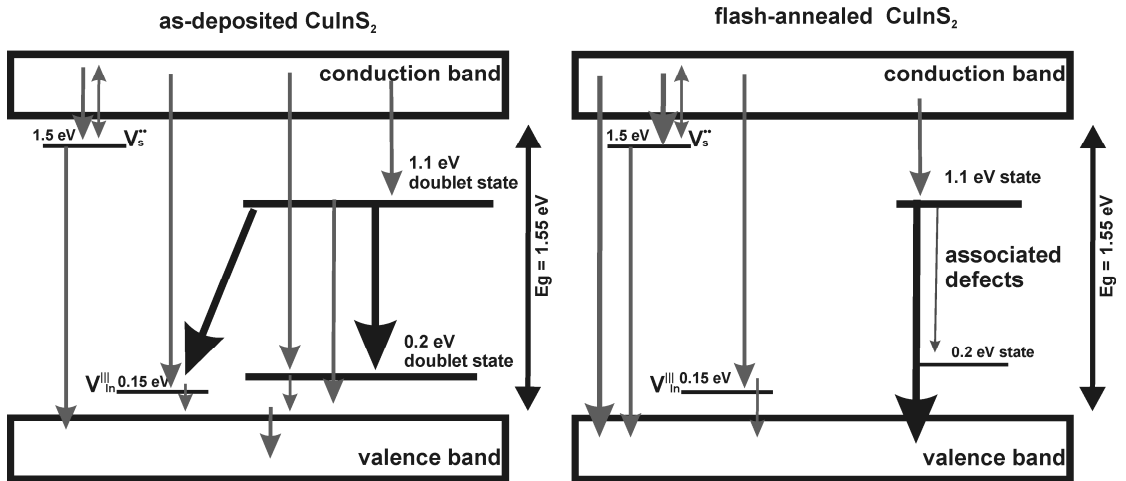


Figure 5.7: Band-diagrams and recombination mechanisms for the as-deposited (left) and the flash-annealed (right) CuInS_2 .

5.4.3 Introduction transient absorption measurements

The recombination mechanism of the excited charge carriers can be extracted from transient absorption spectroscopy. Our previously reported TA results for as-deposited CuInS_2 will be summarized first as they serve as a reference for the annealed samples. The films of the present study are produced under slightly different circumstances, which lead to small differences in composition and, therefore, defects and defect densities. A change in defects and defect densities affects the recombination mechanisms and, therefore, the TA behavior, as will be shown below. The TA results are discussed starting with large probe energies. First the as-deposited CuInS_2 is considered, followed by the flash-annealed material.

5.4.4 Probe energy of 1.38 eV

As-deposited CuInS_2

The probe energy of 1.38 eV probes the transitions from the 0.15 and 0.2 eV doublet acceptor states to the 1.5 eV state and the conduction band, see Figure 5.7a. Three lifetimes are found, being 0.1, 4.2, and 72 μs . It is assumed that the short lifetime components correspond to shallow defect states and that deep defect states have longer lifetime components. In contrast to our previous results, the 0.1 μs component is an absorption, while in our earlier study a bleach with a similar time constant has been found. The observed bleach in the previous investigation was assigned to saturation of the 1.5 eV state, which has a lifetime of 0.1 μs . The presence of a transient absorption in this work indicates that the 1.5 eV state is no longer saturated and, therefore, does not inhibit the probe absorption. Accordingly, transient absorption from the 0.15 eV state to the 1.5 eV state becomes possible and reflects the population of the 0.15 eV state, which has a lifetime of 0.1 μs .

The second and third lifetime components, being 4.2 and 72 μs , have been assigned before²⁸. Population of the 0.2 eV doublet state after the excitation pulse enables absorption to the conduction band. The lifetime of the 0.2 eV population is 4.2 μs . The time constant of 72 μs is the depopulation time of the 1.1 eV doublet state, which empties via the 0.15 eV state and the 0.2 eV doublet state.

Flash-annealed CuInS_2

For the flash-annealed CuInS_2 a similar transient with three time constants is found. The lifetime components can be assigned similarly as for the as-deposited samples. While the time-constants are the same, the pre-factors differ from those of as-deposited CuInS_2 . This can also be seen from the shape of the TA curve, which differs from the as-deposited TA curve, see Figure 5.4a and b. The pre-factors A2 and A3, which belong to the 0.2 eV defect state population and the 1.1 eV defect state population, respectively, have decreased. From this, we conclude that recombination via deep defect states is reduced after annealing the samples. The increase of the pre-factor A1, which belongs to the population of the 0.15 eV defect state, shows that more excited charges now recombine directly to the 0.15 eV state.

5.4.5 Probe energies of 1.13 eV - 1.03 eV

As-deposited CuInS₂

The observed sum of a bleach and an absorption for as-deposited CuInS₂ differs from the findings in our previous work, where only a transient bleach and no absorption is observed at these probe energies²⁸. In our previous work the transitions in this energy range are assigned to electron excitation from the valence band into the In_{Cu}^{••} doublet state at 1.15 eV. The observed bleach could be explained by a saturation of the In_{Cu}^{••} defect state. In the present samples a transient absorption, and not a bleach, is observed at the probe energy of 1.13 eV. We find it hard to believe that at 1.13-1.03 eV an absorption from the valence band is probed, since it suggests an increase of the electron population in the valence band. Therefore, we believe that the 1.13-1.03 eV probe starts in the 0.15 eV state and probes up to a level at 1.3 eV. The band-diagram of Figure 5.7 does not include a state at 1.3 eV, but there are good reasons to postulate the presence of such a state, as will be explained below.

The following observations bring us to conclusions that at 1.3 eV above the valence band defect states are present. First, a PL emission at 1.29 eV is observed. Second, the width of the 1.15 eV PL emission indicates that a large spread in energy states is involved. This spread in energy must be related either to the In_{Cu}^{••} defect state, or to the valence band. The spread in energy of the holes in the valence band is limited to about 50 meV at room temperature. Therefore, we conclude that the spread in energy states of the In_{Cu}^{••} must be wide, up to 1.3 eV. Third, Zhang *et al.*¹⁴ have calculated the defect transition levels of an In_{Cu}^{••} anti-site defect in CuInSe₂. They found two levels at 0.76 and 0.85 eV above the valence band, which are separated 0.09 eV from each other. If for CuInS₂ the lower state lies at 1.15 eV the higher state is expected about 1.25 eV.

By assuming that the In_{Cu}^{••} defect introduces a distribution of states between 1.1-1.3 eV, this does not change the conclusions from our earlier investigations. Therefore, we consider the 1.15 eV defect as a wide distribution of energy-states, which ranges from 1.1 to 1.3 eV, as is shown in Figure 5.8. We assume that when this wide distribution of energy states is filled with charge carriers, the filling starts at the lowest energy level.

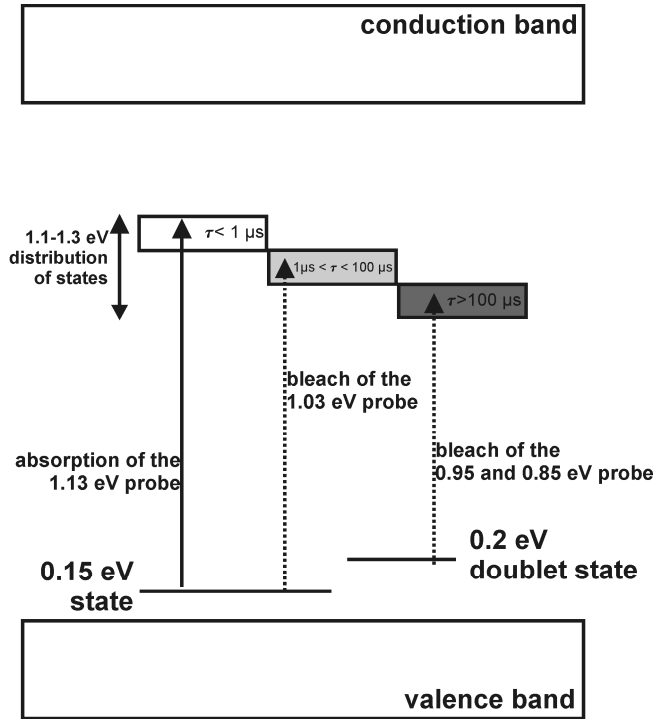


Figure 5.8: Band diagram of CuInS₂, including the 1.1-1.3 eV defect band. The filling of the 1.1-1.3 eV defect band is presented by the shaded areas. The transient absorption probes of 1.13, 1.03, 0.95 and 0.85 eV are indicated in the picture. A solid line indicates a transient absorption and a dashed line indicates a transient bleach.

First the transient bleach at 1.03 eV having a decay time of 1.5 μs is considered, according to Figure 5.8. This bleach dominates at the probe energy of 1.03 eV and is caused by a filling of the middle energy levels of the 1.1-1.3 eV distribution of energy states, as is shown in Figure 5.8. This filling inhibits the absorption of the probe from the 0.15 eV defect state. The time component of 1.5 μs is the lifetime of electrons that fill the middle level of the 1.1-1.3 eV distribution of energy states.

Next, we consider the transient absorption at 1.13 eV and with two decay times being 7.6 and 57 μs . This energy probes from the 0.15 eV state to the upper part of the 1.1-1.3 eV distribution of energy states, as is shown in Figure 5.8. Because the upper part of the 1.1-1.3 distribution of energy states is empty, absorption of the probe from the 0.15 eV state is possible. The observed lifetimes correspond to the population time of the 0.15 eV state, which is 7.6 μs ,

and the population of the 1.1-1.3 eV distribution of energy states that depopulates via the 0.15 eV state, which is 57 μ s.

Flash-annealed CuInS₂

From the PL experiments it is found that flash-annealed CuInS₂ also has a distribution of energy states at 1.1-1.3 eV, according to the wide PL emission at 1.15 eV. Accordingly, at probe energies between 1.13-1.03 eV also the transition from the 0.15 eV state to the 1.1-1.3 eV distribution of energy states is probed, as is shown in Figure 5.8. In contrast to as-deposited CuInS₂, a transient bleach is not found for annealed CuInS₂, instead a transient absorption is observed. This can only occur when the 1.1-1.3 eV distribution of energy states is not saturated. The transient absorption is caused by population of the V_{In}'' at 0.15 eV and the corresponding lifetime of 3.4-4.2 μ s reflects the population of the V_{In}'' . The second lifetime of 61-63 μ s is the population lifetime of the 1.1-1.3 eV distribution of energy states, which depopulates via the V_{In}'' .

5.4.6 Probe energy of 0.95 eV and 0.85 eV

As-deposited CuInS₂

At probe energies of 0.95 and 0.85 eV the transition between the 0.2 eV doublet state (Cu_{In}'') and the 1.1-1.3 eV distribution of energy states (In_{Cu}'') is monitored. For as-deposited CuInS₂, a strong transient bleach with two lifetimes, 2-3 μ s and 91-170 μ s, is found. In our earlier investigations, a fast bleach component (<0.1 μ s) is found at these energies, which has been assigned to a fast depopulation of the 0.2 eV doublet state. For the present samples, a bleach of 2-3 μ s is found, which is too long to be assigned to fast depopulation of the 0.2 eV doublet state. Population of the middle part of the 1.1-1.3 eV distribution of energy states inhibits the absorption of the probe. A lifetime of 2-3 μ s is assigned to this part of the defect band, as is indicated in Figure 5.8. The long lifetime of 91-170 μ s is caused by population of the lower part of the 1.1-1.3 eV distribution of energy states, which also inhibits the absorption of the probe.

Flash-annealed CuInS₂

Flash-annealed CuInS₂ shows a transient absorption at a probe of 0.95 eV, which probes the transition from the 0.2 eV state (Cu_{In}'') to the 1.1-1.3 eV distribution of energy states (In_{Cu}''). A transient absorption can occur only when the 1.1-1.3 eV distribution of energy states is not saturated with electrons. Population of the 0.2 eV defect state allows absorption of the probe beam to the

1.1-1.3 eV distribution of energy states. The lifetime component of 4.5 μ s is the population time of the Cu_{In}^{••} at 0.2 eV and the lifetime component of 47 μ s reflects the depopulation of the In_{Cu}^{••} defect state, which depopulates via the Cu_{In}^{••} defect state at 0.2 eV. At 0.85 eV, no TA signal is found, which is in agreement with the results of the PL experiment that also shows no emission at this energy.

5.4.7 The effect of flash-annealing on the recombination mechanism of CuInS₂ thin films and the associated defect state association.

State-to-state recombination

In our earlier investigations we postulated a mechanism for the formation of defect-state association in CuInS₂^{28, 31}. We believe that the (Cu_{In}^{••}In_{Cu}^{••})^x, V_{In}^{••}, and the V_s^{••} defects are associated, which leads to high state-to-state recombination rates. In the previous work, we have developed a recombination model that is based on the Shockley, Read, and Hall (SRH) theory, which is modified to include state-to-state recombination paths. The TA experiments have been successfully simulated using our model. We have shown that the observed multiple lifetime components can only occur when state-to-state recombination paths are present. In CuInS₂, these state-to-state recombinations include In_{Cu}^{••} → Cu_{In}^{••} at both the nearest neighbor and the next-nearest neighbor configuration and In_{Cu}^{••} → V_{In}^{••}, as is shown in Figure 5.7.

The PL emissions and the TA transitions at 0.95 and 0.85 eV show that the In_{Cu}^{••} → Cu_{In}^{••} recombination path is present in the current batch of as-deposited CuInS₂. From the presence of multiple exponential decay times for the 0.15 eV state, we conclude that also the In_{Cu}^{••} → V_{In}^{••} recombination path is present.

It is concluded from the PL experiments that In_{Cu}^{••} → Cu_{In}^{••} recombination path for the next-nearest neighbor configuration is removed upon flash-annealing CuInS₂ in a sulfur environment. The In_{Cu}^{••} → Cu_{In}^{••} recombination path for the nearest neighbor configuration, which has a PL emission at 0.95 eV, is still present but shows a strongly reduced PL intensity. Additionally, the PL emission at 1.15 eV, which is the recombination path from the In_{Cu}^{••} to the valence band, is also reduced in strength. From the TA experiments, it is concluded that the In_{Cu}^{••} → Cu_{In}^{••} recombination path is still present after the flash-anneal experiment. Multiple lifetime components are

observed for the $V_{\text{In}}^{\text{'''}}$ at 0.15 eV, which indicates the presence of the $\text{In}_{\text{Cu}}^{\text{''}} \rightarrow V_{\text{In}}^{\text{'''}}$ recombination path for flash-annealed CuInS₂.

Population rate from the conduction band to the $V_{\text{In}}^{\text{'''}}$ at 0.15 eV.

From the change in shape of the transient absorption at 1.38 eV we conclude that the recombination rate from the conduction band to the $V_{\text{In}}^{\text{'''}}$ at 0.15 eV is larger after flash-annealing CuInS₂ in sulfur, as is explained below. The first peak is much sharper for the flash-annealed CuInS₂ than for as-deposited CuInS₂. This peak belongs to the population of the $V_{\text{In}}^{\text{'''}}$ defect state from the conduction band. When more excited charge carriers recombine directly to the $V_{\text{In}}^{\text{'''}}$ defect state, the population density of the 0.15 eV defect state is larger and the transient absorption signal that belongs to this population path is stronger.

When more excited charges recombine to the $V_{\text{In}}^{\text{'''}}$, less charges will populate the other defect states. A decrease of the population density of the $\text{Cu}_{\text{In}}^{\text{''}}$ defect state at 0.2 eV and the $\text{In}_{\text{Cu}}^{\text{''}}$ defect state at 1.1-1.3 eV defect states and an increase in population of the $V_{\text{In}}^{\text{'''}}$ defect state at 0.15 eV will reduce the state-to-state recombination rates, according to our SRH-based recombination model²⁸. This lowers the intensity of the long tail in the transient absorption at 1.38 eV, which accordingly sharpens the first peak.

This change in shape of the transient absorption signal is also evident in the exponential pre-factors that belong to the transient absorption at 1.38 eV. For flash-annealed CuInS₂, the pre-factors for the $\text{CB} \rightarrow V_{\text{In}}^{\text{'''}}$ transition are much larger than for the as-deposited CuInS₂ and vice versa. From this, we conclude that the recombination rate of the $\text{CB} \rightarrow V_{\text{In}}^{\text{'''}}$ transition increases upon flash-annealing in sulfur, while the state-to-state recombination rates decrease.

Population rate of the 1.1-1.3 eV distribution of energy states

The sign of the TA signal at 0.95 eV has changed after annealing in sulfur. The as-deposited CuInS₂ shows a transient bleach, which is the result of a saturation of the 1.1-1.3 eV distribution of energy states, as is explained above. The flash-annealed CuInS₂, however, shows a transient absorption, which can only occur when the 1.1-1.3 eV distribution of energy states is not saturated.

Saturation of a defect state occurs when the population rate is larger than the depopulation rate. As is evident from the transient absorption experiments, the lifetime of the $\text{In}_{\text{Cu}}^{\text{''}}$ defect state at 1.1-1.3 eV, which represents the depopulation rate of this state, does not change after flash-annealing. Since saturation is not found for flash-annealed CuInS₂ and the depopulation rate does not change, it is concluded that the population rate of the

1.1-1.3 eV distribution of energy states decreases upon flash-annealing. This conclusion is supported by the reduced PL intensity, which indeed is observed for the 1.1-1.3 eV distribution of energy states after flash-annealing CuInS₂ in sulfur.

5.4.8 The role of sulfur

It is expected that sulfur vacancies are removed by annealing in a sulfur environment and that annealing improves the crystal quality. However, it is not expected that annealing in sulfur repairs the $(\text{Cu}_{\text{In}}\text{In}_{\text{Cu}})^{\times}$ anti-site defect. We have no indications that the concentration of the $(\text{Cu}_{\text{In}}\text{In}_{\text{Cu}})^{\times}$ anti-site defect decreased after annealing in sulfur. The change in PL intensity from the $\text{In}_{\text{Cu}}^{\bullet\bullet}$ at 1.1-1.3 eV is explained by a change of the recombination rate. In order to explain the effect of sulfur vacancies on the recombination mechanism, we postulate that a sulfur vacancy is associated to the anti-site defect as is found before for the $\text{V}_{\text{In}}^{\bullet}$. It is concluded that recombination to the anti-site defect occurs via the sulfur vacancy. Upon removing the sulfur vacancies by annealing in sulfur the recombination path to the $\text{In}_{\text{Cu}}^{\bullet\bullet}$ is inhibited. This explains the decrease in PL emission from the $\text{In}_{\text{Cu}}^{\bullet\bullet}$ defect state to the valence band and the change in TA pre-factors for the transition to the $\text{In}_{\text{Cu}}^{\bullet\bullet}$ defect state, even though the concentration of the Cu/In anti-site defect does not change.

The disappearance of the next-nearest neighbor coupling can also be explained by removing the sulfur vacancy. When a sulfur vacancy is present in the same unit cell, it provides space for a Cu- or In-ion to occupy an off-center or interstitial position. Krustok *et al.* suggest next-nearest neighbor coupling involving interstitial defects²⁵. By removing a sulfur vacancy, the lattice energy of the next-nearest neighbor defect at an interstitial position becomes too high. The interstitial shifts to a lattice position, which cancels the next-nearest neighbor defect. Meanwhile, the anti-site defect, in which the $\text{Cu}_{\text{In}}^{\bullet}$ and $\text{In}_{\text{Cu}}^{\bullet\bullet}$ both occupy a lattice position, remains.

5.4.9 Solar cells

It is shown that the recombination rate to the 1.15 eV state decreases after annealing in sulfur. This indirectly affects the open cell potential of the CuInS₂-based solar cell. Rudigier *et al.* have shown that the open cell potential of CuInS₂-based solar cells increases when the intensity of the 1.1 eV PL peak decreases²⁷. Because the lifetime of charges that are trapped at deep defect states can be long, a significant amount of charge can be stored. This influences the Fermi-level of the CuInS₂, which is of direct relevance to the solar cell voltage. In this study, we have shown that saturation of the 1.1 eV defects does not occur when the recombination path through the sulfur vacancy is not present. This explains why the open cell voltage is related to the intensity of the 1.15 eV PL peak.

5.5 Summary and conclusions

We have studied the effect of flash-annealing in a sulfur environment on spray-deposited CuInS₂. The crystal quality of spray-deposited CuInS₂ improves after flash-annealing in sulfur, as is evident from the Raman spectroscopy. From PL spectroscopy it is concluded that after flash-annealing the PL emission from deep defect states has decreased. Furthermore, the next-nearest neighbor Cu/In anti-site defect association disappears. The effect of flash-annealing in sulfur on the charge carrier recombination mechanism of spray-deposited CuInS₂ is studied by means of Transient Absorption spectroscopy. It is shown that the recombination rate via the deep anti-site defect $\text{In}_{\text{Cu}}^{\bullet\bullet}$ decreases and the next-nearest neighbor effect disappears after annealing in sulfur. It is elaborated that sulfur vacancies act as a recombination trap for the $\text{In}_{\text{Cu}}^{\bullet\bullet}$ defect and initiate the next-nearest neighbor association. These findings can be related to the solar cell efficiency of CuInS₂-based solar cells.

REFERENCES

- [1] R. Klenk, U. Blieske, V. Dieterle, K. Ellmer, S. Fiechter, I. Hengel, A. JägerWaldau, T. Kampschulte, C. Kaufmann, J. Klaer, M. C. LuxSteiner, D. Braunger, D. Hariskos, M. Ruckh and H. W. Schock, "Properties of CuInS₂ thin films grown by a two-step process without H₂S", *Solar Energy Materials and Solar Cells* **1997**, 49, 349-356
- [2] M. Kanzari and B. Rezig, "Effect of deposition temperature on the optical and structural properties of as-deposited CuInS₂ films", *Semiconductor Science and Technology* **2000**, 15, 335-340
- [3] J. Klaer, J. Bruns, R. Henninger, K. Seimer, R. Klenk, K. Ellmer and D. Braunig, "Efficient CuInS₂ thin-film solar cells prepared by a sequential process", *Semiconductor Science and Technology* **1998**, 13, 1456-1458
- [4] S. Siebentritt, "Wide gap chalcopyrites: material properties and solar cells", *Thin Solid Films* **2002**, 403, 1-8
- [5] M. Krunks, O. Bijakina, V. Mikli, H. Rebane, T. Varema, M. Altsaar and E. Mellikov, "Sprayed CuInS₂ thin films for solar cells: The effect of solution composition and post-deposition treatments", *Solar Energy Materials and Solar Cells* **2001**, 69, 93-98
- [6] M. Krunks, O. Bijakina, T. Varema, V. Mikli and E. Mellikov, "Structural and optical properties of sprayed CuInS₂ films", *Thin Solid Films* **1999**, 338, 125-130
- [7] M. Krunks, O. Kijatkina, H. Rebane, I. Oja, V. Mikli and A. Mere, "Composition of CuInS₂ thin films prepared by spray pyrolysis", *Thin Solid Films* **2002**, 403, 71-75
- [8] M. Krunks, V. Mikli, O. Bijakina, H. Rebane, A. Mere, T. Varema and E. Mellikov, "Composition and structure of CuInS₂ films prepared by spray pyrolysis", *Thin Solid Films* **2000**, 361, 61-64
- [9] I. Oja, M. Nanu, A. Katerski, M. Krunks, A. Mere, J. Raudoja and A. Goossens, "Crystal quality studies of CuInS₂ films prepared by spray pyrolysis", *Thin Solid Films* **2005**, 480, 82-86
- [10] M. Nanu, J. Schoonman and A. Goossens, "Nanocomposite three-dimensional solar cells obtained by chemical spray deposition", *Nano Letters* **2005**, 5, 1716-1719
- [11] R. O'Hayre, M. Nanu, J. Schoonman, A. Goossens, Q. Wang and M. Gratzel, "The influence of TiO₂ particle size in TiO₂/CuInS₂ nanocomposite solar cells", *Advanced Functional Materials* **2006**, 16, 1566-1576
- [12] M. Valdes, M. A. Frontini, M. Vazquez and A. Goossens, "Low-cost 3D nanocomposite solar cells obtained by electrodeposition of CuInSe₂", *Applied Surface Science* **2007**, 254, 303-307
- [13] D. Perniu, S. Vouwzee, A. Duta and J. Schoonman, "Defect chemistry of solar cell chalcopyrite materials", *Journal of Optoelectronics and Advanced Materials* **2007**, 9, 1568-1571
- [14] S. B. Zhang, S. H. Wei, A. Zunger and H. Katayama-Yoshida, "Defect physics of the CuInSe₂ chalcopyrite semiconductor", *Physical Review B* **1998**, 57, 9642-9656
- [15] J. J. M. Binsma, L. J. Giling and J. Bloem, "Luminescence of CuInS₂. 2. Exciton and near Edge Emission", *Journal of Luminescence* **1982**, 27, 55-72

- [16] J. J. M. Binsma, L. J. Giling and J. Bloem, "Luminescence of CuInS₂. I. The Broad-Band Emission and Its Dependence on the Defect Chemistry", *Journal of Luminescence* **1982**, 27, 35-53
- [17] H. Y. Ueng and H. L. Hwang, "The Defect Structure of CuInS₂. I. Intrinsic Defects", *Journal of Physics and Chemistry of Solids* **1989**, 50, 1297-1305
- [18] J. Alvarez-Garcia, B. Barcones, A. Perez-Rodriguez, A. Romano-Rodriguez, J. R. Morante, A. Janotti, S. H. Wei and R. Scheer, "Vibrational and crystalline properties of polymorphic CuInC₂ (C=Se,S) chalcogenides", *Physical Review B* **2005**, 71, -
- [19] B. M. Basol, A. Halani, C. Leidholm, G. Norsworthy, V. K. Kapur, A. Swartzlander and R. Matson, "Studies on sulfur diffusion into Cu(In,Ga)Se-2 thin films", *Progress in Photovoltaics* **2000**, 8, 227-235
- [20] K. Siemer, J. Klaer, I. Luck, J. Bruns, R. Klenk and D. Braunig, "Efficient CuInS₂ solar cells from a rapid thermal process (RTP)", *Solar Energy Materials and Solar Cells* **2001**, 67, 159-166
- [21] H. Rodriguez-Alvarez, I. M. Kotschau and H. W. Schock, "Pressure-dependent real-time investigations on the rapid thermal sulfurization of Cu-In thin films", *Journal of Crystal Growth* **2008**, 310, 3638-3644
- [22] S. Marsillac, M. C. Zouaghi, J. C. Bernede, T. Ben Nasrallah and S. Belgacem, "Evolution of the properties of spray-deposited CuInS₂ thin films with post-annealing treatment", *Solar Energy Materials and Solar Cells* **2003**, 76, 125-134
- [23] J. Krustok, J. Raudoja and H. Collan, "Photoluminescence and the tetragonal distortion in CuInS₂", *Thin Solid Films* **2001**, 387, 195-197
- [24] J. Krustok, J. Raudoja, J. H. Schon, M. Yakushev and H. Collan, "The role of deep donor-deep acceptor complexes in CIS-related compounds", *Thin Solid Films* **2000**, 361, 406-410
- [25] J. Krustok, J. H. Schon, H. Collan, M. Yakushev, J. Madasson and E. Bucher, "Origin of the deep center photoluminescence in CuGaSe₂ and CuInS₂ crystals", *Journal of Applied Physics* **1999**, 86, 364-369
- [26] T. Onishi, K. Abe, Y. Miyoshi, K. Wakita, N. Sato and K. Mochizuki, "Study of deep photoluminescence levels in CuInS₂ crystals", *Journal of Physics and Chemistry of Solids* **2005**, 66, 1947-1949
- [27] E. Rudigier, T. Enzenhofer and R. Scheer, "Determination of the quality of CuInS₂-based solar cells combining Raman and photoluminescence spectroscopy", *Thin Solid Films* **2005**, 480, 327-331
- [28] J. Hofhuis, J. Schoonman and A. Goossens, "Elucidation of the excited-state dynamics in CuInS₂ thin films", *J. Phys. Chem. C* **2008**, 112, 15052-15059
- [29] J. Alvarez-Garcia, J. Marcos-Ruzafa, A. Perez-Rodriguez, A. Romano-Rodriguez, J. R. Morante and R. Scheer, "MicroRaman scattering from polycrystalline CuInS₂ films: structural analysis", *Thin Solid Films* **2000**, 361, 208-212
- [30] J. Alvarez-Garcia, A. Perez-Rodriguez, A. Romano-Rodriguez, J. R. Morante, L. Calvo-Barrio, R. Scheer and R. Klenk, "Microstructure and secondary phases in coevaporated CuInS₂ films: Dependence on

growth temperature and chemical composition", *Journal of Vacuum Science & Technology a-Vacuum Surfaces and Films* **2001**, 19, 232-239

[31] A. Goossens and J. Hofhuis, "Spray-deposited CuInS₂ solar cells", *Nanotechnology* **2008**, 19, 424018

Summary and Outlook

New materials and production methods are needed to lower the costs of solar cells. Spray pyrolysis deposition is a promising method for producing thin-film CuInS₂-based solar cells. To date, however, the material quality of spray-deposited CuInS₂ is lower than that of CuInS₂ obtained with conventional deposition methods. Defects in spray-deposited CuInS₂, i.e., interstitials, vacancies, impurities, and anti-site defects have a negative effect on the energy conversion efficiency. Defect states act as recombination centers and stimulate electron-hole recombination. This directly influences the current output of a solar cell.

Formation of a pn-heterojunction introduces interface states, which can affect the solar cell efficiency. Time-of-Flight (ToF) measurements have been performed on TiO₂/CuInS₂ heterojunctions to elucidate the relationship between the presence of interface states and the charge carrier dynamics. In ToF experiments, a short laser pulse creates minority carriers at the TiO₂/CuInS₂ junction, which drift away by the internal electric field. The samples under investigation are solar cells and the outcome of ToF experiments is closely related to the transport of charge carriers in solar cells under operational conditions.

In contrast to conventional ToF experiments, two semiconductor materials are involved, instead of one. Accordingly, the electric field is divided over two semiconductor materials. Because the carrier mobility in CuInS₂ is much larger than that in TiO₂, the CuInS₂ merely acts as an electrical contact to the TiO₂. By measuring the electron-transit time in TiO₂, it is possible to assess the voltage distribution at the TiO₂/CuInS₂ heterojunction, which depends strongly on the electronic properties of the TiO₂/CuInS₂ interface.

It is observed that the drift of electrons through the TiO₂ layer is independent of the applied electric field below an applied bias of 2 V. This observation is not expected for the drift velocity of electrons, which should be linearly dependent on the electric field.

An electrostatic model is developed, in which the surface states at the heterojunction are included. The electric field distribution that follows from the externally applied bias is derived from this electrostatic model. It is found that the presence of surface states leads to Fermi-level pinning in the TiO₂ below an applied bias of 2 volt. As a result, the voltage drop over the TiO₂ is almost zero.

The electric field in the TiO₂, therefore, is small and excited electrons only show diffusion type migration. Above 2 volt bias the Fermi-level pinning is lifted and the voltage drop over the TiO₂ increases linearly with the applied voltage.

In addition to the electrostatic model, a charge transport model is developed, which describes the drift and diffusion velocity of electrons. The TiO₂ layer is divided in a depletion region, in which the potential drop occurs and a drift velocity is present, and a neutral region, in which no electric field is present and a diffusion velocity remains. The width of the depletion region depends on the voltage drop, which follows from the electrostatic model. By combining the electrostatic model with the transport model, the ToF experiment is simulated. Carefully estimating the model parameters shows that Fermi-level pinning indeed is responsible for the ToF observations. An electron mobility of 10⁻² cm²/Vs is found for all three TiO₂ layer thicknesses. The interface state density increases with TiO₂ layer thickness from 5x10¹¹ to 6x10¹² eV⁻¹cm⁻² for 200-400 nm thick TiO₂. Thicker sprayed TiO₂ has more surface roughness, leading to a larger interfacial contact area. Accordingly, the interface states density increases with a thicker TiO₂ layer.

In Cu-rich CuInS₂ indium vacancies and sulfur vacancies introduce defect states near the valence band and the conduction band, respectively. The band structure of spray deposited CuInS₂ is extracted from photoluminescence (PL) experiments. A defect state at 0.15 eV above the valence band is observed, which is assigned to the indium vacancy. Deep defect states at 0.2, 0.25, 1.1, and 1.15 eV are observed, which have not been assigned before. Defect states at nearest and next-nearest neighbor lattice positions cause the existence of doublet states at 0.2 and 1.15 eV above the valence band. PL emissions observed at 0.95 and 0.85 eV are in agreement with the nearest and next-nearest neighbor defect model.

Transient absorption measurements have been performed at room temperature, from which the recombination mechanism of excited charge carriers is extracted. First, the population lifetime of the defect states is determined. It is found that the 1.15 eV doublet state has a lifetime of 20-50 μs, the 0.2 eV doublet state has a lifetime of 3-5 μs, and the 0.15 eV defect state has a lifetime of 0.5 μs. Remarkably, the 0.2 eV doublet state shows a second lifetime component, which equals that of the 1.15 eV doublet state. In addition, the 0.15 eV defect state shows three lifetime components, of which one equals that of the 1.15 eV state and one that of the 0.2 eV state.

The presence of multiple lifetime components gives reason to elaborate a state-to-state recombination mechanism. In this mechanism, charge carriers do

not only recombine between the energy bands and the defect states, but also recombine from one defect state to another. The well-known Shockley, Read, and Hall recombination model has been extended to include state-to-state recombination and the transient absorption experiments are simulated by solving this model numerically. The simulations are in good agreement with the experiment if state-to-state recombination is enabled.

State-to-state recombination can only occur when defects are at nearest-neighbor or next-nearest neighbor positions in the crystal. The Cu/In anti-site defect has this property. It is postulated that the deep donor-deep acceptor pair is related to the presence of associated copper/indium anti-site defects in the chalcopyrite matrix. The defect doublet levels at 1.15 and 0.2 eV are assigned to the $\text{In}_{\text{Cu}}^{\bullet\bullet}$ and the $\text{Cu}_{\text{In}}^{\bullet}$ anti-site defects, respectively. Since also the indium vacancy at 0.15 eV is coupled to the 1.15 eV doublet state, the presence of $(\text{V}_{\text{In}}^{\bullet\bullet} - \text{In}_{\text{Cu}}^{\bullet\bullet} - \text{Cu}_{\text{In}}^{\bullet})^{\bullet}$ defect state association is concluded.

The recombination mechanism of excited charge carriers in spray-deposited CuInS₂ is also studied by means of excitation power dependent photoluminescence (PL) spectroscopy. It is observed that the PL intensity first increases linearly with increasing excitation power, but the PL intensity decreases above a threshold excitation power. This result is unexpected and is not predicted by the existing recombination models. These models do not include state-to-state recombination, which is found to be present in the current samples, as is obtained from transient absorption spectroscopy.

The earlier developed recombination model, in which state-to-state recombination is included, is applied to the excitation-power dependent PL experiments. The effect of state-to-state recombination is elaborated by simulating the PL experiments using a simplified recombination mechanism. It is found that defect state saturation occurs when strong state-to-state recombination is present. Recombination from the conduction band to a defect state is inhibited, if the state is saturated by the state-to-state recombination pathway. The PL emission intensity for the transition from the conduction band to the defect state decreases above a threshold excitation power.

The state-to-state recombination model is applied to simulate the excitation-power dependent PL experiments on spray-deposited CuInS₂ thin films. This model explains the experimental observations very well. It is concluded that the presence of state-to-state recombination results in a decrease of the PL intensity above a threshold excitation power.

In the recombination model, the capture cross section is considered being constant, however, for a donor-acceptor pair the capture cross section can be dependent on the charge carrier concentration. An empirically-based relation

between the capture cross section and the charge carrier concentration improves the fit of the simulation to the experiment.

Annealing CuInS₂ in a sulfur environment is known to improve the material quality. Spray-deposited CuInS₂ is subjected to a rapid thermal anneal in a sulfur containing atmosphere. The material and transport properties are investigated using photoluminescence-, Raman-, and transient absorption spectroscopy. It is found from Raman spectroscopy that the crystal quality improves upon flash annealing in sulfur and equals high-quality CuInS₂ crystals.

It is observed from PL spectroscopy that after flash-annealing in sulfur the PL emission at 0.85 eV disappears. From this, it is concluded that the next-nearest neighbor state-to-state recombination pathway disappears. The PL emission at 0.95 eV, which is assigned to the nearest neighbor state-to-state recombination pathway, and the PL emission from the 1.1 eV defect state to the valence band both decrease in intensity after flash-annealing.

The effect of flash-annealing on the recombination mechanism is derived from transient absorption spectroscopy. Both as-deposited, as well as, flash-annealed CuInS₂ are investigated. It is found that the as-deposited sample shows similar behavior as in earlier research. In addition, the 1.1 eV defect state is found to range between 1.1 and 1.3 eV. In agreement with the PL experiment, no transient absorption is found for the next-nearest neighbor state-to-state transition, which confirms that the next-nearest neighbor defect association disappears after flash annealing in sulfur.

A change in sign for other transitions, including the nearest neighbor state-to-state transition, is observed when CuInS₂ is flash-annealed in a sulfur atmosphere. This indicates a change of the defect-state population, from which a change in the recombination rates is concluded. Analyzing the transient absorption data shows that the recombination rate to the $V_{in}^{\bullet\bullet}$ at 0.15 eV above the valence band has increased and the recombination rate to the $In_{Cu}^{\bullet\bullet}$ defect at 1.1 eV has decreased. The change in recombination rate is related to the presence of sulfur vacancies, which are expected to disappear after the flash-annealing experiment. It is concluded that the sulfur vacancy mediates the recombination to the $In_{Cu}^{\bullet\bullet}$ defect. Removing the sulfur vacancy by flash-annealing in a sulfur atmosphere removes the recombination pathway via the sulfur vacancy and the $In_{Cu}^{\bullet\bullet}$ defect state.

Conclusions and outlook

The presence of deep defect states influences the efficiency of CuInS₂-based solar cells. Because of the long lifetime of electrons in the deep defect state, electronic charge is stored in the bandgap of CuInS₂. As a direct

consequence, the Fermi-level will rise and accordingly the voltage output of a CuInS₂-based solar cell is decreased. This explains why CuInS₂-based solar cells have not yet reached an output voltage above 50% of the theoretical value.

Flash annealing in a sulfur ambient does not remove the Cu/In anti-site defect. However the population rate of the In_{Cu}^{••} defect is reduced strongly. This will affect the current-output of the solar cell, since less charge will recombine through this defect. Because of the long lifetime of electrons in the In_{Cu}^{••} defect, charge is still stored in this defect state, also if a low population rate is present. Therefore, it is not expected that the output voltage of a CuInS₂-based solar cell will improve when flash-annealing in a sulfur ambient is applied to CuInS₂.

The Cu/In antisite defect is present as a stable defect in the chalcopyrite matrix and difficult to monitor, since the crystal structure is only changed locally. XRD- or Raman-spectroscopy do not indicate the presence of a Cu/In antisite defect. Photoluminescence spectroscopy can show the presence of the defect, but precautions have to be taken into account. First, the excitation level has to be low enough to prevent defect-state saturation, as is explained elsewhere in this thesis. Second, the detection level of the PL equipment has to be low enough to monitor the small signal that belongs to the anti-site defect. Especially, if low concentrations of the anti-site defect are present, they may not be found experimentally.

When the formation of the Cu/In anti-site defect can not be prevented or solved, the efficiency of CuInS₂-based solar cells will not exceed the current level. The Cu/In anti-site defect should be considered as a material property, which is present under all circumstances. A detailed study of the formation of the anti-site defect in order to remove the anti-site defect can solve the anti-site issue. Such a study should include a detailed study of the effect of deposition parameters and heat treatments upon charge carrier recombination. Complicated synthesis procedures, however, will not improve the economic efficiency of the CuInS₂-based solar cells. Regarding to low cost deposition techniques, recombination to the anti-site defect can be minimized by sulfur-annealing, but the defect will not fully be removed and the voltage output will remain far below the theoretical value. Inhibition of the recombination path by sulfur-annealing can increase the current-output of the solar cell, which will lead to a higher economical potential.

Samenvatting

Nieuwe materialen en productiemethoden zijn nodig om de kosten van zonnecellen te verlagen. Sproei-depositie is een veelbelovende techniek om zonnecellen, die gebaseerd zijn op dunne-laag CuInS₂ te produceren. De materiaalkwaliteit van gesproeide CuInS₂ lagen is momenteel lager dan voor lagen die met conventionele depositietechnieken zijn vervaardigd. Defecten in gesproeide lagen, zoals interstitiële, vacatures, verontreinigingen en *anti-site* defecten hebben een negatief effect op het rendement van de energieomzetting. Defecten vormen locaties voor recombinatie en bevorderen de electron-gat recombinatie. De stroom uit een zonnecel wordt hierdoor direct beïnvloed.

Door de vorming van een pn-heterojunctie kunnen energietoestanden aan het oppervlak ontstaan die het rendement van een zonnecel beïnvloeden. Time-of-Flight (ToF) metingen aan TiO₂/CuInS₂ heterojuncties zijn uitgevoerd om het verband tussen de aanwezigheid van oppervlaktetoestanden en de dynamiek van ladingdragers te onderzoeken. Bij ToF metingen wordt een korte laserpuls gebruikt om ladingdragers te creëren aan het TiO₂/CuInS₂ oppervlak, welke diffunderen onder invloed van een intern elektrisch veld. De onderzochte samples zijn zonnecellen en het resultaat van de experimenten is nauw gerelateerd aan het transport van ladingdragers in werkende zonnecellen.

In tegenstelling tot normale ToF metingen zijn twee halfgeleider materialen gebruikt, waar het normaal slechts één materiaal betreft. Dit heeft tot gevolg dat het elektrisch veld verdeeld wordt over beide halfgeleiders. Omdat de mobiliteit van de ladingdragers in het CuInS₂ vele malen hoger is dan die in TiO₂ gedraagt het CuInS₂ zich als een elektronisch contact voor het TiO₂. Door de reistijd van de electronen in het TiO₂ te meten is het mogelijk de verdeling van de spanning over de TiO₂/CuInS₂ heterojunctie in kaart te brengen. Deze verdeling is sterk afhankelijk van de elektronische eigenschappen van de TiO₂/CuInS₂ overgang.

De experimenten laten zien dat de drift van electronen door het TiO₂ onafhankelijk is van de laagdikte van het TiO₂, wanneer een voltage lager dan 2 V wordt aangelegd. Deze waarneming is niet verwacht voor de drift-snelheid van electronen, welke lineair afhankelijk van het elektrisch veld zou moeten zijn.

Een elektrostatisch model waarin de energietoestanden aan het grensvlak van de heterojunctie zijn meegenomen wordt ontworpen. De

verdeling van het elektrisch veld, als gevolg van een extern aangelegde spanning, is afgeleid van dit electrostatische model. Het model laat zien dat de aanwezigheid van oppervlaktetoestanden leidt tot *Fermi-level pinning* in het TiO₂ wanneer een externe spanning lager dan 2 volt wordt aangelegd. Een direct gevolg van *Fermi-level pinning* is dat de spanningsval over het TiO₂ bijna nul is. Het elektrisch veld in het TiO₂ is daarom klein en aangeslagen elektronen hebben alleen een diffusie-gerelateerde migratie. Bij een aangelegde spanning hoger dan 2 volt wordt *Fermi-level pinning* opgeheven en neemt de spanningsval over het TiO₂ lineair toe met de aangelegde spanning.

Als toevoeging aan het electrostatische model is een model voor ladingtransport ontworpen. Dit model beschijft de drift- en diffusiesnelheid van elektronen. De TiO₂ laag is verdeeld in een depletielaag, waarin de spanningsval plaatsvindt, en een neutraal gebied waarin geen elektrisch veld aanwezig is en dus alleen diffusie-transport plaatsvindt. De breedte van de depletielaag hangt af van de grootte van het spanningsval, welke volgt uit het electrostatische model.

Door het electrostatische model en het model voor ladingtransport met elkaar te combineren kan het ToF experiment gesimuleerd worden. Wanneer de verschillende parameters zorgvuldig gekozen worden laat de simulatie zien dat *Fermi-level pinning* verantwoordelijk is voor de waarnemingen van de ToF metingen. Voor alle drie de TiO₂ laagdikten is een elektronen beweeglijkheid van $10^{-2} \text{ cm}^2/\text{Vs}$. De dichtheid van de energietoestanden aan het oppervlak neemt toe met de laagdikte van 5×10^{11} tot $6 \times 10^{12} \text{ eV}^{-1} \text{ cm}^{-2}$ voor 200-400 nm dikke TiO₂ lagen. Dikker gespreeid TiO₂ heeft meer oppervlakte ruwheid en leidt tot een groter oppervlak aan de materiaalovergang. Hierdoor is de dichtheid van de oppervlaktetoestanden groter voor dikkere TiO₂ lagen.

In koper-rijk CuInS₂ veroorzaken indium- en zwavelvacatures defecten met een energieniveau in de buurt van respectievelijk de valentieband en de geleidingsband. Met behulp van fotoluminescentiespectroscopie (PL) is de bandenstructuur van CuInS₂ bepaald. Op 0.15 eV boven de valentieband is een defect gevonden, die is toegewezen aan de indium-vacature. Nog niet eerder toegewezen defecten zijn waargenomen op 0.2, 0.25, 1.1 en 1.15 eV boven de valentieband. Defecten op naaste buur en volgend-naaste buur roosterplaatsen veroorzaken de aanwezigheid van dubbele defecten op 0.2 en 1.15 eV boven de valentieband. In overeenstemming met dit model zijn PL emissies gevonden op 0.95 en 0.85 eV. Uit transient absorptiemetingen bij kamertemperatuur is het recombinatie-mechanisme van aangeslagen ladingdragers afgeleid. Als eerste is de bezettingstijd van de defecten bepaald. Het 1.15 eV dubbele defect heeft een levensduur van 20-50 μs , het 0.2 eV dubbele defect heeft een levensduur van 3-5 μs en het 0.15 eV defect heeft een levensduur van 0.5 μs . Het is opmerkelijk

dat het 0.2 eV dubbele defect een tweede levensduur-component heeft, welke gelijk is aan die van het 1.15 eV dubbele defect. Verder heeft het 0.15 eV defect drie levensduur-componenten, waarvan er één gelijk is aan die van het 0.15 eV defect en één aan die van et 0.2 eV defect.

De aanwezigheid van meerdere levensduur-componenten geeft aanleiding om een defect-naar-defect recombinatiemodel af te leiden. Bij dit mechanisme recombineren ladingdragers niet alleen tussen de energiebanden en de defecten maar vindt ook recombinatie tussen twee defecten plaats. Het bekende model van Schockley, Read en Hall is uitgereid tot een model waarin defect-naar-defect recombinatie is inbegrepen. De transient absorptiemetingen zijn gesimuleerd door het model numeriek op te lossen. Deze simulaties zijn in goede overeenstemming met de experimenten wanneer het defect-naar-defect recombinatiemechanisme gebruikt wordt.

Defect-naar-defect recombinatie kan alleen plaatsvinden wanneer de defecten zich op naaste buur of volgend-naaste buur posities in het kristal bevinden. Het koper-indium anti-site defect heeft deze eigenschap. Het is gepostuleerd dat het diepe donor - diepe acceptor paar gerelateerd is aan het geassocieerde koper-indium anti-site defect in de chalcopyriet matrix. De dubbele defecten op 1.15 en 0.2 eV zijn toegewezen aan respectievelijk de $\text{In}_{\text{Cu}}^{\bullet\bullet}$ en $\text{Cu}_{\text{In}}^{\bullet}$ anti-site defecten. Omdat ook de indium vacature op 0.15 eV gekoppeld is aan het 1.15 eV dubbele defect wordt de aanwezigheid van het $(\text{V}_{\text{In}}^{\bullet\bullet} - \text{In}_{\text{Cu}}^{\bullet\bullet} - \text{Cu}_{\text{In}}^{\bullet})^{\bullet}$ defect-associaat geconcludeerd.

Het recombinatiemechanisme van aangeslagen ladingdragers in gesproeid CuInS₂ is ook bestudeerd met behulp van excitatievermogen-afhankelijke fotoluminescentie-spectroscopie. De waargenomen PL intensiteit neemt eerst lineair toe met toenemend excitatievermogen, maar neemt af na het bereiken van een grenswaarde van het excitatievermogen. Dit resultaat is niet verwacht en wordt niet voorspeld door de bestaande recombinatie-modellen. Deze modellen houden geen rekening met de defect-naar-defect recombinatie die is gevonden met behulp van transient absorptiespectroscopie.

Het eerder ontworpen model, waarin defect-naar-defect recombinatie is inbegrepen, is toegepast op de excitatievermogen-afhankelijke PL metingen. Het effect van de defect-naar-defect recombinatie is onderzocht door PL experimenten aan een defect recombinatie aanwezig is, vindt verzadiging van een defect plaats. Recombinatie van de geleidingsband naar een defect wordt gehinderd als het defect is verzadigd door de defect-naar-defect recombinatie. De intensiteit van de PL emissie voor de overgang van de geleidingsband naar het defect neemt af bij toenemend excitatievermogen.

Het defect-naar-defect recombinatie model is toegepast op gesproeide CuInS₂ dunne lagen en de excitatievermogen-afhankelijke PL metingen worden

gesimuleerd. Dit model verklaart de experimenten vrij goed. De aanwezigheid van defect-naar-defect recombinatie resulteert in een afname van de PL intensiteit boven een bepaald grenswaarde van het excitatievermogen.

In het recombinatie-model wordt de invangdoorsnede aangenomen als een constante. Echter, voor een donor-acceptor paar kan de invangdoorsnede afhankelijk zijn van de concentratie van ladingdragers. Een empirische vergelijking tussen de invangdoorsnede en de concentratie van ladingdragers verbetert de overeenkomst tussen de simulatie en het experiment.

Het is bekend dat het temperen van CuInS₂ in een zwavel atmosfeer de materiaalkwaliteit verbetert. Gesproeid CuInS₂ ondergaat een snelle temper behandeling in een zwavelhoudende atmosfeer. De materiaal- en transport eigenschappen zijn onderzocht met behulp van fotoluminescentie-, Raman- en transient absorptie spectroscopie. Raman spectroscopie laat zien dat de kristalkwaliteit verbetert tijdens flits-temperen in een zwavelhoudende atmosfeer en gelijk wordt aan die van hoge-kwaliteit CuInS₂.

Met behulp van PL spectroscopie wordt waargenomen dat na het flits-temperen in een zwavelhoudende atmosfeer de PL emissie van 0.85 eV verdwijnt. Hieruit wordt geconcludeerd dat de volgende-naaste buur defect-naar-defect recombinatie verdwijnt. De PL emissie van 0.95 eV, welke is toegewezen aan de naaste-buur defect-naar-defect recombinatie, en de PL emissie van het 1.1 eV defect naar de valentieband, nemen beide af in intensiteit na het flits-temperen.

Het effect van flits-temperen op het recombinatiemechanisme is afgeleid van transient-absorptiespectroscopie waarbij zowel niet- als wel- getemperd CuInS₂ is onderzocht. Het niet-getemperde CuInS₂ vertoont dezelfde eigenschappen als in een eerder onderzoek. Als toevoeging wordt gevonden dat het 1.1 eV defect een gebied tussen de 1.1 en 1.3 eV inneemt. In overeenstemming met de PL experimenten wordt er geen transient absorptie gevonden voor de volgend-naaste buur overgang, wat bevestigt dat de volgend-naaste buur defectassociatie verdwijnt na het flits-temperen in een zwavelhoudende atmosfeer.

Een verandering van teken is waargenomen na flits-temperen in een zwavelhoudende atmosfeer voor de andere overgangen, inclusief de naaste-buur defect-naar-defect overgang. Dit geeft aan dat een verandering in de bezetting van defecten plaatsvindt, waaruit een verandering in de recombinatiesnelheid wordt geconcludeerd. Uit de transient-absorptie metingen volgt dat de recombinatiesnelheid naar de V_{In}^{\bullet} op 0.15 eV boven de geleidingsband is toegenomen en de recombinatiesnelheid naar het In_{Cu}^{\bullet} defect op 1.1 eV is afgenomen. De verandering in recombinatiesnelheid is gerelateerd aan de aanwezigheid van zwavel vacatures, waarvan wordt verwacht dat deze

verdwijnen na het flits-temperen experiment. Er wordt geconcludeerd dat de zwavel vacature als schakel dient voor de recombinatie naar het $\text{In}_{\text{Cu}}^{\bullet\bullet}$ defect. De verwijdering van de zwavel vacature door flits-temperen in een zwavelhoudende atmosfeer verwijdert de recombinatie-mogelijkheid via de zwavel vacature en het $\text{In}_{\text{Cu}}^{\bullet\bullet}$ defect.

Conclusies en vooruitblik

De aanwezigheid van diepe defecten beïnvloedt het rendement van CuInS₂-gebaseerde zonnecellen. De lange levensduur van electronen in diepe defecten zorgen voor ladingsopslag in de verboden bandafstand van CuInS₂. Een direct resultaat is een toename van de energie van het Fermi-niveau met als gevolg een afname van de spanning van een CuInS₂-gebaseerde zonnecel. Dit verklaart, waarom de uitvoerspanning van CuInS₂-gebaseerde zonnecellen niet boven 50% van de theoretische waarde uitkomt.

Het flits-temperen in een zwavelhoudende atmosfeer verwijdert het Cu/In anti-site defect niet. Echter, de vulsnelheid van het $\text{In}_{\text{Cu}}^{\bullet\bullet}$ defect neemt sterk af. Hierdoor neemt de stroom door de zonnecel toe, omdat minder lading recombineert via dit defect. De lange levensduur van electronen in het $\text{In}_{\text{Cu}}^{\bullet\bullet}$ defect resulteert echter nog steeds in de opslag van lading in de verboden bandafstand, ook al is er een lage vulsnelheid. Om deze reden ligt het niet in de verwachting, dat de uitvoerspanning van een CuInS₂ gebaseerde zonnecel zal toenemen, wanneer flits-temperen in een zwavelhoudende atmosfeer is toegepast.

Het Cu/In anti-site defect is aanwezig als een stabiel defect in de chalopyriet matrix en moeilijk waar te nemen. Immers, de kristalstructuur wordt alleen lokaal aangetast. Met Röntgendiffractie of Raman spectroscopie kan het Cu/In antisite defect niet worden waargenomen. Fotoluminescentie kan het defect wel zichtbaar maken, maar aan enkele voorwaarden moet worden voldaan. Als eerste moet het excitatievermogen laag genoeg zijn om verzadiging van de defecten te voorkomen, zoals elders in dit proefschrift is besproken. Ten tweede, de gevoeligheid van de detectieapparatuur moet hoog genoeg zijn om het kleine signaal van het anti-site defect waar te kunnen nemen. Als slechts kleine hoeveelheden van het anti-site defect aanwezig zijn is het mogelijk dat deze experimenteel niet worden waargenomen.

Wanneer de vorming van het Cu/In anti-site defect niet kan worden voorkomen of opgelost, zal het rendement van CuInS₂-gebaseerde zonnecellen niet boven het huidige niveau uitstijgen. Het Cu/In anti-site defect moet beschouwd worden als een materiaaleigenschap, die onder alle omstandigheden aanwezig is. Een gedetailleerd onderzoek naar de vorming van het anti-site defect, met als doel dit defect te verwijderen, kan bijdragen aan een oplossing

van dit probleem. Zo'n onderzoek zou een gedetailleerde studie van het effect van depositie-instellingen en warmtebehandelingen op de recombinatie van ladingdragers moeten bevatten.

Ingewikkelde syntheseprocedures leiden echter niet tot verbetering van het economisch rendement van CuInS₂ gebaseerde zonnecellen. Met betrekking op goedkope depositietechnieken kan recombinatie naar het antisite defect geminimaliseerd worden door de toepassing van een warmtebehandeling in een zwavelhoudende atmosfeer, maar het anti-site defect zal nooit compleet verdwijnen en de uitvoerspanning zal ver beneden de theoretische waarde blijven. Het voorkomen van het recombinatiemechanisme met behulp van temperen in een zwavelhoudende atmosfeer kan de stroom uit de zonnecel verhogen, waardoor het economisch rendement toeneemt.

Publications

published papers

J.P.T. Hofhuis, J. Schoonman, A.P.L.M. Goossens
Time-of-flight studies on TiO₂/CuInS₂ heterojunctions
Journal of Applied Physics, 103 (2008) 014503-1 - 014503-7

J.P.T. Hofhuis, J. Schoonman, A.P.L.M. Goossens
Elucidation of the Excited-State Dynamics in CuInS₂ Thin Films
Journal of Physical Chemistry C, 112 (2008), 15052 - 15059

A.P.L.M. Goossens, J.P.T. Hofhuis
Spray-deposited CuInS₂ solar cells
Nanotechnology, 19 (2008) 424018 - 424018

submitted papers

J.P.T. Hofhuis, J. Schoonman, A.P.L.M. Goossens
Elucidation of the excited-state dynamics in CuInS₂ thin films
submitted to *Solar Energy Materials and Solar Cells*

J.P.T. Hofhuis, E.Bouman, J.Schoonman, A.P.L.M. Goossens
How flash annealing affects defect association in spray deposited CuInS₂
submitted to *Journal of Applied Physics*

Talks

J.P.T. Hofhuis
Time of flight studies on TiO₂-CuInS₂ heterojunctions
Quantosol Winterworkshop 2006, Austria, 21 March 2006

J.P.T. Hofhuis ., J. Schoonman, A.P.L.M. Goossens
Near-infrared photoluminescence and transient absorption spectroscopy of
spray deposited CuInS₂
EMRS, Strasbourg, 27 May - 1 June 2007

Curriculum Vitae

Joris Hofhuis was born at October 3th, 1978 in Delft. He obtained his secondary school diploma (VWO) at the "Sint Stanislas College" in Delft in 1997. From 1997 till 2004 he studied Materials Science and Engineering at the Delft University of Technology. During his master studies he visited the National Laboratory for Sustainable Energy of Denmark (Risø), where he studied new materials for hydrogen storage. His undergraduate research was performed in the group of prof. Joop Schoonman and was focused on electronic transport properties in thin film solar cells. In 2005 he started his work as a Ph.D. student, continuing the study he started as a master student. The results are presented in this thesis and in a number of publications.

Dankwoord

Dit proefschrift kon niet tot stand komen zonder de directe of indirecte hulp van vele mensen. Allereerst wil ik mijn promotor, Joop Schoonman, bedanken. Het werk in dit proefschrift heeft plaatsgevonden in een wetenschappelijke omgeving die door uw inzet tot stand is gekomen. Ik hoop dat het 'pensioen' nog veel mooie wetenschap brengt. Albert Goossens wil ik bedanken voor zijn dagelijkse begeleiding. Ik heb veel van je geleerd. Je wist op je eigen wijze mijn grenzen te verleggen en mij te stimuleren niet bang te zijn voor het onbekende. Je brede wetenschappelijke en fundamentele kennis heeft in belangrijke mate bijgedragen aan de inhoud van dit proefschrift.

De collega's van Anorganische Chemie, Opto-electronische Materialen en Materials for Energy Conversion and Storage wil ik bedanken voor het bieden van een prettige werkomgeving. Ruben Loef, bedankt voor het aanwezig zijn als naaste collega. Jouw chemische achtergrond heeft mij enorm geholpen in het uitvoeren van eenvoudige handelingen die ik niet eerder gedaan had. Jouw deur ging altijd open als er behoefte was aan een praatje. Harry Donker, bedankt voor het overdragen van je kennis over optische opstellingen en lasers, zonder deze kennis zouden mijn metingen nooit gelukt zijn. Juleon, ondanks je korte bijdrage heeft deze geleid tot de meeste resultaten, bedankt hiervoor. Marius Nanu, bedankt voor het ontwikkelen van de sproeidepositie techniek en het begeleiden tijdens mijn afstuderen. Jouw werk diende als basis voor dit proefschrift. Ruben Abellon, bedankt voor de ondersteuning en fijne gesprekken. Evert Bouman wil ik graag bedanken voor zijn bijdrage aan hoofdstuk 4 in dit proefschrift. Het was een genoegen jou te begeleiden in je bachelor project. De collega's van Advanced Surface Technology (AST BV, Bleiswijk) wil ik bedanken voor het maken van enkele monsters die in dit proefschrift zijn onderzocht. Ik wens jullie veel succes in de toekomst. Gerrit Schotte, bedankt voor de technische ondersteuning bij de ontwikkelingen van de apparatuur. Ondanks dat weinig van jouw werk uiteindelijk in dit proefschrift terecht is gekomen heb ik veel van je geleerd, bedankt hiervoor. Astrid, Marian en Cecelia bedankt voor de onmisbare secretariële ondersteuning. Kamergenoten Sander Lems, Arjan Didden en Yen Tran, bedankt voor de koffie en de gezellige en nuttige gesprekken.

Als laatste wil ik mijn familie en vrienden bedanken voor de mooie momenten die niets met promoveren te maken hebben. Irene, je hebt me er doorheen gesleept als het even niet meer ging. Er bestaan geen woorden, die mijn dank en waardering uit drukken.